# DIMUON MEASUREMENT BY THE CBM EXPERIMENT AT FAIR ENERGY

Thesis

submitted for the award of the degree of

*Doctor of Philosophy*

in

*Physics*

by

**Shabir Ahmad**

**Under the Supervision of**

**Dr. M. Farooq Mir**


***Department of Physics,***

***University of Kashmir, Srinagar, 190 006***

**October, 2015**

# Acknowledgements

I would like to take this opportunity to thank all those people who contributed to the completion of this work. First, I would like to gratefully acknowledge and extend my heartfelt gratitude to my Research Supervisor, **Dr. M. Farooq Mir** for introducing me into the field of High Energy Physics and providing me various opportunities to work in other collaborating centres. His constant guidance helped me a lot to finish this research work in time.

My regardful thanks are due to **Dr. Manzoor A. Malik**, Head of Physics Department and **Prof. Sheikh Javid**, Dean Research, University of Kashmir for providing me with necessary infrastructure, help, support and other facilities during my tenure of research. I also extend my thanks to the whole teaching faculty of the department for their generous help whenever needed.

My sincere thanks to **Dr. Subhasis Chattopadhayay**, an eminent scientist in experimental high energy physics at VECC, Kolkata for his valuable suggestions and timely help in the completion of my work in appropriate time. My special thanks are also to our CBM Collaborators especially **Dr. Peter Senger, Dr. Ana Senger,** Dr. Iouri Vissilev, Dr. Volkar Friese, Dr. Volodia Nikulin and Dr. Horst Stoecker from GSI Germany, Dr. Steffen A. Bass from Duke University Durham USA, and Dr. Y.P. Viyogi, Dr. D. K. Srivastava, Dr. Tapan K. Nayak, Dr. Zubyer, Dr. Anand Dubey, Dr. P. P. Bhaduri, Dr. Jan-e-Alam, Dr. Vikas Singhal, and Miss Ekata Nandy from VECC for their guidance and academic suggestions throughout my research period.

My sincere thanks to senior scholars and my friends Mr. Raja Nisar and Mr. Waheed Ahmad for their timely suggestions. My special thanks to my

friends and scholars Mr. Asif Iqbal, Mr. Mubashir Hamid, Mr. Waseem Raja, Mr. Firdous Ahmad, Miss Suraya, Mr. Bari Maqbool, Mr. Javid Para, Mr. Billal Malik, Miss Qudsiya Gani, Mr. Zahoor Ahmad, Mr. Naveel Ahmad, Mr. Billal Ahmad, Mr. Shamsul Haque, Mr. Muzamil and Miss Rubaya Sofi for their help during the completion of my research work. Thanks are also due to research scholars Miss Hushnud (AMU), Mr. Mukesh Sharma (JU), Mr. Kalyan Dey (GU), Dr. Arun Kumar (BHU), Mr. Inaam (JMI), Mr. Subhasis Samanta (BOSE Int.), Rama Prasad Adak (BOSE Int.) and Miss Nirupama from University of Notre Dame, USA for their help, support, and good wishes.

I sincerely thank all the members of technical and non-technical/non-teaching staff of the department for their affection and kind co-operation.

I extend my thanks to my close friends Mr. Manzoor Ahmad Dar, Mr. Fayaz Ahmad Wani, Dr. Abdul Wahid, Dr. Feroz Ahmad Mir, Mr. Ajaz Ahmad Dar, Mr. Fayaz Ahmad Najar, Mr. Riyaz Ahmad Bhat, Mr. Salim Ahmad Lone and Mr. Zahoor Ahmad Mir for their support, concern and best wishes.

I also thank to Mrs. Raveena Hassan, Mrs. Sameena, and Dr. Renu Vakil from GCW, M. A. Road and Prof. Naseer Ahmad, Mr. Billal Ahmad, and Mr. Mehraj Ahmad from GDC, Ganderbal for their consistent support, concern and wishes.

I have no words to express my gratitude to my parents, brother, sister and close friends for bearing with me throughout programme. I shall always remain indebted to them for their unstinted support, be it financially, morally or inspirationally.

***Shabir Ahmad***

# Post Graduate Department of Physics, University of Kashmir, Srinagar.

## Certificate

This is to certify that the thesis entitled "***DIMUON MEASUREMENT BY THE CBM EXPERIMENT AT FAIR ENERGY***" submitted by ***Shabir Ahmad***, in partial fulfilment for the award of the degree of ***Doctor of Philosophy*** in ***Physics***, is the original research work carried out by him under our supervision and guidance. It is further certified that the thesis has not been submitted for the award of Ph.D. or any other degree to this University or any other University. The scholar has attended the department for statutory period as required under rules.

**Dr. M. Farooq Mir**
(*Supervisor* )

**Dr. Manzoor A. Malik**
(*Head of the department* )

# Publications

1. *Design and performance simulation of a segmented-absorber based muon detection system for high energy heavy ion collision experiment*
   **S. Ahmad**, M. Farooq et al, NIM A 775, 139-147 (2015), ISSN: 0168-9002

2. *Study of secondaries produced in the MUCH detector of the CBM Experiment*
   **S. Ahmad** and M. Farooq, CBM Progress Report 2012, p. 45, FAIR-GSI, Darmstadt, Germany (publisher), ISBN: 978-3-9815227-0-9.

3. *Identification of dimuons from low-mass vector mesons with CBM at SIS-300*
   **S. Ahmad**, S. Chattopadhayay, and M. Farooq, CBM Progress Report 2013, p. 114, FAIR-GSI, Darmstadt, Germany (publisher), ISBN: 978-3-9815227-1-6.

4. *Effeciency of the CBM Muon Chamber system for low-mass vector mesons*
   **S. Ahmad**, S. Chattopadhayay, and M. Farooq, CBM Progress Report 2013, p. 115, FAIR-GSI, Darmstadt, Germany (publisher), ISBN: 978-3-9815227-1-6.

5. *Simulation of beam-pipe shielding for CBM-MUCH*
   **S. Ahmad**, M. Farooq, and S. Chattopadhayay, CBM Progress Report 2014, p. 70, FAIR-GSI, Darmstadt, Germany (publisher), ISBN: 978-3-9815227-2-3.

6. *The Compressed Baryonic Matter Experiment at FAIR*
   CBM Collaboration (.., **S. Ahmad** et al), Nuclear Physics A 904, 941c-944c (2013) 941c-944c, ISSN: 0375-9474.

7. *Measurement of dileptons with the CBM experiment at FAIR*
   CBM Collaboration (.., **S. Ahmad** et al), Nuclear Physics A 931, 735-739 (2014), ISSN: 0375-9474.

8. *Measurement of rare probes with the Silicon Tracking System of the CBM experiment at FAIR*
   CBM Collaboration (.., **S. Ahmad** et al), Nuclear Physics 931, 1136-40 (2014), ISSN: 0375-9474.

9. *Anisotropic Flow of Identified Hadrons by the Event Plane Method at FAIR Energies*
   S. Bashir, M. Farooq, **S. Ahmad**, IJFPS, Vol 5, 12-17 (2015), ISSN: 2231-8186

10. *Propagation of Fluctuations in Au+Au Collisions at FAIR energy*
    **S. Ahmad**, M. Farooq et al, arXiv:1408.5107 [hep-ph], ISSN: 2331-8422

11. *Evolution of strangeness fluctuations at FAIR energies*
    **S. Ahmad**, S. Chattopadhayay, and M. Farooq, CBM Progress Report 2014, p. 146, FAIR-GSI, Darmstadt, Germany (publisher), ISBN: 978-3-9815227-2-3.

12. *Technical Design Report for the CBM Muon Chamber (MUCH)*
    .., **S. Ahmad** et al (MUCH Working Group & CBM Collaboration), GSI Report 2013-4, Germany

# Proceedings

1. *Secondaries upstream and downstream the first absorber of muon detection system for CBM Experiment at FAIR*

**S. Ahmad** and M. Farooq, Proceedings of the DAE Symp. on Nucl. Phys. 58, p. 964 (2013)

2. *Segmentation Optimization for dimuon detection system in CBM Experiment at FAIR*
   H. Jahan, **S. Ahmad** et al, Proceedings of the DAE Symp. on Nucl. Phys. 58, p. 748 (2013)

3. *Cocktail detection with CBM Experiment at 25 GeV*
   **S. Ahmad**, S. Chattopadhayay, and M. Farooq, Proceedings of the DAE Symp. on Nucl. Phys. 59, p. 686 (2014)

4. *STS Effects and MUCH Effeciency of CBM Experiment*
   **S. Ahmad**, M. Farooq, and S. Chattopadhayay, Proceedings of the DAE Symp. on Nucl. Phys. 59, p. 754 (2014)

5. *Optimisation of Beam-Pipe Shielding for MUCH detector of CBM experiment*
   **S. Ahmad**, M. Farooq, and S. Chattopadhayay, Proceedings of the DAE Symp. on Nucl. Phys. 59, p. 754 (2014)

6. *Net-Proton Evolution in Heavy Ion Collisions*
   **S. Ahmad**, M. Farooq, and S. Chattopadhayay, Proceedings of the DAE Symp. on Nucl. Phys. 60, 740 (2015)

7. *Optimisation of Selection Cuts for MUCH detector of CBM experiment*
   M. Farooq, **S. Ahmad**, S. Chattopadhyay, Proceedings of the DAE Symp. on Nucl. Phys. 60, 912 (2015)

8. *MUCH beam-pipe for CBM experiment*
   **S. Ahmad**, E. Nandy, S. Bashir, M. Farooq, and S. Chattopadhayay, Proceedings of the DAE Symp. on Nucl. Phys. 60, 1026 (2015)

9. *Study of the elliptic flow and their energy dependence over pseudorapidity rang at FAIR energies*
   S. Bashir, M. Farooq, **S. Ahmad**, and F. Ahmad, Proceedings of the DAE Symp. on Nucl. Phys. 60, 732 (2015)

10. *Performance Study of MUCH beam-pipe and Shielding for CBM experiment*
    E. Nandy, S. Chattopdhyay, and **S. Ahmad**, Proceedings of the DAE Symp. on Nucl. Phys. 60, 806 (2015)

Dedicated

To

My Parents

# Contents


**1 Theoretical Overview** **16**

1.1 Quantum Chromodynamics . . . . . 17
1.2 Quark Gluon Plasma . . . . . 18
1.3 Relativistic Heavy Ion Collisions . . . . . 21
1.3.1 Space Time Evolution . . . . . 23
1.4 Signatures of QGP . . . . . 25
1.4.1 Direct Photon Production . . . . . 25
1.4.2 Di-lepton Production . . . . . 26
1.4.3 Low Mass Vector Mesons . . . . . 28
1.4.4 $J/\psi$ Suppression . . . . . 29
1.4.5 Strangeness Enhancement . . . . . 31
1.4.6 Jet Quenching . . . . . 32
1.4.7 Collective Flow . . . . . 34
1.4.8 Fluctuations . . . . . 35
1.5 Chiral Symmetry Restoration . . . . . 36
1.6 Detectors in High Energy Experiments . . . . . 37
1.7 Motivation and Plan of Present Work . . . . . 39

**2 The CBM Experiment at FAIR** **41**

2.1 The Facility for Anti-proton and Ion Research (FAIR) . . . . . 41
2.1.1 Experiments at SIS100 Accelerator . . . . . 43
2.1.2 Experiments at SIS300 Accelerator . . . . . 44
2.2 CBM Detector Concepts . . . . . 45
2.2.1 The Muon Chamber System (MUCH) . . . . . 49

2.2.2 Electronics for MUCH . . . . . 54
2.2.3 Data Acquisition System (DAQ) . . . . . 56

**3 DIMUON MEASUREMENT 57**
3.1 Muons . . . . . 57
3.2 Dimuon Sources . . . . . 58
3.3 Dimuon Continuum . . . . . 62
3.4 Combinatorial Background . . . . . 63
3.5 Experimental Results . . . . . 63
3.5.1 Low Mass Vector Mesons . . . . . 63
3.5.2 Thermal Radiation . . . . . 67
3.5.3 Charmonium . . . . . 69
3.6 Summary . . . . . 70

**4 DIMUON DETECTION SYSTEM FOR CBM 73**
4.1 Muon Chamber (MUCH) . . . . . 75
4.1.1 First Absorber . . . . . 76
4.1.2 MUCH Layout . . . . . 80
4.1.3 Tracking Detectors . . . . . 82
4.1.4 Beam Conditions . . . . . 83
4.2 Simulation Tools . . . . . 84
4.3 Simulation Procedure . . . . . 86
4.3.1 Geometry implementation and transport . . . . . 87
4.3.2 Digitization . . . . . 90
4.3.3 Clustering and Hit-Finder . . . . . 92
4.3.4 Track Propagation . . . . . 92
4.3.5 Muon identification . . . . . 93
4.4 MUCH Beam-pipe and its Shielding . . . . . 94
4.4.1 Beam-Pipe Shielding . . . . . 94
4.4.2 Beam-Pipe for MUCH . . . . . 96

**5 PHYSICS PERFORMANCE OF MUCH 102**
5.1 Input to the Simulations . . . . . 102
5.1.1 Event Generator . . . . . 103

5.2 Detector performace of low mass vector mesons at 25 GeV . . 109
5.3 Using Time of Flight Detector . . . . . 112
5.4 Combinatorial Background/Signal . . . . . 114
5.5 Detection of $J/\psi$ at SIS300 . . . . . 116
5.6 Summary . . . . . 117

**6 PHYSICS AT FAIR** **119**
6.1 FLUCTUATION . . . . . 119
6.1.1 UrQMD Hybrid version . . . . . 122
6.1.2 Methodology . . . . . 123
6.1.3 Results . . . . . 125
6.1.4 Discussions . . . . . 136
6.2 STRANGENESS PRODUCTION . . . . . 137
6.2.1 Models . . . . . 138
6.2.2 Results . . . . . 139
6.2.3 Conclusion . . . . . 141

**7 Summary and Conclusion** **143**

# List of Figures


1.1 hadro-Synthesis . . . . . 20
1.2 QCD phase diagram . . . . . 20
1.3 Relativistic Heavy ion Collision . . . . . 22
1.4 Formation of QGP at high temperature and high baryon density 23
1.5 Space-time evolution of an ultra-relativistic nuclear collisions . 24
1.6 Time evolution nuclear collision . . . . . 25
1.7 Di-lepton production . . . . . 27
1.8 Di-electronic background . . . . . 28
1.9 Invariant mass distribution of lepton pairs . . . . . 29
1.10 $J/\psi$ suppression . . . . . 30
1.11 Strangeness enhanced production . . . . . 32
1.12 Jet Quenching . . . . . 33
1.13 Directed flow . . . . . 34
1.14 Strange particle production at SPS . . . . . 38

2.1 FAIR Layout at GSI, Germany . . . . . 42
2.2 CBM experiment set-up RICH . . . . . 46
2.3 CBM experiment set-up with MUCH . . . . . 47
2.4 The CBM muon detection system . . . . . 50
2.5 GEM structure when viewed in an electron microscope . . . . 52
2.6 Amplification inside the GEM detector . . . . . 52
2.7 Straw tube parts and its working . . . . . 53
2.8 n-XYTER for CBM and under test . . . . . 54
2.9 The FEE with ROC . . . . . 55

3.1 NA60 dimuon invariant mass distributions . . . . . 64

3.2 Signal extracted from NA60 dimuon continuum . . . . . 65
3.3 Excess mass spectra of dimuons in NA60 . . . . . 66
3.4 Dimuon excess in NA60 compared with theory . . . . . 66
3.5 Transverse mass spectra of the excess dimuons . . . . . 67
3.6 Inverse slope parameter versus dimuon mass in NA60 . . . . . 68
3.7 $J/\psi$ suppression pattern in In+In collisions . . . . . 70
3.8 Total charm production cross-section measurements . . . . . 71

4.1 Fraction of surviving particles with Absorber thickness . . . . 76
4.2 Multiplicity Comparison for C and Fe Absorber . . . . . 78
4.3 Ratio of reconstructed to MC tracks . . . . . 79
4.4 $\chi^2_{MUCH}$ of the tracks from signal muons and backgrounds . . . 80
4.5 MUCH layout . . . . . 81
4.6 Sector Geometry . . . . . 83
4.7 Simulation Procedure . . . . . 86
4.8 Input ASCII MuCh geometry file . . . . . 88
4.9 MUCH with Beam-Pipe . . . . . 89
4.10 First MUCH Station Radial hit distribution . . . . . 89
4.11 Segmentation of the first MUCH station . . . . . 91
4.12 MUCH with different beam-pipe options . . . . . 94
4.13 Hit density for different beam-pipes . . . . . 95
4.14 Background comparison of MUCH beam-pipes . . . . . 96
4.15 Old and New Beam-Pipe . . . . . 97
4.16 Point density from New and Old Beam-pipes . . . . . 98
4.17 Beam-Spot size and profile . . . . . 99
4.18 MUCH with ECAL, Lead Opening view . . . . . 100
4.19 Hits of MUCH & STS with lead-hole radius . . . . . 101

5.1 Input Cocktail . . . . . 104
5.2 Spectra of LMVM resonances from PLUTO . . . . . 105
5.3 Spectra of pions and kaons from UrQMD . . . . . 108
5.4 Like sign & unlike sign background comparison . . . . . 109
5.5 Reconstructed Cocktail & S/B . . . . . 110
5.6 Acceptance of reconstructed $\rho^0$ . . . . . 111

5.7 Composition of the reconstructed background . . . . . 112
5.8 $\beta^{-1}$ V/s $q$ in ToF . . . . . 113
5.9 MUCH with TOF . . . . . 114
5.10 TOF Hits & S/B comparison . . . . . 115
5.11 Reconstructed $J/\psi$ dimuon spectra & Acceptance . . . . . 117

6.1 Evolution of net-baryon density with time . . . . . 126
6.2 Mean multiplicities of pion with elapsed time . . . . . 127
6.3 Mean multiplicities of kaon with elapsed time . . . . . 127
6.4 Evolution of $K/\pi$ ratio with time . . . . . 128
6.5 Time evolution of $\nu_{dyn}$ of $K/\pi$ . . . . . 129
6.6 Time evolution of $\nu_{dyn}$ of $Q^+/Q^-$ . . . . . 129
6.7 Beam energy dependence of kaon and pion . . . . . 130
6.8 Beam energy dependence of the ratio of kaon to pion . . . . . 130
6.9 Beam energy dependence of $\nu_{dyn}$ for $K/\pi$ . . . . . 131
6.10 $\nu_{dyn}$ with $E$ for $K/\pi$ with pure & hydro mode . . . . . 132
6.11 $\nu_{dyn}$ with $E$ for $Q^+/Q^-$ with pure & hydro mode . . . . . 133
6.12 Time evolution of $S\sigma$ for net-proton . . . . . 134
6.13 Time evolution of $K\sigma^2$ for net-proton . . . . . 134
6.14 $S\sigma$ with $E$ for net-proton . . . . . 135
6.15 $K\sigma^2$ with $E$ for net-proton . . . . . 135
6.16 Mean multiplicities of strange particles . . . . . 139
6.17 Strange hyperons with strangeness quantum number . . . . . 140
6.18 Multi-strange particles as a function of $|S|$ . . . . . 141

# List of Tables

2.1 Ion species and their kinetic energy per nucleon at SIS100/SIS300 43

4.1 Cuts used for LMVM and $J/\psi$ analysis . . . . . 94

5.1 Multiplicities of different particles from HSD . . . . . 106
5.2 Branching ratio of some important resonances . . . . . 107
5.3 Reconstructed particle efficiencies . . . . . 111
5.4 Combinatorial background/signal in dilepton experiments . . . 116

# Chapter 1

# Theoretical Overview

Standard model is considered as a successful theory describing most of the fundamental particles and their interactions. It helps us to understand the working of nature all the way back just after a fraction of a second after to the famous Big Bang. Discovery of last predicted but undetected particle called Higgs Boson (*God's Particle*) in July 2012 fully established the success of Standard Model in high energy physics. While the Standard Model groups elementary particles into three generations, each comprising two leptons and two quarks, searches for a fourth generation have failed [1, 2] with strong indirect evidence of against its existence [3, 4, 5]. Generally particles are massive in higher generations, and hence less stable causing them to decay via weak interactions into lower-generation. Consequently only first-generation particles, i.e. up and down quarks, are found commonly in nature. High energy collisions, like in cosmic rays, create heavier quarks which then decay quickly. They must have been there just after the fractions of a second after the Big Bang, as the universe was in an extremely hot and dense phase. Nowadays particle accelerators are used to create and study heavier quarks in artificially created conditions called *Little Bangs* [6]. After the invention of accelerators in 1960's which could accelerate protons or electrons to high energies and smash them, called as relativistic collisions, to produce new particles [7], hundreds of new particles were found. Through a long series of experiments and theoretical studies, Standard Model was formed which

classified them in a very simple scheme of two basic sets of particles: the quarks and leptons and a set of fundamental forces transmitted via exchange particles called gauge bosons. Role of particle physicist is to test this model in all conceivable ways to discover whether something more lies beyond it.

In this unit we will give brief introduction of theory of high energy physics relevant to relativistic heavy ion collisions, new state of de-confined quarks and gluons (QGP) and finally brief introduction about the detectors used in relativistic heavy ion collisions.

## 1.1 Quantum Chromodynamics

The field theory for the strong interaction, called as quantum chromodynamics (QCD), is formulated in the non-Abelian gauge theory with $SU(3)_c$ color symmetry. QCD allows combinations of quarks containing equal mixtures of imaginary colors: red, green, blue; along with anti-colors, to form color neutral particles observed in nature. Color force quarks interact through the exchange of *gluons*, a massless particle, with a strength which has conspicuous behaviour for a variation of momentum transfer square $Q^2$. The strong coupling constant representing the color force strength usually written as $\alpha_s = g_s/4\pi$ *runs* as $Q^2$ varies. Accordingly physics of QCD has been divided into two regimes [8]: (1) *large* $Q^2$ region where $\alpha_s(Q^2)$ becomes small, realized in hard scattering like deep inelastic scattering, where quarks and gluons behave as free particles known as *asymptotic-freedom* and the perturbation theory works well in this region. (2) *small* $Q^2$ region where $\alpha_s(Q^2)$ becomes large, realized in the static state of bound quarks confined inside hadrons called as the *confinement* phase and in such a region lattice QCD calculations are employed. Coupling constant $\alpha_s$ depending upon the wavelength of the quark written as $\alpha_s(E) = \frac{12\pi}{(33-2n_f)ln(\frac{E^2}{\Lambda^2})}$, where $n_f$ is the number of quarks active in pair production, $\Lambda$ is the wavelength of quarks and its experimentally obtained value is $\approx 0.2$ GeV. $\alpha_s$ has value $\approx 1$ at the radius of a proton. If the proton is penetrated at a radius corresponding to an energy of 1 TeV, $\alpha_s$ goes down to $\approx 0.1$ corresponding to asymptotic freedom [9].

Quantum chromodynamics must describe the dynamics of quarks and gluons from *asymptotic-freedom* to *confinement* phase [10].

Individual quarks are never observed in particle accelerators, detector observes *jets* of many color-neutral particles (mesons and baryons) which are clustered together. This is as a result of the confinement, for two quarks separated in heavy ion collisions at some point, it becomes more energetically favourable for a new quark-anti-quark pair to spontaneously appear via string breaking/fragmentation/hadronisation rather than bag of bound state quarks to extend further. The processes involved like hadronization, fragmentation and string breaking are one of the least understood processes in particle physics. Inter-quark confining potential i.e. $V = -\frac{\alpha_s}{4\pi r} + kr$, where $k$ is the string constant and $r$ is inter-quark distance, tends to zero by reducing the potential with decreasing distance.

In QED, in the vicinity of a charge, the vacuum becomes polarized and virtual particles of opposing charge are attracted to the charge, and virtual particles of like charge are repelled. The net effect is to partially cancel out the field at any finite distance. Getting closer and closer to the central charge, one sees less and less of the effect of the vacuum, and the effective charge increases. This is known as charge *screening* effect. Just like in QED (Quantum electrodynamics) QCD virtual quark-anti-quark pairs tend to screen the color charge. As each gluon carries both a color charge and an anti-color magnetic moment, so net effect of polarization of virtual gluons in the vacuum is not to screen the field but to augment it, called as *anti-screening*, while changing its color. By decreasing the separation between the quark diminishes the anti-screening effect which would weaken the effective charge and coupling strength. The gluon cloud penetration carrying color charge between the quarks would reduce the effective color charge of the quarks known as *color screening* [11].

## 1.2 Quark Gluon Plasma

Once the color charge density inside nucleons is increased, screening radius ($r_D$) is reduced and a stage reaches when $r_D$ becomes less than $r_H$( hadron

radius) and at the point strongly interacting matter is expected to transite from the color insulator hadronic matter to color conductor quark-gluon plasma (QGP) phase.

Quarks inside hadrons have effective mass $m_q^{eff} \approx 300$ MeV while asymptotic freedom leads eventually to a vanishing quark mass in QGP. A theory with massless quarks is *chirally symmetric* which is spontaneously broken at low density and gets restored when $m_q^{eff} \to 0$ at high density [12, 13]. Mass decrease in hot and dense medium is expected to increase in the width of the resonance peaks of vector mesons which can be used as signature of newly formed noval medium [14].

Quark gluon primordial soup is supposed to be originated just after few microseconds of the Big Bang through the hadro-synthesis process depicted as in the figure 1.1. A dense state of matter is expected to exist in the interior of Neutron stars due to its large density inside the core [15].

Lattice QCD predict a diagram for the envisaged nuclear matter phases shown in figure 1.2. Three dynamical light quark flavours computations on the lattice [17] revealed that a phase transition from a hadronic matter to quarks gluons plasma at low chemical potential of quarks and at a critical temperature $T_c \sim 170$ MeV corresponding to an energy density $\epsilon_c = 0.6\ GeV/fm^3$. Moreover, color flavor locked (CFL) phase and color superconductivity [16] are expected at large baryonic chemical potentials with comparatively small temperature as depicted in phase-diagram [14].

Heavy ion collisions, also known as *Little Bang*, are used to create matter at high temperature and energy density and the conditions that existed immediately after the Big Bang. Many heavy ion projects have been undertaken to investigate the matter at extreme conditions. The *CERN* lead beam programme was initiated in 1994 and seven large experiments were involved to measure different aspects of Pb+Pb (lead-lead) and Pb+Au (lead-gold) collisions. All the seven experimental sites were code-named as *NA44*, *NA45*, *NA49*, *NA50*, *NA52*, *NA57* and *WA98* where acronym NA stands for north-area and WA stands for west-area which are regions of the accelerator. There are modern experiments which study the QGP like *LHC* (Large Hadron Collider) at CERN, *RHIC* (Relativistic Heavy Ion Collider) at Brookhaven,

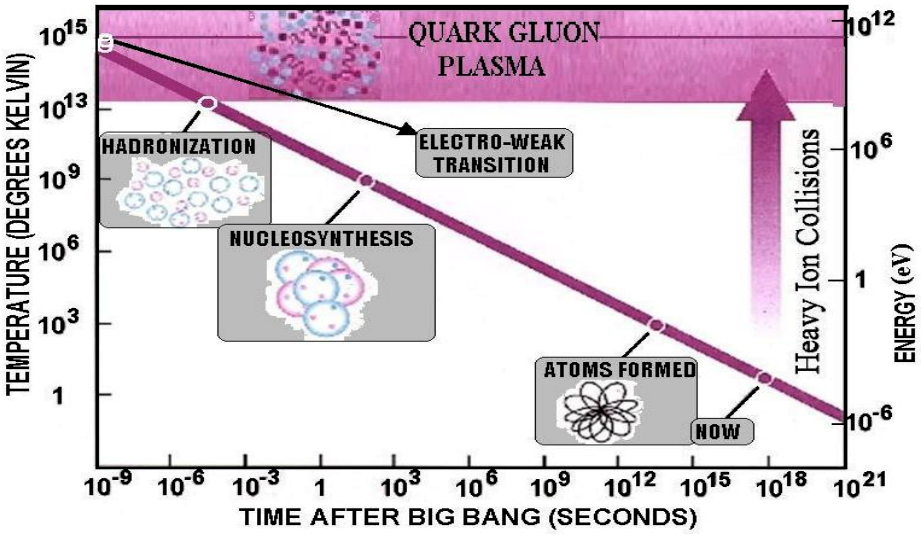


Figure 1.1: The transition from plasma of quarks and gluons to ordinary matter occurred some $10^{-5}s$ after the Big Bang when the temperature lowered to about $10^{12}K$. The inverse process is expected to occur nowadays at relativistic heavy ion collision experiments at LHC, RHIC, future CBM etc..

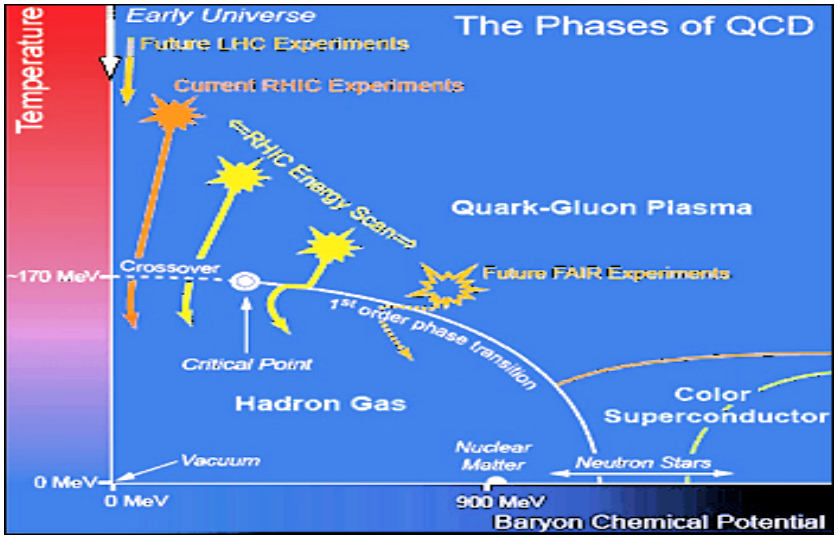


Figure 1.2: QCD phase diagram

future *FAIR-CBM* Experiment at GSI Germany and so on..

## 1.3 Relativistic Heavy Ion Collisions

Based on the two scenarios like high temperature and high density, we expect QGP formation at three places:

- In the early universe
- At the centre of compact stars
- In the initial stage of high energy heavy ion collisions.

In experiments last possibility is pursued currently. Ordinary nuclei are defined by a much smaller temperature than the proton and pion rest masses and their baryon density is $\sim 0.14$ nucleons/fm$^3$ which corresponds to an energy density of 130 MeV/fm$^3$. As inter-distance between nucleons is larger than their radius ($\approx 0.8$ fm), so transformation of these nucleons into QGP requires the nucleon wave functions overlaps significantly. Such conditions are likely reachable by smashing heavy nuclei together at relativistic energies resulting in much higher nuclear energy density causing nucleons to melt into a soup of quarks and gluon's through a process that reverses the early universe history.

Although we can achieve high energy density also in relativistic collisions where system-size is small like in electron-positron ($e^- - e^+$) or proton-proton ($p - p$) collisions but overall *interaction region size is too small* to study the de-confinement related effects. Moreover, because of the short range nature of the strong interactions and subsequent short range QGP evolution, the relevant experimental observables representing signal comes mainly from the interior of the dense medium while background essentially originates from the surface. Since the signal over background ratio is proportional to the colliding object's volume over surface ratio which is favourably best for heavy ion collisions.

When heavy nuclei collisions occur, nucleons gets excited to short-lived states of baryon resonance decaying with the emission of mesons. Even at higher temperatures baryon anti-baryon pairs are created. The mixture of mesons, baryons and anti-baryons known to be **hadronic matter** at high

temperature or known as **baryonic matter** when baryons preponderate at high density. In nucleus-nucleus collision overlapped region is called *partic-*

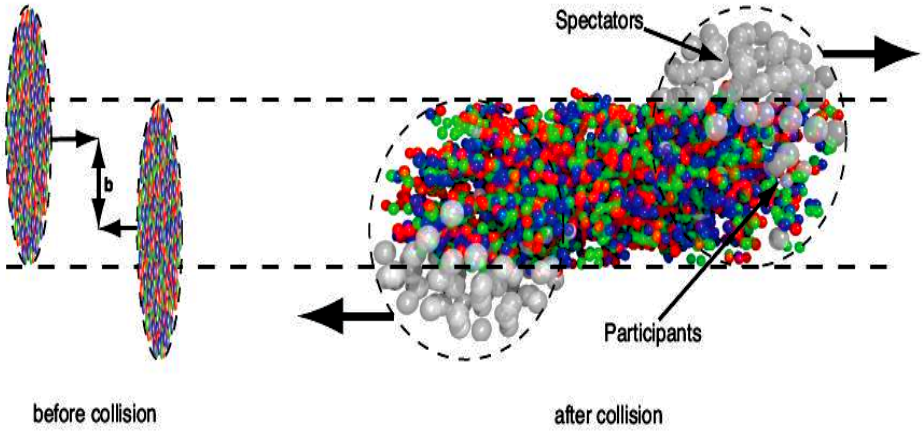


Figure 1.3: Relativistic Heavy ion Collision scenario for b>0

*ipant* region while the rest part of the nuclei which doesn't participate in collision is called the *spectator* region as depicted in Fig. 1.3. Spectator region of the nuclei move apart at relativistic energies and fragment in a very narrow cone around their original direction. Centrality of the collision determines certain bulk properties of matter created in (heavy ion) collisions described interms of impact parameter b (which is a distance between the centers of two colliding nuclei). Events with ($\mathtt{b} \sim 0$) are called central events which are the best candidates for creating noval medium of QGP as peripheral collisions at large b do not provide the enough geometrical overlap of nucleons needed to achieve high energy density in a large volume [14].

One of the main goals of the heavy ion collision experiments at RHIC and LHC and future FAIR energies is the study of quark gluon plasma and the QCD phase diagram. At FAIR, phase diagram of nuclear matter will be explored at high baryonic density region with relatively low temperature complementary to LHC which focuses at high temperatures with relatively small chemical potential (baryon density). When two heavy nuclei are accelerated such as Au ( A=197) up to relativistic energies, nuclei gets Lorentz-contracted as "*pancakes*". Colliding nuclei having centre-of-mass energy per nucleon more than 100 GeV tend to pass through each other, as

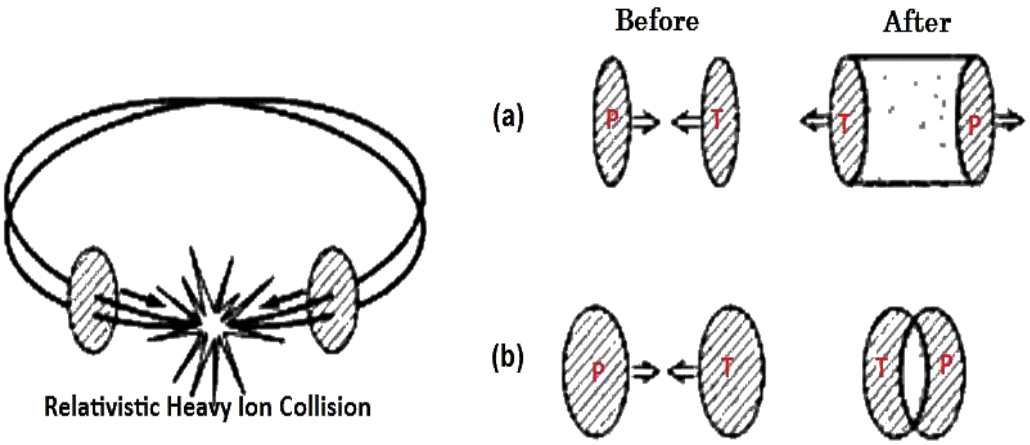


Figure 1.4: **(a)**Formation of QGP at high temperature by means of relativistic nucleus-nucleus collision with a collider-type accelerator. **(b)** Formation of QGP at high baryon density by means of less energetic collision than in (a)

depicted in Fig. 1.4(a), producing matter high in energy density and temperature but low in baryon density. The Relativistic Heavy Ion Collider (RHIC) at Brookhaven National Laboratory (BNL) and the Large Hadron Collider (LHC) at CERN provides this situation. On the other hand, when the colliding nuclei have energy at few tens of GeV per nucleon, they tend to stay with each other, as depicted in Fig. 1.4(b), producing matter which not only high temperature but also high in baryon density [14]. NA60, NICA and future CBM experiment at FAIR provide this situation. Theoretically we say when the incident beam energy exceeds the velocity of sound in nuclear matter at ground state matter density ($\beta_s = 0.2$), nucleons cannot escape fast enough and zone of high density is formed in heavy ion collisions.

### 1.3.1 Space Time Evolution

When Lorentz contracted nuclei collide, two scenario are expected to precede. Initial formation of hadron gas state made of pions mostly is followed by freeze-out which is linked to a superposition of many binary nuclear collisions. In second case, initial stage is followed by an equilibrated quark gluon plasma state which gradually becomes hadrons and parton mixed phase as it cools then chemical freeze-out of particles species occur forming hadron gas and

finally kinetic freeze-out is followed as depicted by Fig. 1.6 and Fig. 1.5.

The participant region in relativistic heavy ion collisions has a very different behaviour schematically illustrated in Fig. 1.6. Figure just gives a temporal hierarchy as there is no clear delimitation in the evolution of the participant region. After the "*formation time*", which is $\sim$ 1 fm/c, quarks

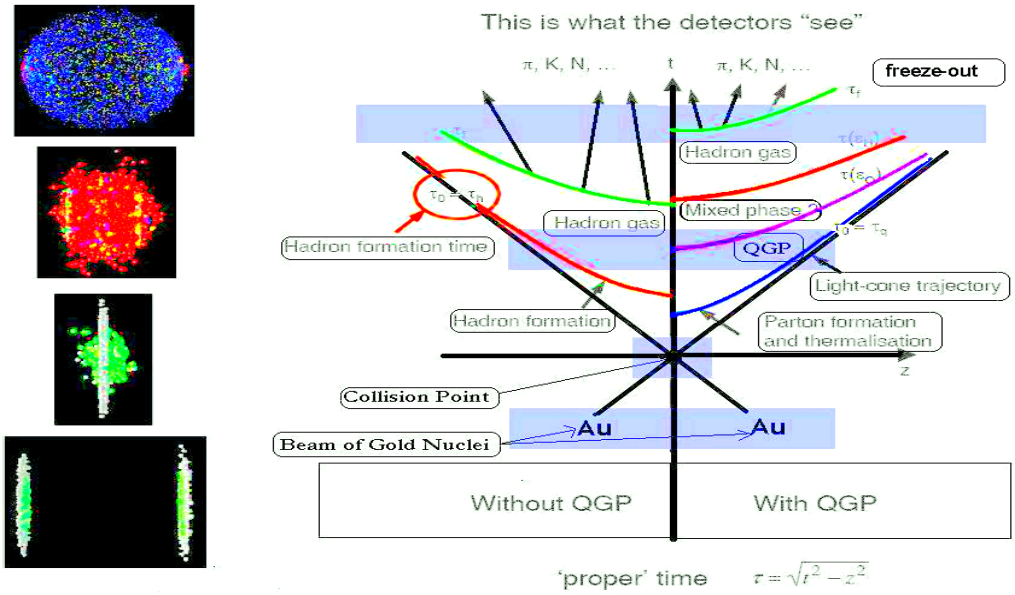


Figure 1.5: Space-time diagram of the evolution of an ultra-relativistic nuclear collision as viewed in the nucleon-nucleon center-of-mass system.

and gluons of highly excited color field materialise and reaction between individual pairs establishes *thermal equilibrium* leading to the creation of the so-called "*fireball*". System expands and cools rapidly mainly along the longitudinal direction till it reaches the transition temperature $T_c$ of QGP. For the QGP formation with the system is in thermal equilibrium, thermodynamics description of the system can be used. Subsequently mixed phase is formed where hadronization starts in the expanding "fireball" in an ordered motion with large outward flow through a hadron gas phase until the particles cease to interact known as"*freeze out*" eventually recieved by the detector. Singals associated with each phase is observed by experiments. In relativistic heavy ion collisions, baryons appear in the centre-of-mass predominantly at the initial beam rapidities while the central rapidity region is expects to have the

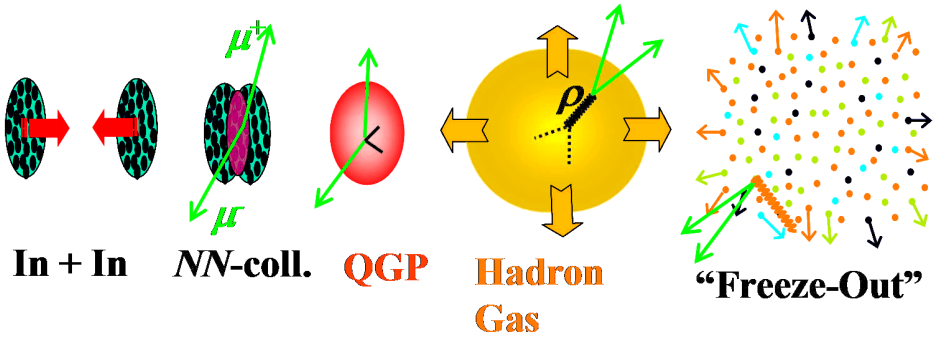


Figure 1.6: Time evolution of nuclear collisions

bulk of produced particles.

## 1.4 Signatures of QGP

Main problem in heavy ion collision is that we can only see the particles that escape from the fireball after the freeze-out which reach the detectors. Signals have to be recognised which could help in reconstructing what happened before so that one can work out whether quark-gluons plasma was formed or not. The experiments must be optimised for measuring different signals of quark-gluon plasma which have small size (5-10 fm) and small life time ($\approx 10^{-23} sec$). Theoretically predicted prominent signals of quark gluon phas have been discussed briefly in following subsections.

### 1.4.1 Direct Photon Production

Electromagnetic radiation in the form of photons emitted by quarks enable us to detect their effects directly. Quarks interact via real or virtual photon in QGP with former having long mean free path due to their interaction enabling them to escape cleanly to carry the information about the temperature of the state. On the other hand, virtual photon decays via di-leptonic channel carrying the same message as that by the direct photon. Two main processes of direct photon production inside QGP are:

1. *Annihilation Process:* In annihilation process gluon is produce along with one $\gamma$

$$q \ + \ \bar{q} \ \longrightarrow \ \gamma \ + \ g \tag{1.1}$$

2. *Compton Process:* In this process gluon scatters off a quark (or anti-quark).

$$g \ + \ q(\bar{q}) \ \longrightarrow \ \gamma \ + \ q(\bar{q}) \tag{1.2}$$

Background noise in *hadronic processes* comes mostly from pion interactions, like Pion Annihilation ($\pi^+ + \pi^- \longrightarrow \ \gamma + \rho^0$), Charged pion - neutral pion interaction ($\pi^\pm + \pi^0 \longrightarrow \ \gamma + \rho^\pm$), pion - rho interaction ($\pi^\pm + \pi^0 \longrightarrow \gamma + \rho^\pm, \ \pi^\pm + \rho^\mp \longrightarrow \ \gamma + \pi^0, \ \pi^0 + \rho^\pm \longrightarrow \ \gamma + \pi^\pm$ ) etc., which mimic direct photon production in a QGP [13]. Large number of neutral mesons, such as $\pi^0$ and $\eta$ decaying into two gamma (photons) with a branching ratio 98.8 % and 38.9% respectively, are produced by soft QCD processes and hence the copious source of photons. Photons can also be produced by bremmstahlung in heavy ion collisions [135, 136, 137] which is significant at low photon energies. Decay of hadrons through photons leads to a large spread in energy due to broad hadron rapidity distribution.

The number of photons from hadron decay is greater than from other photon sources by 1 - 2 order of magnitude. Its experimental challenge to separate out the $\gamma$ (photon) yields into a part from the decays of produced hadrons, and other 'single $\gamma$' part from other sources. Hadronic interactions occur at a lower temperature than quark-gluon plasma, so photon momentum distribution can be used to differentiate the two cases which eventually tell us about the thermodynamical state of the QGP [13]. For QGP formation photons with $p_T$ range 2-3 GeV/c is considered to be clear signal of the same [18, 19].

### 1.4.2 Di-lepton Production

Virtual photons $\gamma^*$ from the quark $q$-antiquark $\bar{q}$ anhillation inside QGP subsequently decays into dilepton pairs ($l^- l^+$) as depicted in figure 1.7.

As di-leptons interact only through the electromagnetic force, so their free mean path is quite large enabling them to come out cleanly even after

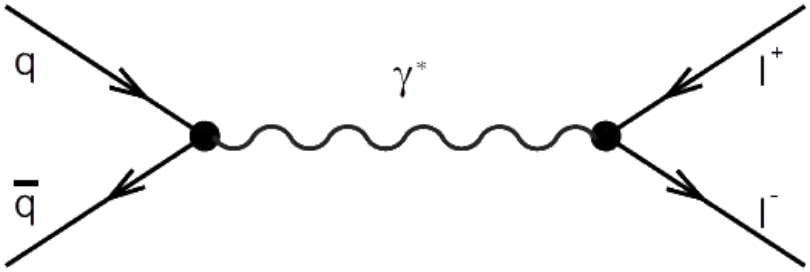


Figure 1.7: Reaction $qq \longrightarrow l^- l^-$ in quark gluon plasma

their production in QGP. Production rate and momentum distribution of di-leptons depends on the properties of the quark-antiquark pairs governed by the thermodynamic condition of the plasma. Therefore, the di-leptons can be used to extract the information of the thermodynamical state of QGP when they were produced enabling us to conceive the initial state of the collision [13] . One of the prominent decay channel of quark - anti-quark interaction is :

$$q\bar{q} \quad \longrightarrow \quad \mu^+\mu^- \quad (Signal) \tag{1.3}$$

Some of the hadronic processes serving as background, by increasing the di-lepton yield, includes:

- *Drell-Yan Process:* When a nucleon valence quark of one nucleus interact with a nucleon anti-quark of another nucleus [20], they get annihilated forming a virtual photo which subsequently decays via dilepton pair as depicted in figure 1.8a.

- $\pi^+\pi^-$ *annihilation and hadron resonance decays* ($\rho, \omega, \phi$ and J/$\psi$) as shown in figure 1.8b.

- eta - pion interaction:
  $\eta^+\pi^- \quad \longrightarrow \quad \mu^+\mu^-$

The number of $l^+l^-$ pairs from the Drell-Yan process scales as $A^{4/3}$ for central collisions of same system size. Their contribution plays important role in the upper edge of the dimuon invariant mass region (about 1.5 GeV) [13]. It has been suggested that a window of invariant mass region between $\phi$ and J/$\psi$ gives dileptons from the plasma phase [21]. Above the J/$\psi$ mass Drell-Yan and direct charm decay contribution dominates [22, 23], while below $\rho$

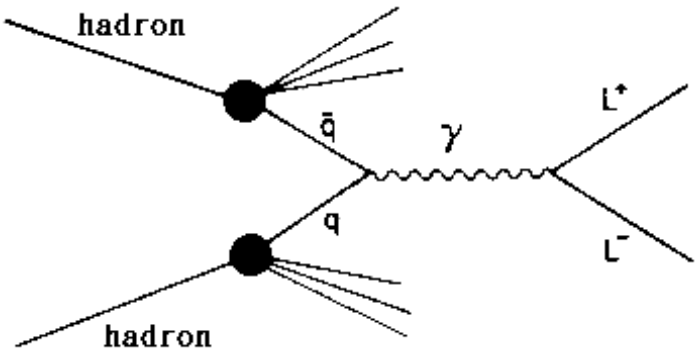


(a) Drell Yan Process

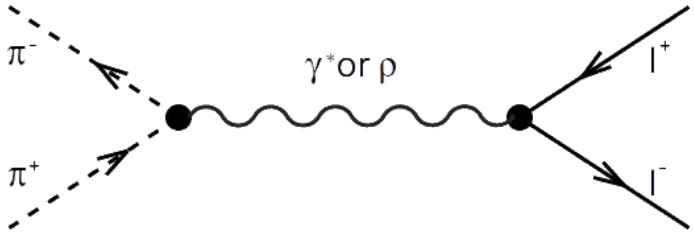


(b) $\pi^+\pi^-$ annihilation

Figure 1.8: Di-leptonic background

meson mass, radiative and direct decays and $\pi\pi$ annihilation forms the most important contribution [24, 25, 26].

### 1.4.3 Low Mass Vector Mesons

Production of low mass vector mesons ($\rho^0$, $\omega$,, $\phi$, etc..) in heavy nucleus collisions is considered an effective probe of QGP. Their properties like mass, width, and branching ratios are expected to be sensitive to strong 'in-medium effects' and 'chiral effects'. They can decay into lepton pairs even at the time of medium formation making it clean signal of medium modifications. A graph of the number of lepton pairs in terms of invariant mass shows a peak for each vector meson resonance with a wide peak for $\rho^0$ and a sharp peak of $\omega$ meson on its top. We observe no $\rho^0$ peak but a broad smear in experiments because $\rho^0$'s decay just after their formation while the hadrons are still interacting and short time between collisions does not give them an

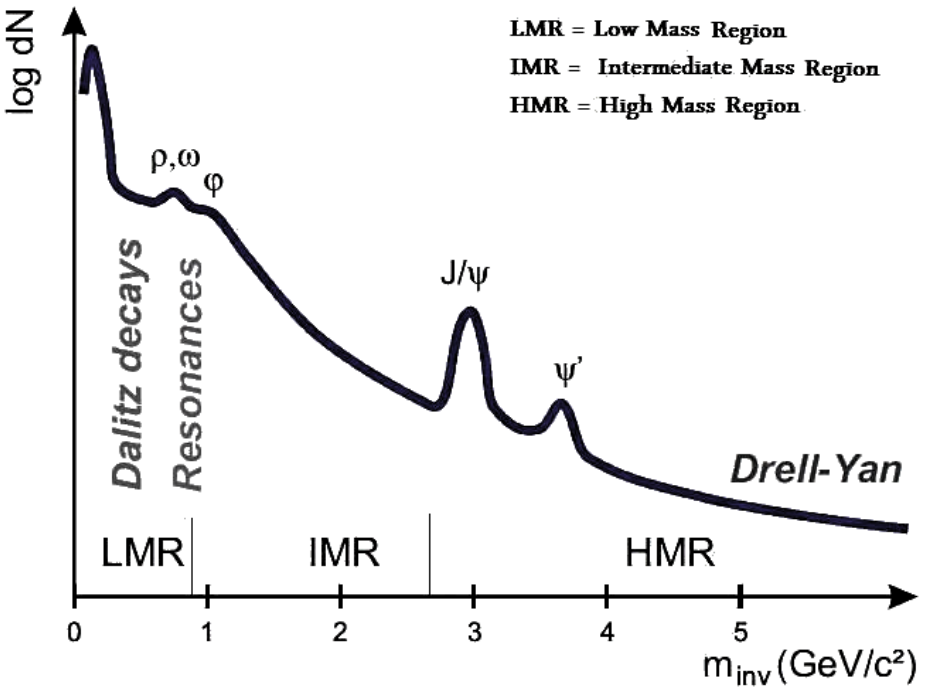


Figure 1.9: Invariant mass distribution of lepton pairs

opportunity to develop into a well-defined mass state. Thus figure 1.9 acts as a snapshot of the collision stage directly just after the liberated quarks condense and well before the hadrons stop interacting.

Decays of $J/\psi$ and $\psi'$ resonances shows two peaks at 3.1 $GeV/c^2$ and 3.7 $GeV/c^2$ respectively on larger side of invariant mass region known as high mass region (HMR). While resonances on the smaller side ($< 1$ $GeV/c^2$) of invariant mass spectrum, known to be low mass region (LMR), are from $\rho^0$, $\omega$, and $\phi$ meson decays. Di-lepton spectrum at even lower masses is dominated by *Dalitz* decays of $\pi^0, \eta, \eta'$, and $\omega$.

### 1.4.4 $J/\psi$ Suppression

The $J/\psi$ meson being the bound state of a charm quark c and a charm antiquark $\bar{c}$ has bound state radius $r_{J/\psi} = \frac{1}{2m_c}$ (with charm quark mass $m_c$= 1.5 GeV/$c^2$) which so small ($\simeq$ 0.20 fm) and, thus, making it tightly bound state very difficult to break apart. If somehow $J/\psi$ is broken apart then charm quark and anti-charm quark will combine separately with an up or

down antiquarks to form a $D^0(c\bar{u})$ or a $D^+(c\bar{d})$ and a $\bar{D}^0(\bar{c}u)$ or a $D^-(\bar{c}d)$ respectively. In that case, binding energy of the $J/\psi$ comes out to be:

$$\epsilon_{J/\psi} = m_{D\bar{D}} - m_{J/\psi} = 634 \;\; MeV \tag{1.4}$$

Large binding energy and small size makes the $J/\psi$ hard to break apart. Not present initially, this long lived bound state of heavy quarks originate mainly from *gluon-gluon fusion* which create heavy quark pairs like $c$-$\bar{c}$ or a $b$-$\bar{b}$ that become a bound state at very early times in the collision when the temperature of medium is still above charm/bottom production threshold.

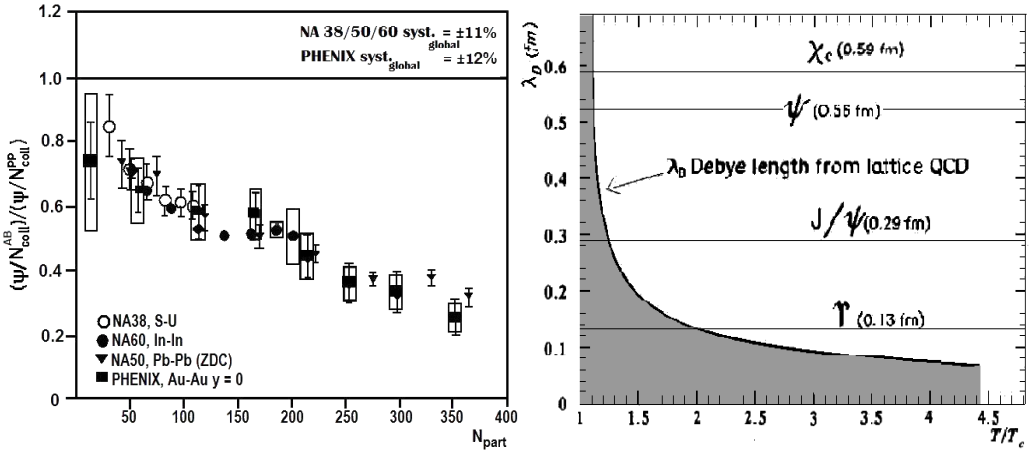


(a) J/$\psi$ suppression at RHIC (b) Quarkonium bound state threshold

Figure 1.10: (a) $J/\psi$ suppression in lead-lead (Pb-Pb) collisions at the SPS ($\sqrt{S_{NN}} = 17GeV$) and in gold-gold (Au-Au) at RHIC as a function of the reaction centrality. (b) Debye length as a function of the ratio between the melting temperature and the transition temperature. Small-size quarkonia break up at lower temperature.

Helmut Satz et al in 1986 predicted melting of heavy quarkonium states if the temperature of the QGP state is greater than a critical de-confinement temperature $T_c$ [27]. For distances greater than *Debye colour screening* ($\lambda_D$), strong color forces binding $c$-$\bar{c}$ or $b$-$\bar{b}$ pair together becomes screened in QGP resulting in suppression of J/$\psi$ production. Following the above prediction, at CERN NA38 Collaboration indeed observed a suppression in $J/\psi$ production relative to the dimuon continuum [28] but to conclude with certainty

hadronic scenarios cannot be ruled out. At RHIC, $J/\psi$ suppression concluded is depicted in figure 1.10a.

In a sequential melting picture, bound charmonium states with larger size first disappear and ones with smaller size disappear at higher T as depicted by figure 1.10b. The $\Upsilon$ ground state melts at a temperature whuch is around two times the transition temperature.

Experimentally, $J/\psi$ production shows a peak in the invariant mass distribution of lepton pairs arround *3.1 GeV*. Drell-Yan and open charm productions are possible backgrounds which may mask a $J/\psi$ suppression by giving a large contribution to $J/\psi$ region in the invariant mass spectrum.

### 1.4.5 Strangeness Enhancement

Johann Rafelski and Berndt Muller predicted that strange particles would be produced more abundantly relative to other hadrons in the QGP state [29, 30, 31, 32, 33] which could be used as a signature of QGP. The enhancement in strangeness production was predicted to be by a factor of 10-50 [30]. Infact enhancement was seen by different experiments compiled in figure 1.11.

The reasons behind the strangeness enhancement are:

- Higher density of gluons in QGP leads to increase in strange quark production via the gluon-gluon fusion $g + g \longrightarrow s + \bar{s}$ [34]. Inside hadrons gluon density as well as energy density are lower due to the confined volume restricting such reactions.

- Due to chiral symmetry restoration in QGP strange quark mass is significantly lowered making it much easier to produce $s + \bar{s}$ pairs in $q - q$ or in $g - g$ collisions. In QGP which is a chirally symmetric state a quark mass is just its *current mass*, and in a chiral condensate the mass is larger which is called as the *constituent quark mass*.

Among all particle species, strange particles freeze-out chemically at the early stage of system evolution and interacts with quarks of different flavour and eventually appear as a strange hadron in the final state. In dense nuclear matter, strange quarks have very fast chemical equilibration time, of

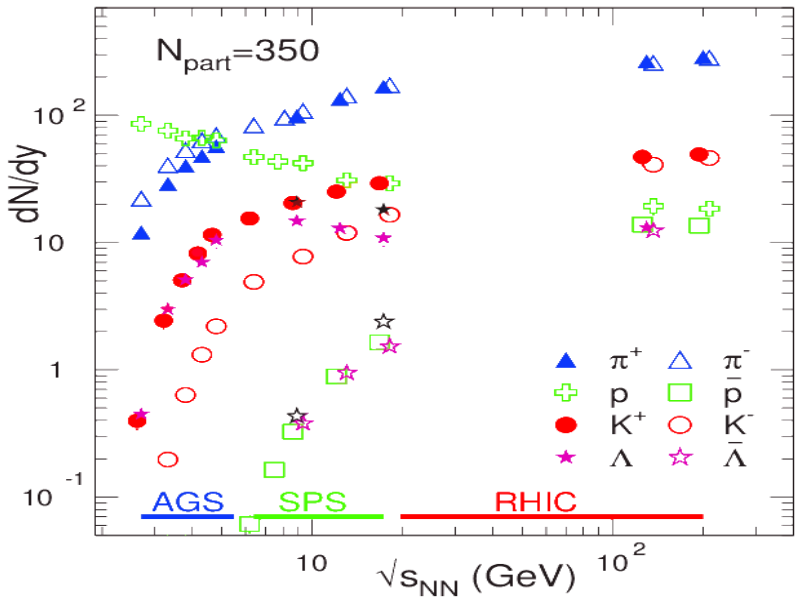


Figure 1.11: Yield of various particles with $\sqrt{s_{NN}}$ at mid-rapidity. The lines are added to indicate the trends. Strange particle yields in nucleus-nucleus collisions at the AGS and the SPS energies indicate a rise with $\sqrt{s_{NN}}$

the order of 5-6 fm/c, which corresponds to the QGP life-time. Production of anti-hyperons is unlikely because incoming beam particles requires interactions involving anti-nucleons. This different behaviour of multi-strange anti-baryons in QGP makes them a strong probe. Infact, WA97 collaboration measurements indeed showed enhanced production of multi-strange hyperons [28].

### 1.4.6 Jet Quenching

When high momentum strongly interacting particle pairs are produced inside the QGP and then one of the particle loses energy in flight through the plasma and may get lost whereas the other particle escapes easily as depicted in figure 1.12a, phenomenon is known as jet-quenching. Figure 1.12a shows two possible scenarios for pair-production in the quark-gluon plasma. On the left, a particle anti-particle pair have momentum almost parallel to the surface of the plasma, and both particles escape without experiencing much drag from QGP. On the right, a particle-antiparticle pair have momentum

roughly normal to the surface, as a result one particle escapes easily while the other moves into the dense inner plasma region and loses most of its energy and probably never making it out upto the detector. Thus jet quenching is epected to show up as a depletion in the yield of $p_T$ hadrons making it a potential probe for the high density deconfined phase transition [35, 36, 37].

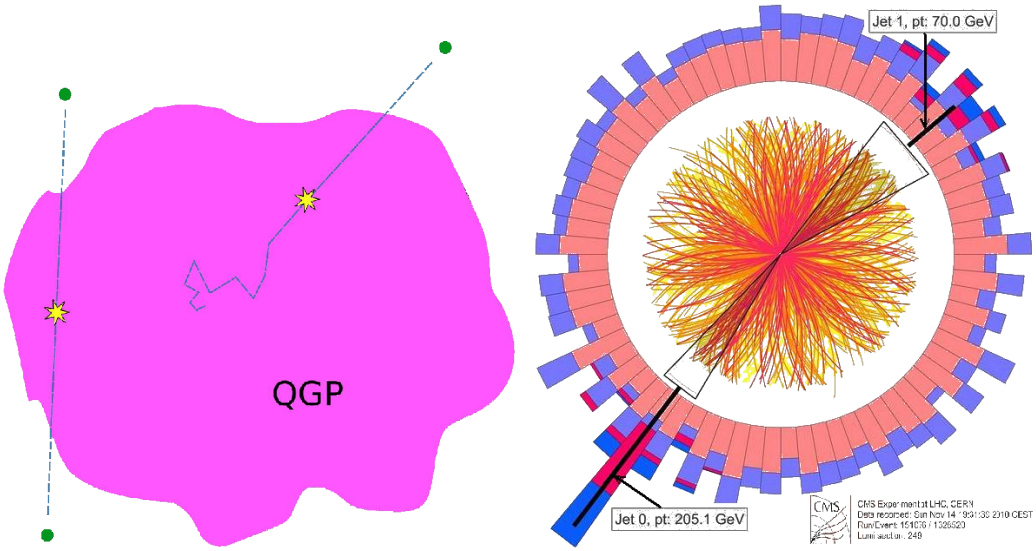


(a) Jet Quenching process (b) Jet Quenching at CMS

Figure 1.12: (a) Jet Quenching Mechanism inside QGP. (b) Jet Quenching at CMS Experiment at RHIC (Copyright CERN ).

The event shown in figure 1.12b is the first lead-ion run of the LHC showing two nearly back-to-back particle jets from a single event. Conservation laws predict their momenta to be the same in magnitude but the jet at the top right falls well short of the bottom left jet. The top right jet seems to have interacted with the QGP and lost its energy by transferring some of its momentum to the particles in the plasma which is resulting in a lower momentum as measured by the calorimeter effect attributed to *jet-quenching* [38].

### 1.4.7 Collective Flow

Collective flow is an important observable reflecting collective properties of nuclear medium created in heavy ion collisions. It gives the information about the Equation of State(EoS) of nuclear matter deflected sidewards from the hot and dense region formed by the overlap of projectile and target nuclei. Collective flow is generated by the pressure gradient in hydrodynamical picture illustrated in figure 1.13a which shows a *sidewards deflection* of the nuclear matter after the collision known as "*sidewards collective flow*". This flow reflects the interplay of collective and random motions of emitted fragments dictated by the thermal energy and is independent of mass after the system is thermalised. On the other hand, due to collective motion fragment energy increases linearly with mass which makes the heavier fragments flow more prominently depicted in figure 1.13b along with model calculation curves showing that the fragment flow is an excellent indication of the underlying flow of nuclear matter. Comparison between the different systems of projectile and target nuclei at different incident energies permit us to determine the incompressibility of nuclear matter.

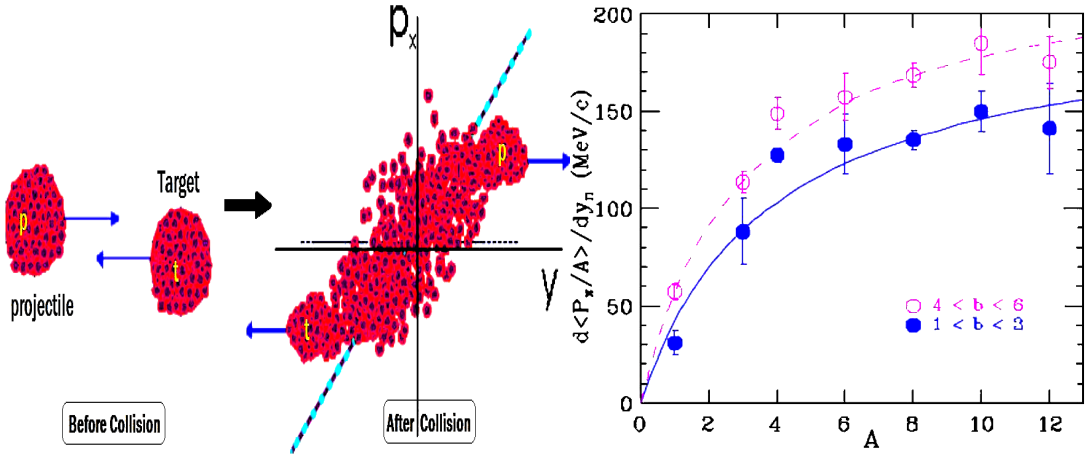


(a) (b)

Figure 1.13: (a) Distribution of nuclear matter before and after collision.(b) Sideward flow increase with fragment mass.

In heavy ion experiments, the Lorentz contracted almond shaped region of a non-central collision generates large pressure gradient in the direction

of impact parameter resulting in an *elliptical* azimuthal particle distribution which is then characterized by the second Fourier coefficient (**v2**) of a Fourier decomposition of angular distributions. Measuring the **elliptic flow** helps to detect the existence of the QGP pressure in the early stage. For the first order phase transition, the pressure remains constant resulting in a vanishing sound velocity, $c_s = \sqrt{\partial P/\partial \varepsilon}$ referred as "*softening of the EoS*". If softening occurs then the collective expansion velocity will be reduced significantly, hence final state produced hadrons are expected to provide the key information about the EoS [39].

### 1.4.8 Fluctuations

Fluctuations of thermodynamic observables are used to study the nature of the phase transition from hadronic to quark gluon plasma created in heavy ion collisions [40]. For first order phase transition large fluctuations in energy density are expected, on the other hand for second order phase transition specific heat diverges. Moreover, near the critical point fluctuations are predicted to be enhanced largely [41]. In experiments, fluctuations of *conserved quantities* like electric charge, baryon number or strangeness are usually studied as they are generated in the early plasma stage of the system created in heavy-ion collisions with quark and gluon degrees of freedom [42, 43]. The fluctuation generated at the partonic phase is expected to increase as the system evolves in time [44, 45]. Fluctuations which are usually studied in heavy ion experiments are:

- *Net charge fluctuations:* Net charge fluctuations have been measured by experiments at SPS and RHIC using different fluctuation measures.
- *Multiplicity fluctuations:* Multiplicities of produced particles characterizes the evolving system and their fluctuation is distinct signal of the QGP phase transition [40, 42].
- *Particle ratio fluctuations:* Relative production of different types of particles produced in the hot and dense matter might be affected during the phase transition. Of particular interest is the strangeness fluc-

tuation in terms of the kaon to pion ratio whose broadening by large in the yields has been predicted due to the differences in free enthalpy of the hadronic and QGP phase. This is probed through the $K/\pi$ ratio fluctuation.

- $< p_T >$ *fluctuations:* The $< p_T >$ of emitted particles in an event is related to the temperature of the system. Thus the event-by-event fluctuations of average $p_T$ can be used to measure the temperature fluctuations in the QGP phase transition experimentally.

## 1.5 Chiral Symmetry Restoration

Besides confinement, another important property of QCD is that the masses of the $u$ and $d$ quarks are small ($\approx 0$) as compared to the relevant QCD scale. Theory which assumes massless quarks with its spin pointing along or opposite to the direction of the motion and preserves this helicity irrespective of the interaction at all times is known as *chiral symmetry* where the conserved spin alignment with the quark's direction of motion can be associated with the right or left handedness respectively for two spin states. Chiral symmetry predicts mirror particle for every particle with the same properties, such as the mass etc., known as its chiral partner under parity transformation. Spectrum of hadrons is expected to group into parity partners with identical properties which is not observed in nature due to the large differences in the masses of chiral partners. Hence, chiral symmetry is observed to be *spontaneously broken* in the nature. For spontaneously broken chiral symmetry, we expect existence of zero mass excitation modes called as *Goldstone bosons* which can be associated with the pions due to their small mass on the hadronic scale. Pions being the lightest hadrons have proper chiral properties. Due to the small mass resulting from $u$ and $d$ quarks which explicitly break chiral symmetry. At high temperatures and/or densities, we expect a phase transition to the chirally restored state which would produce dramatic changes in the properties of certain hadrons in the medium around the phase transition. Particle along with its chiral partner will become alike in chirally

restored medium created in heavy ion collisions.

## 1.6 Detectors in High Energy Experiments

Most of the quark-gluon phase probes are directly undetectable due to their fast decaying nature which needs to be reconstructed via their decay products after freeze-out reaching the sensitive detector element. For fixed target experiment, detectors are located downstream the collision point and surrounded the collision point in colliding beam experiments. Particles coming from the fireball interact with the sensitive detector material thereby their properties comprising momentum, energy, spin, mass, charge, lifetime and identity are measured. The limited kind of particles produced in high energy experiments include photons, electrons, muons, hadrons, neutrinos, etc. Detectors need to be efficient enough so that each and every particle of interest is tagged and identified separately. Detector design is decided by the particle type and its interaction with the matter. Some of the particles relevant at high energy physics experiments along with their properties exploited in detection are: (a) Photons react via photoelectric effect, Compton scattering and pair-production; (b) Charged particles (e.g. $e^{\pm}$, $\mu^{\pm}$, $p$, $\pi^{\pm}$, etc.) interact mainly by scattering (which is unwanted), ionization, excitation, bremsstrahlung, transition radiation and cherenkov radiation; (c) Hadrons whether charged or neutral, also interact strongly through inelastic interaction (e.g. induced fission, neutron capture, etc.). (d) Neutrinos which interact weakly, their 'non-interaction' is signature manifesting as 'Missing Energy'. A detectors sensitive material is used to obstruct the particle path and generates electrical signals later converted into computer bits by Analog-to-Digital conversion. Fig. 1.14 gives a scheme of how the different particles react with the different modules of the CMS detector with the details of the different componets used in detection are as follows:

Tracking detectors (or *Tracker*) in combination with a strong magnetic field is used to measure the track, momentum, charge and energy. Computer optimised algorithms are used to reconstruct the particle trajectories whose accuracy depends on the spatial resolution of the tracker, which is few $\mu$m's

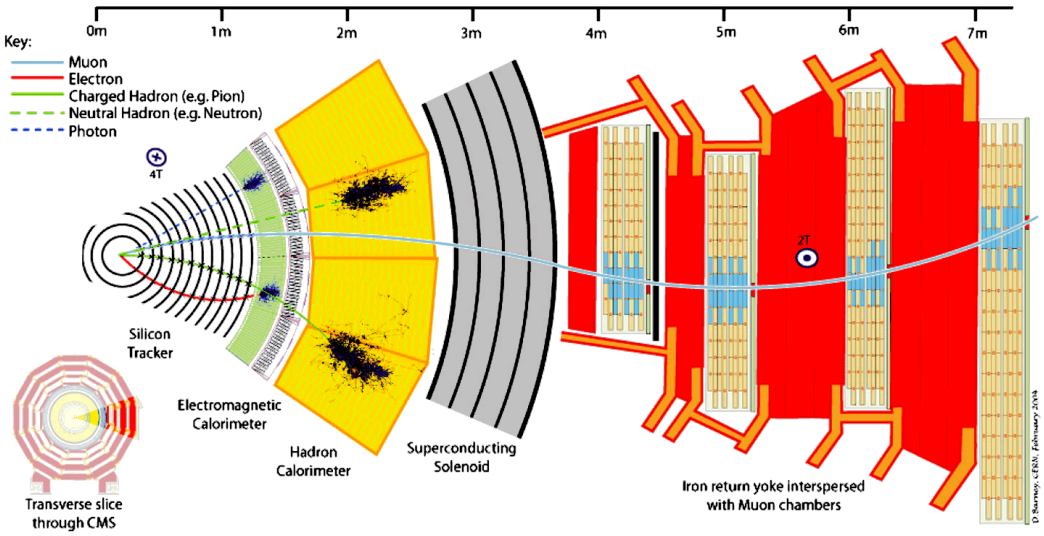


Figure 1.14: A slice through the CMS detector consists of a central silicon Tracker (Pixel and Strips), an Electromagnetic Calorimeter, a Hadron Calorimeter, a Superconductor Solenoid Magnet, a massive iron return yoke instrumented with Muon Chambers. The depicted interactions present an ideal detector behaviour for the different particles $\mu$ , $e$, charged and neutral hadrons, and $\gamma$

for semiconductor detectors, $\sim$100 $\mu$m for gas detector like drift chamber and a few hundreds $\mu$m for Multi-Wire Proportional Chambers (MWPC). The accuracy is also effected by the multiple coulomb scattering inside the tracker.

There are two types of *Calorimeters*: Electromagnetic and Hadronic. Calorimeter is used to measure both the energy and the impact of the incoming particle by determining the electromagnetic and hadronic showers created inside the material by electrons/photons and hadrons respectively. In addition, the deposited energy distribution is used to discriminate different incoming electrons/photons and hadrons.

*Muon detector* made of hadron absorbers and traking detectors detects muons traversed all through the material in the inner detectors. It has an excellent background rejection capability.

*Particle Identification Detector (PID)* is used for identification of different particle species. Transition Radiation Detectors (TRD), Cerenkov Detectors, etc are examples of PID's. TRD can discriminate electrons from hadrons even at high energy region.

All the detectors/sub-detectors are carefully integrated to suit the purpose of the overall resulting apparatus. Fast outputs from sub-detectors/dedicated detectors provide *trigger signals* indicating the occurrence of a particular type of event inside the apparatus. Trigger can be based on spatial and /or temporal correlation of detectors or it can be based on threshold like energy threshold etc.

Experimental data is usually collected via a Data Acquisition System (DAQ) which sends it or part of it to monitoring computer and the recording system. Computers process the data and reconstruct physical events and finally display using graphical routines.

## 1.7 Motivation and Plan of Present Work

The work presented in this thesis is based on the Compressed Baryonic Matter (CBM) Experiment at FAIR GSI Germany. The primary motivation of CBM is to investigate highly compressed cold nuclear matter at very high densities and moderate temperature, such matter exists in the core of the neutron stars and supernova explosion. This approach is complementary to the present experiments like LHC and RHIC which studies matter at high temperatures and low net baryonic densities. In the present work, we have generated simulated data for CBM experiment to optimise and test the performance of the proposed muon detection system. The signal generation like low mass vector mesons and their subsequent decay into muon pairs is done using PLUTO event generator. PLUTO distributes mother particles thermally in $p_T$ and gaussian in rapidity. PLUTO generate dimuon decay events with one multiplicity per event in order to enhance the statistics of the signal. For proper normalisation, the multiplicities of different sources of cocktail are calculated from Hadron-String Dynamics (HSD) model and dimuon branching ratios from Particle Data Ground (PDG) database. Background events are calculated using the UrQMD event generator. In this work we propose the muon detection system for CBM and demonstrate its physics performance in simulation at 25 AGeV collision energy. The muon detector will measure the complete spectrum from low mass vector meson

to charmonia via their muonic decay in Au+Au (gold-gold) collisions. The modifications and dissociation of these resonances in a deconfined medium is one of the promising signatures of QGP formation. For efficient reconstruction of low mass vector mesons and charmonia, muon detector absorber length and material has been analysed. Optimised muon detection system for different energy regions (SIS100 and SIS300) has been demonstrated interms of their physics performance. Finally some physics issues like fluctuation and strangeness production will be discussed in reference to FAIR energies.

The present thesis is organized is as follows: In the current chapter we introduced high energy physics relevant for QGP study. In next chapter, a brief description of the CBM experiment and various detectors including MUCH detector used in CBM experiment are given. Chapter-III discusses about the present status about the di-muonic measurements. In Chapter-IV we present the new muon detection system for CBM experiment. Chapter-V demonstrates the physics performance of the muon chamber for CBM experiment at SIS300 energies. Chapter-VI discusses some physics issues like fluctuation and strangeness production at FAIR energies. Finally in Chapter -VII we summarise all the findings briefly.

# Chapter 2

# The CBM Experiment at FAIR

Many experiment worldwide in high energy are devoted to the investigation matter under extreme conditions. Experiments at RHIC and LHC are exploring the de-confined QCD matter at very high temperatures and almost zero net baryon densities. Experiments like at RHIC (STAR and PHENIX), SPS-CERN, JINR-NICA are investigating the QCD phase diagram at high net-baryon densities and looking for the critical endpoint [46, 47, 48]. Due to low luminosity above mentioned experiments are constrained to look for the bulk observables which are predominantly sensitive to the late and dilute phase when most of the particles freeze out except elliptic flow. In contrast, Compressed Baryonic Matter (CBM) experiment at FAIR will have high beam luminosity and fast detector system to focus on the measurement of rare and diagnostic probes of the early dense phase. This approach will help us to find signatures of partonic degrees of freedom, first order deconfinement phase transition and its critical endpoint, in-medium modifications of hadrons, and nuclear equation of state at high baryonic densities.

## 2.1 The Facility for Anti-proton and Ion Research (FAIR)

The FAIR provides an accelerator facility for a multifaceted science programs which will provide excellent beams in a wide range of intensities and energies

of stable/unstable nuclei as well as of anti-protons [49]. A sketch of the future FAIR along with the existing GSI facilities is shown in Figure 2.1.

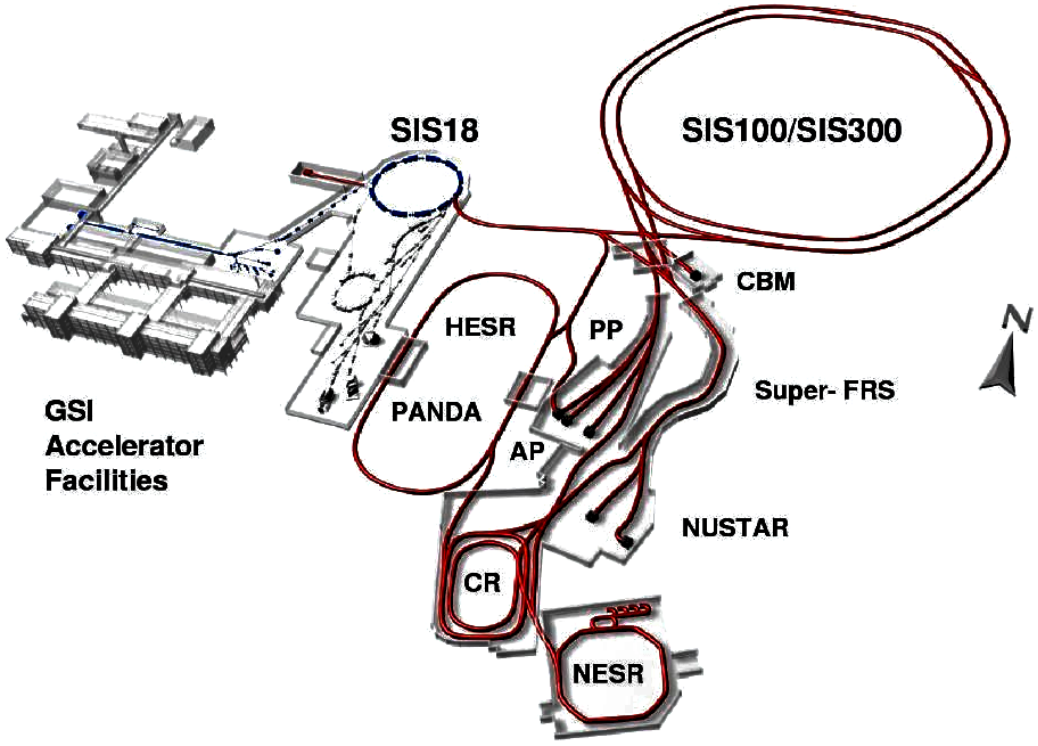


Figure 2.1: FAIR Layout at GSI, Germany.

At present FAIR has low intensity accelerators namely UNILAC and SIS18 but its future upgrade program for high intensities will comprise two new synchrotrons namely SIS100 and SIS300 with about 1000m circumference and 100Tm and 300Tm magnetic rigidities respectively. Existing GSI accelerators will serve as injectors for the new synchrotron. There is a storage cooler ring system, experimental stations including a superconducting nuclear fragment separator (Super-FRS) and an anti-proton production target adjacent to the double synchrotron. There are also Storage ring for anti-protons namely high-energy storage ring (HESR), the collector ring (CR), and the new experimental storage ring (NESR). SIS100 accelerator will be able to deliver energies up to 11 AGeV for Au, 14 AGeV for Ca, and 29 GeV for protons, whereas SIS300 will deliver up to 35 AGeV for Au and 89 GeV for protons to be available two years later than SIS100 for full CBM detector

Table 2.1: Ion species and their kinetic energy per nucleon for a beam rigidity of 100 Tm at the SIS100 and 300 Tm at the SIS300 (E/A is in GeV)

| **Beam** | **Z** | **A** | **E/A SIS100** | **E/A SIS300** |
|---|---|---|---|---|
| **p** | 1 | 1 | 29 | 89 |
| **d** | 1 | 2 | 14 | 44 |
| **Ca** | 20 | 40 | 14 | 44 |
| **Ni** | 28 | 58 | 13.6 | 42 |
| **In** | 49 | 115 | 11.9 | 37 |
| **Au** | 79 | 197 | 11 | 35 |
| **U** | 92 | 238 | 10.7 | 34 |

system. FAIR will also provide rare isotopes and anti-protons beams with high intensity and quality. The FAIR energy regime has only been explored at AGS up to ∼14 AGeV. Multiple research programs can be run in parallel at FAIR like:

1. **CBM** experiment investigating heavy ion collisions at highest baryon densities.
2. **PANDA** detector to investigate hadron physics using cooled high energy anti-proton beams.
3. **NUSTAR** detectors to investigate the structure of unstable nuclei, nuclear astrophysics, plasma physics and atomic physics.

SIS100 and SIS300 synchrotrons with deliver beams to HADES and CBM. The kinetic beam energy per nucleon depends on the bending power **B.r** of the dipole magnets [$E/A = \sqrt{(0.3 \times B.r \times Z/A)^2 + m^2} - m$, where Z and A are the charge and atomic number of the ion, and $m$ the mass of the nucleon]. The beam possible energies for the maximum beam rigidity of SIS300 (**B.r** = 300 Tm) are listed in Table 2.1 for different ion species [50].

### 2.1.1 Experiments at SIS100 Accelerator

FAIR research program will built accelerator at SIS100 in first phase to deliver energies up to 11 AGeV for Au and 29 GeV for protons suitable to

study the properties of dense baryonic matter. Transport calculations shows that energy densities up to 2.5 GeV $fm^{-3}$ and baryon densities of 2-7 times normal nuclear density $\rho_0$ are expected in the center of the reaction zone, conditions which prevail in core supernova and neutron stars. The experiments at SIS100 will try to shed light on following fundamental topics:

- Dense baryonic matter and its electromagnetic structure.
- Hadron properties in dense baryonic matter.
- Chiral symmetry restoration at very high baryon densities.
- Equation-of-state of nuclear matter at neutron star core densities.
- Relevant degrees-of-freedom in the vicinity of the de-confinement phase transition.
- Strange matter in the form of heavy multi-strange objects.
- Charm production at threshold beam energies.
- Charm propagation in nuclear matter.

HADES research program will measure electron-positron pairs to look for the in-medium modifications of low mass vector mesons. PANDA research program will investigate production mechanism of charm anti-charm pairs at threshold energies, their properties at saturation density using proton beam energies up to 29 GeV, and their propagation in cold nuclear matter by varying the target nucleus size. The yields, spectra and collective flow of (multi-) strange hyperons will be done using STS tracking detector inside a dipole magnetic field along with a time-of-flight (ToF) wall. The identification of open charm (D-mesons) requires the CBM start version along with a micro-vertex detector (MVD) for reconstruction of displaced vertices. Identification of charmonium from SIS100 version of CBM muon detection system will be carried in nucleus-nucleus and proton-nucleus collisions.

### 2.1.2 Experiments at SIS300 Accelerator

FAIR research program will install accelerator at SIS300 after two years of SIS100 in second phase which will deliver energies up to 35 AGeV for `Au` and

89 GeV for protons. The most promising observables in the SIS300 energy range are:

- Particles containing charm quarks (open charm, charmonium) to probe the highly compressed baryonic matter.
- Low-mass vector mesons dilepton decays carrying information on hadron properties in the hot and dense fireball.
- The collective flow of identified hadrons carrying the information on the equation-of-state of hot and dense matter.
- Kaons, hyperons and hadronic resonances carrying strange quarks sensitive to the fireball evolution.
- Event-by-event dynamical fluctuations and correlations of particle multiplicities and momenta are to study a first order phase transition or the critical endpoint.
- Photons to get the direct radiation information from the early fireball.

Key feature of the CBM experimental program is to have systematic and comprehensive measurement of excitation functions and system size dependencies of all observables. Particular emphasis is on rare probes, not accessible to other experiments in this energy range, by using high beam intensities, a large duty cycle, excellent beam quality, and several months per year running time. Full azimuthal coverage in a wide acceptance of rapidity and transverse momentum and excellent centrality determination is required for event-by-event fluctuations observable [50].

## 2.2 CBM Detector Concepts

Primary job of the CBM experiment will be to measure particle multiplicities, phase space distributions and flow of certain particles like protons, pions, kaons, hyperons, hadronic resonances, low mass vector mesons, charmonium and open charm including their event-by-event fluctuations and correlations in heavy-ion collisions at FAIR. The technical challenge of the CBM experiment is to filter out rare probes at reaction rates $\sim$10 MHz [51] with charged

particle multiplicities ∼1000 per event which require extremely fast and radiation hard detector (and electronic) components. Moreover, the experiment will provide lepton identification (both electrons and muons for reliable results), determination of high resolution secondary vertex, and a high speed trigger and data acquisition system [49]. The CBM experimental setup is sketched in Fig. 2.2. Details of the different modules of CBM detector is

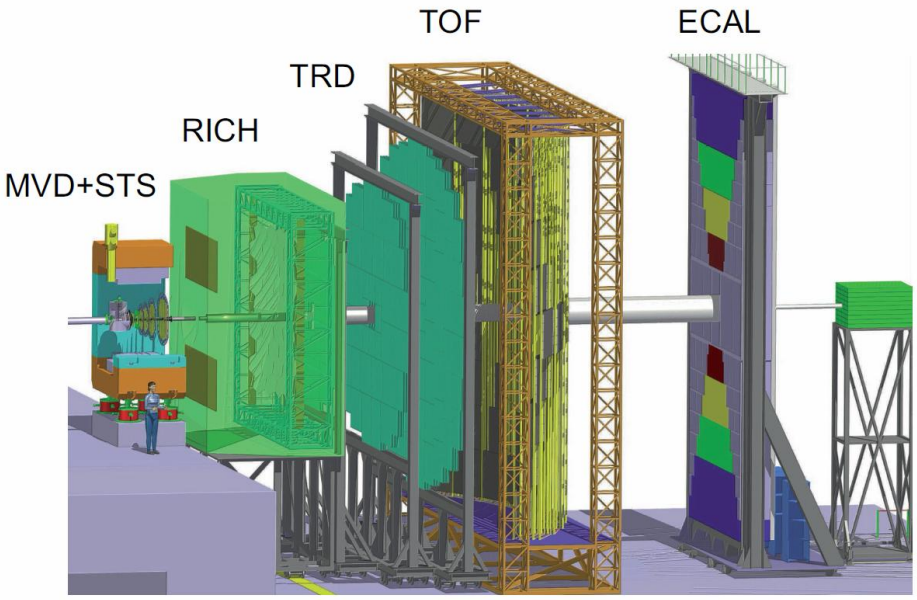


Figure 2.2: The CBM experiment set-up consists of a large acceptance dipole magnet, radiation-hard Silicon pixel/strip detectors (STS, MVD), a Ring Imaging Cherenkov detector (RICH) and Transition Radiation Detectors (TRD), Resistive Plate Chambers (RPC), an Electromagnetic Calorimeter (ECAL), and a Projectile Spectator Detector (PSD).

given below:

- **STS and MVD:** The primary component of the experiment will be a silicon tracking system installed in a large acceptance dipole magnet which allows track reconstruction in a wide momentum range from about 100 MeV up to more than 10 GeV with a momentum resolution of about 1%. The Micro-Vertex Detector (MVD) is needed along with STS to determine secondary vertices for D-mesons close to the target with high precision. The STS has 8 detector stations placed from 30 - 100 cm distance from the target based on low-mass silicon micro-strip

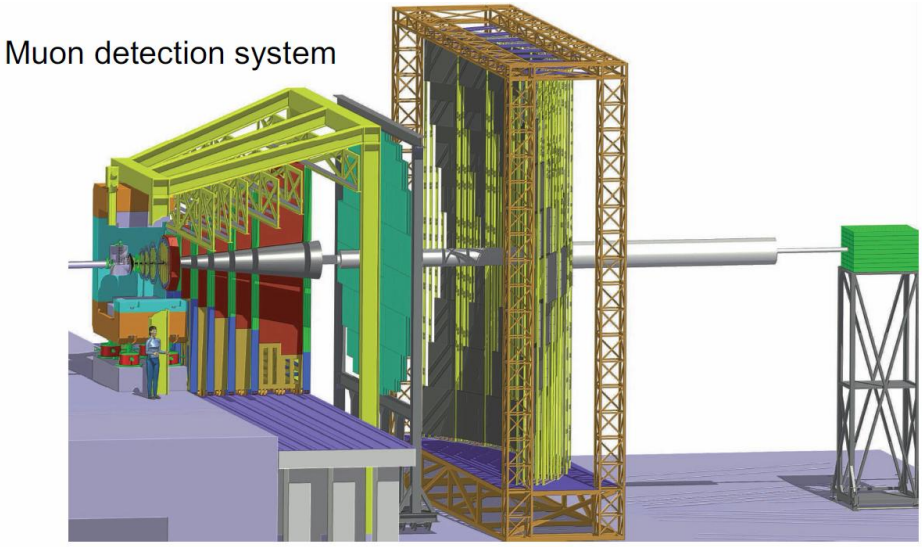


Figure 2.3: The CBM experiment set-up with a muon detection system (MUCH) with alternating hadron absorbers and detector layers, to be put in place of RICH.

detectors for the track point measurement. The stations are of ladder structure build of 300 $\mu m$ thick double-sided silicon micro strip sensors and 60 $\mu m$ strip pitch read-out electronics placed at the perimeter. Signals from sectors are sent through thin capton micro-cables to the front-end boards. MVD on the other hand consists two detector stations installed in a vacuum vessel located at 5 and 10 cm (alternatively 10 and 20 cm) downstream the target. Monolithic Active Pixel Sensors (MAPS) of pixel size of 40 x 40 $\mu m^2$ provides a high spatial resolution of 3 $\mu m$, and a thickness of 100 $\mu m$ (very thin) is what's needed to measure the displaced vertices of D-mesons.

- **RICH:** The measurement of electrons will be performed with a Ring Imaging Cherenkov (RICH) detector (for momenta below 8-10 GeV/c) together with Transition Radiation Detectors (TRD) with momenta above 1.5 GeV/c. RICH would be positioned behind the magnet and in front of the first transition radiation detector (TRD) in current CBM Layout. Pion suppression of about 100-1000 is expected by the RICH alone out of total pion suppression of 10000 required from all detectors. High detection efficiency of electrons mean 10-15 hits per electron ring

at minimum. As global tracking connects tracks in the STS and TRD and then the RICH which require it should not extend beyond $3m$ and it should have a material budget about 3-4 % radiation length for reduction in multiple scattering. A large acceptance of $25^o$ will make it able to cover the vector mesons in a wide range of rapidity and transverse momentum.

- **TRD:** Transition Radiations (TR) are X-rays of energy 10 KeV produced when ultra relativistic particles cross the boundary between two media with different dielectric constants $\epsilon$'s. CBM experiment uses TRD to separate pions from electrons because of the fact that pions do not produce any TR. TRD in CBM will comprise of 3 stations, located at approx. 5 m, 7.2 m and 9.5 m downstream the target, each consisting of 3-4 detector layers for particle tracking and electron-positron identification with $p > 1.5$ GeV/c ($\gamma > 1000$). The TRD readout will consist rectangular pads to give a resolution of 300-500 $\mu$m across and 3-30 mm along the pad and every second TR layer is rotated by $90^o$ [50]. Prototype TRD gas detectors have used MWPC and GEM technologies with good results.

- **MUCH:** Muons will be measured with an active hadron absorber system consisting of iron layers and muon tracking chambers (MUCH). For muon measurements the MUCH will be moved to the position of the RICH as shown in Fig. 2.3. Brief details about the MUCH will be given in the section-2.2.1.

- **TOF:** Charged hadron identification will be performed by a time-of-flight (TOF) measurement with a wall of RPC's located at a distance of 10 m behind the target. The TOF wall consists of approximately 60,000 independent cells giving a resolution of $\sigma_{TOF} \leq 80$ ps [52]. Start signal for ToF measurement is provided by a diamond pixel or micro-strip detector. The tRPC (timing Resistive Plate Chamber) with 25-$30^o$ coverage has been considered as an option for ToF provided it is able to handle rates $\sim$20 kHz/cm$^2$ and the FEE (Front End Electronics)

process the signals at an interaction rate ∼10 MHz. First prototypes with glass electrodes gives an efficiency of 95% with time resolution of 120 *ps* at rates of 18 kHz/cm$^2$ [53] and separation of kaons and pions is achieved up to 3.5GeV/c laboratory momentum while protons could be identified up to 7GeV/c.

- **ECAL and PSD:** Electromagnetic Calorimeter (ECAL) a complementary in the set-up in selected regions of phase space gives information about photons and neutral particles. Projectile Spectator Detector (PSD) is used for the collision centrality determination and the reaction plane orientation. The PSD is a compensating, modular lead-scintillator calorimeter which measures nucleons from the projectile nucleus which do not interact. It consists $12^9$ modules each consisting of 60 lead-scintillator layers. The photons produced in the scintillator are measured by multi avalanche photo diodes (MAPD) having size of 3×3 mm$^2$ with $10^4$/mm$^2$ pixel density [54].

### 2.2.1 The Muon Chamber System (MUCH)

The measurements of $J/\psi$ and low mass vector mesons ($\rho,\ \omega,\ \phi$) in heavy-ion collisions are key probes of deconfinement, in-medium modification of hadrons and chiral symmetry restoration at high baryonic densities ($\rho_b$). While looking to their di-muonic decays, the experimental challenge at FAIR energies is to identify low-momentum muons in a high multiplicity particle environment [55].

At CBM, idea is to track the particles through a hadron absorber system to perform a momentum-dependent muon identification realized by segmenting the hadron absorber in several layers, and placing triplets of tracking detector planes in between the gaps. The detector system is placed near the target downstream the STS and made as compact as possible to reduce meson decays into muons. The standard muon detector system to be used at SIS300 consists of 6 hadron absorber layers and 18 gaseous tracking chambers in triplets behind each absorber as shown in Fig. 2.4. First absorber faces the harsh radiation condition and it has been choosen of carbon 60 cm, for

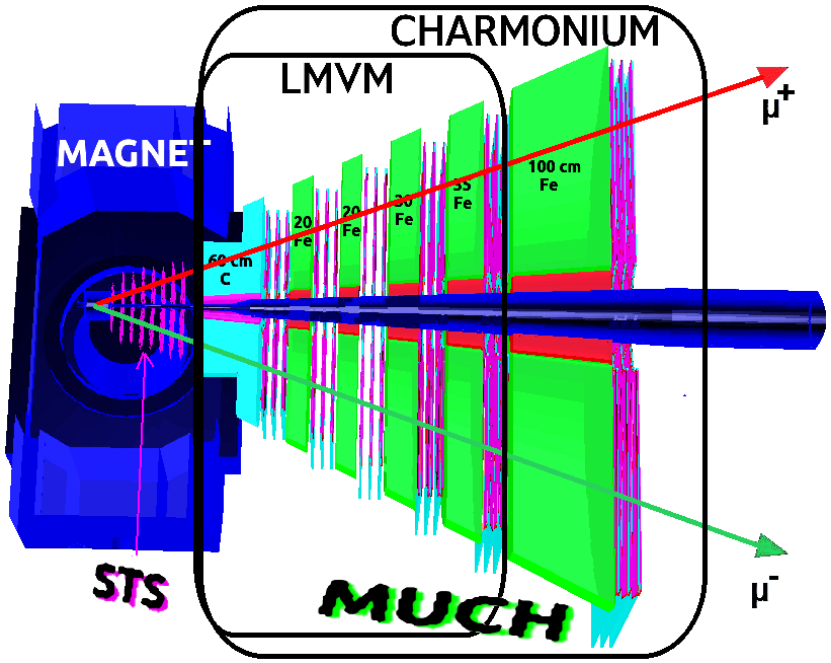


Figure 2.4: The CBM muon detection system consisting of alternating layers of iron hadron absorbers accept first one which is of carbon and detectors for low mass vector meson and charmonium detection via di-muonic channel.

the reasons discussed in detail in the chapter-4, while rest of the absorbers are made of iron material. The definition of a type of signal muon depends on its momentum, mass, and beam energy. For example, for SIS300 beam energies, muons from $J/\psi$ have to pass all 6 absorber layers with a total thickness of 265 cm (carbon 60cm + iron 205cm) which corresponds to 13.4 $\lambda_I$ (nuclear interaction length) whereas, muons from low-mass vector mesons have to penetrate only 5 hadron absorber layers with a total thickness of 165 cm which corresponds to 7.5 $\lambda_I$. Due to huge particle density in front of first absorber/detector, fast and highly granulated gaseous detectors based on GEM (Gas Electron Multiplier) technology have to be used at least for first two stations [56]. The low particle multiplicities behind the muon absorbers makes it easy to implementation trigger on muon pairs to select tracks with good vertices which would reduce the event rate considerably [50].

India will contribute 50% of the muon detector parts and 100% for its electronics. Indian-CBM collaboration is performing R&D work for detector

options at various places. Possible option is to use high resolution fast gas detectors (GEM) at first few stations where particle density is very high and the use of straw tubes at later stages. Technical Design Report (TDR) for MUCH construction has been approved and presently production of different detector components at large scale is going on.

We will discuss about the approved version of the muon detection system for CBM experiment in coming chapters-4 & 5 in details. Here we will briefly discussed about some of the detector technologies that will be used by the MUCH.

**Gas Electron Multiplier (GEM)**

Introduced by F. Sauli in 1996, GEM technology has been used frequently in high energy and medical detectors for the amplification of signal in gaseous detector. GEM consist of a thin polyimide (Kapton) foil about 50 $\mu$m thick coated with copper layer on both sides. The structure perforated with holes, arranged in a hexagonal patter, having 70 $\mu$m diameterand a pitch of 140 $\mu$m typically. Holes get a double conical shape with an inner diameter of about 55 $\mu$ due to chemical itching [57]. Fig. 2.5 shows a picture of a GEM taken with an electron microscope.

The working principle of a GEM is illustrated in Fig. 2.6. When a voltage of a few 100 V is applied between the two copper coatings, field lines are focused through the holes with a strength of the order of 10 kV/cm and each hole acts as an independent proportional counter. Electrons released on the top via ionisation etc. drift into the hole and gets multiply in avalanche till it transfers to the other side resulting in high gas amplification. An good fraction of electrons of the avalanche emerging from the hole to the gas gap can be used for amplification in the subsequent stages. In a single GEM amplification up to $10^3$ is achievable but we can achieve higher amplification by cascading multiple successive GEM. The field configuration is choosen such a way so that most electric field lines end towards cathode side and most of the lines go into the direction of the anode on other side. Most of the gas amplification ions are pulled and collected on the GEM surface while most

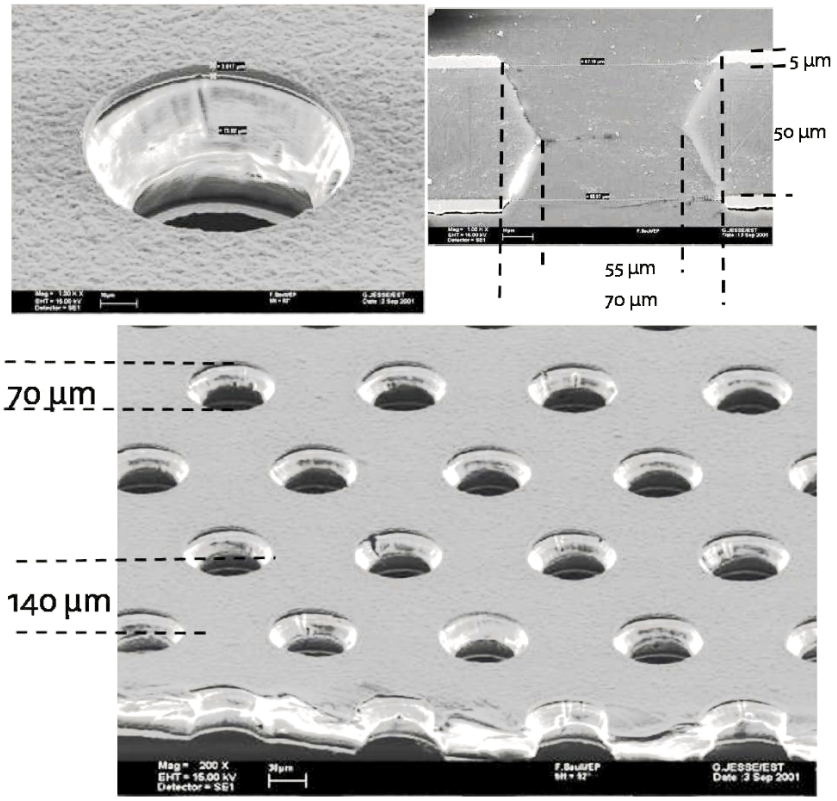


Figure 2.5: GEM structure when viewed in an electron microscope.

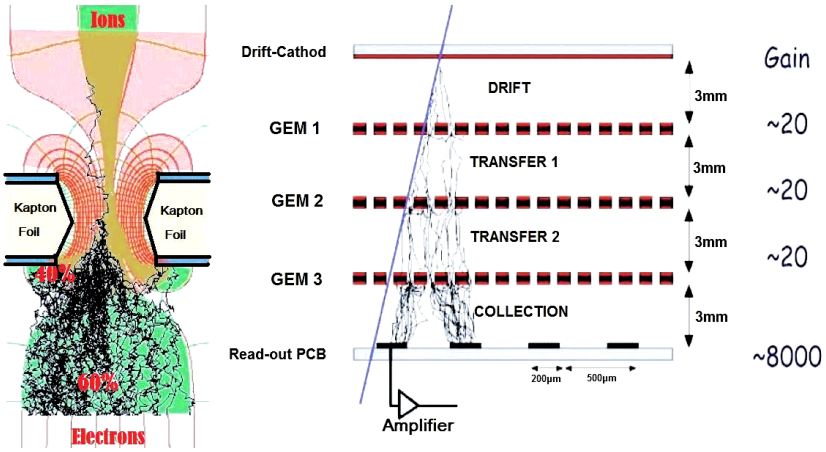


Figure 2.6: (left) pictorial representation of amplification inside the detector under high field inside the hole. (right) working of triple GEM detector.

electrons are extracted out of the GEM holes towards the anode. Applying magnetic field perpendicular to the GEM plane can intensify electron extrac-

tion same way as in TPC (Time Projection Chamber). The electrons due to their light mass tend to follow magnetic field lines while the ions follow the electric field lines due to their heavy masses.

### Straw Tube Tracking Detector

The straw tube is a proportional counter, a gas filled cylindrical tube of aluminized Mylar as a cathode and 20 $\mu$m gold plated tungsten wire stretched along the cylinder axis as an anode as shown in figure 2.7a. Mylar is the preferred because of its higher Young's modulus and a higher tensile strength as compared to Kapton. Straw tube detector can give spatial resolution of about 200 mm in a large volume operating under vacuum conditions. It can reduce the detector mass and inactive parts to decrease straggling and interactions of the particles.

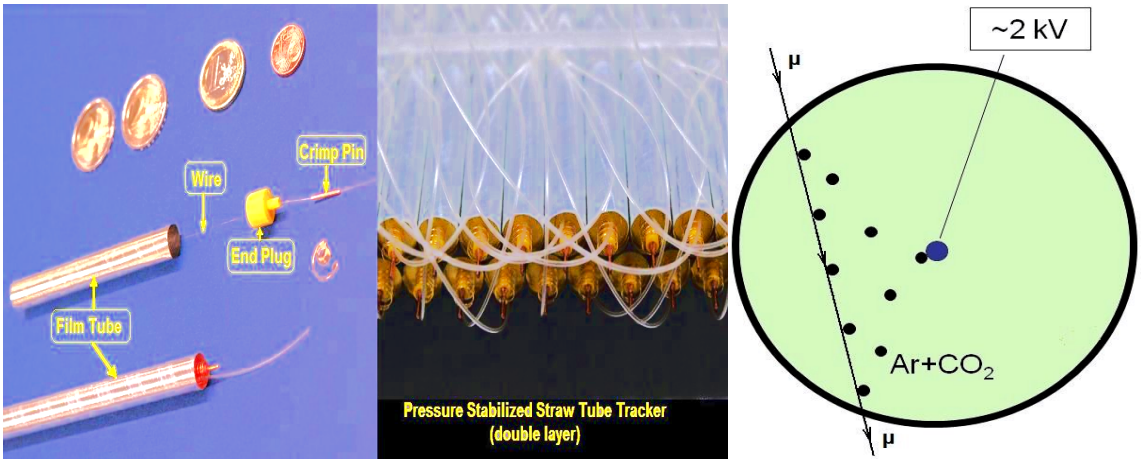


(a) (b)

Figure 2.7: (b)Straw tube parts (b)Working of Straw tube proportional gas detector

Charged particle track passing through the straw tube ionizes the gas (Ar: $Co_2$) molecules and stripped off electrons drifts towards the anode wire as depicted in the figure 2.7b. Inside the tube excess pressure of 1 bar is used to create the necessary wire tension, by creating 7.85 N axial force, and mechanical stability by make the tubes self-supporting. The full detector consisting of 3000 straws with each having mass less than 2.5 g resulting

in total mass of about 7.5 kg. Modularity structure of the detector system allows convenient repairing of defective components of detector geometry. The endcap, made of PVC because of low density and good gluing property, holds as well as centers the anode wire and includes the gas connector. The anode wire is centered with a 1 mm thick copper sleeve and an inner hole of 100 mm is glued into the endcap.

The production technology has been developed for the straw detector of the COMPASS experiment [138] at CERN-SPS, and further improved for the ATLAS TRT at LHC [139]. The fifth MUCH detector station is proposed to consist of 3 double straw-tube layers which are rotated with respect to each other by 10 degrees. Straw tubes may also be an option for the detector station number six.

### 2.2.2 Electronics for MUCH

High rate front end electronics along with its integration without large dead space and heat dissipation is a technological challenge. The electronics including FEE (front end electronics) need to be radiation hard, and highly integrated for cost reasons. CBM will design fast Application Specific Integrated Circuits (ASICs) for most of the detectors of the set-up. A *self-triggered* ASIC version having both *analog and digital readout* named **as "n-XYTER"** will be used for readout as shown Fig. 2.8. n-XYTER is a front

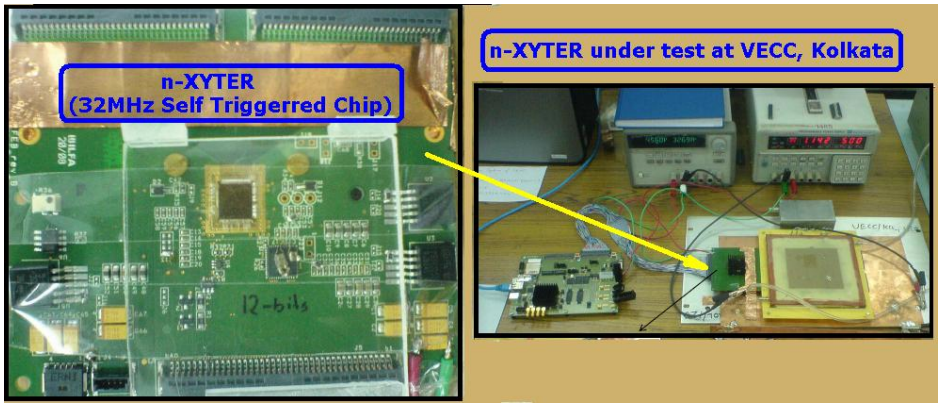


Figure 2.8: (left)n-XYTER for CBM. (right) n-XYTER under test at VECC

end ASIC with 128 channels (integrated mixed signal) [58, 59], each channel

equipped with charge sensitive pre-amplifier and shaper circuitry for capturing incoming signals of either preset polarity asynchronously. Analogue pulse height and a digital time stamp are stored in a short *fifo* (first in first out) for every channel, where it will remain until read out. Data is read through a token ring structure out of the *fifos* un-prejudicially whichever channel has data and skips non-hit channels. For time stamp determination, it has a fast channel of 20 *ns* trigger time while it has a slow channel for charge measurement and it can read-out data at 32 MHz rate [60].

The n-XYTER receives analogue data directly from the sensors to detect the signal peak value and the exact time and provides time stamp digitally whereas the peak value is in analog form. Analog data is converted into digital form by an ADC (analog to digital converter) which consumes time, as a result the correlation between time stamp and signal value is lost which need to be recombined. Transferring the measured data, controlling of the n-XYTER's functional behaviour and the ADC is done by the ROC (Read out Controller) board as depicted in Fig. 2.9.

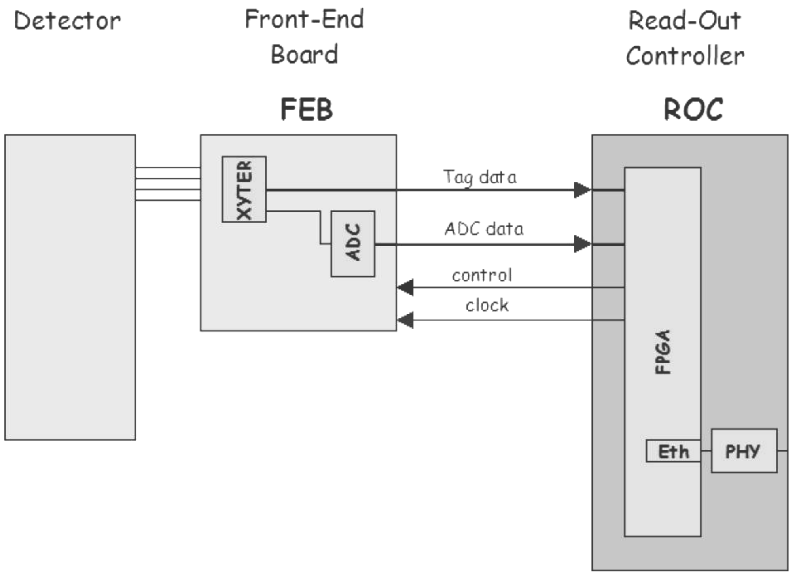


Figure 2.9: The FEE with ROC

Main task of the ROC is to prepare clock signals for the n-XYTER and ADC with well defined frequencies and phase relations to each other. This

is a very sensitive point, as the ADC converts the data exactly at its clock's rising edge with time slot for the conversion being just about 3 $ns$. It is possible to change the delay at runtime from 0 - 31 $n$s (full clock cycle is 32 $n$s) in steps of 1 $n$s manually at the moment [61].

### 2.2.3 Data Acquisition System (DAQ)

CBM expects a beam intensity of $10^9$ ions/s with just 1% interaction probability in the target, high event rates around 10 MHz is realised in central Au+Au collisions. For 1 GB/s bandwidth and 40 kB average event for minimum bias Au+Au collisions, data acquisition system will accept an event rate of 25 kHz. So, online event selection system is required to reject less interesting events. Online software and hardware will archive only one in 400 events for event rate of 10 kHz making ensure that interesting rare events are not lost and there is reliable extraction of cross sections.

The on-line event selection system will be based on a fast on-line event reconstruction algorithms running on a PC farm equipped with multi-core CPU's and graphics cards. Track reconstruction, which is a most time consuming task, will be based on parallel track finding and fitting algorithms implementing the Cellular Automaton and Kalman Filter methods depending upon the interested event rates realised from the detector. Parallel programming, using languages like CUDA, Ct & OpenCL, will be used on the heterogeneous CPU/GPU on-line event selection system.

Trigger on open charm production requires high speed tracking and event reconstruction in the STS and MVD to search secondary vertices on-line. For J/$\psi$ mesons, highest suppression factor is required and only allowing a high-energetic electron or muon pairs in the TRD or MUCH respectively. For low mass vector meson electron-positron pairs, no online selection is possible due to the large number of rings/event in the RICH caused by the STS material budget whereas for low mass vector meson muon pairs some background rejection seems to be feasible on the trigger level.

# Chapter 3

# DIMUON MEASUREMENT

Electromagnetic probes have one of the advantage of not being affected from strong interactions while traversing through hadronic medium. This is why dileptons are used to access a large variety of physics observables in heavy ion collision experiments. Problem with the dilepton production is the small production crossections and various dilepton source partial overlap. So far, no di-lepton data is available in the FAIR energy range (2 - 40 A GeV). Challenges in dilepton measurements is to suppress the huge combinatorial background of lepton pairs. For muon measurements, the background is generated by weak decays of pions and kaons, by mismatches of hadrons upstream and muons downstream the absorber, and by punch through hadrons (showers created by hadrons in absorber which "*leak*" through thin absorber). In this chapter we will briefly review our present knowledge on dilepton physics based on the results of the NA60 experiment which represent the most precise dilepton data measured so far in heavy-ion collisions.

## 3.1 Muons

Anderson and Nedermeir in 1936 discovered muon in cosmic rays. Muon has a mass of 105.658389 MeV, lifetime($\tau$) 2.19703 $\mu$s and it decays via electronic channel [$\mu^{-+} \rightarrow e^{-+}\ \overline{\nu}_e\ \nu_\mu$]. Two main muon sources are: (a)*Cosmic Rays:* Approximately $10^2$ muons/(m$^2$×s) reach ground with energy E >1GeV. (b)*Accelerators :* Low $p_T$ muons are products of mesonic decay and high $p_T$ muons are prod-

ucts of heavy object decays like $J/\psi, \Upsilon, b(quark), W/Z$, etc.

Muons are usually identified by their large penetrating power with precise energy measurement by calorimeter and momentum measurement in magnetic spectrometers. Detectors used for muon measurement consists of hadron absorbers in between tracking detector system to record "*prompt*" muons from the original reaction, decay products in flight, or punch through hadrons. Bending muons in air rather than in iron, after target in fixed target experiment and in central tracker in collider experiment, improves momentum resolution. Thick absorber is installed to absorb the background particles from accelerator beam losses, spectator interactions with accelerator and detector equipment and neutrons etc. Absorber is made of *steel* to catch hadrons, *poly-materials* to absorb neutrons, and *lead* to reduce gamma fluxes.

## 3.2 Dimuon Sources

Di-leptonic decays of the $\eta$, $\eta^{'}$, $\rho$, $\omega$ and $\phi$ mesons are the dominant processes in the low mass region of dimuon mass spectrum, whereas, Drell-Yen and quarkonia are the dominant source in intermediate and high mass region respectively. Most interesting dimuon sources are discussed briefly below:

- **Quarmonium States**
  Dilepton production of heavy quarkonium states ($J/\psi, \psi^{'}$ and $\Upsilon$ etc) provide important information about the deconfined partonic medium. Quarkonium states called as the *external probes* are produced essentially by primary parton collisons before QGP like medium is formed if any. When they pass through the subsequent deconfined medium dissociation of states occurs resulting in suppression in quarkonium yields [27] because partonic medium requires harder gluons than those present in hadrons. Whereas quarkonia regeneration is expected to dominate with higher energies due to statistical recombination of $q\bar{q}$ pairs emerging from the medium, as more number of heavy quarks are produced at higher energies. In fact, instead of suppression of J/$\psi$ an

enhancement is observed at LHC [62]. Important quakonium states relevant at FAIR energies are :

*Charmonium J/$\psi$ :* First excited state of charmonium ($c\bar{c}$) discovered in 1974. J/$\psi$ has a spin 1 (J=1), odd parity, rest mass of 3.0969 GeV/c$^2$ and mean-life time $7.2 \times 10^{-21}$ s. J/$\psi$ has significant leptonic branching ratio (J/$\psi \rightarrow\ l^+l^-$) as hadronic modes are suppressed. Due to the same reason lifetime is about a thousand times longer than expected. In heavy ion collisions J/$\psi$ are produced at hadronisation which actually are produced as a coalescence of earlier created $c$ and $\bar{c}$ quarks in coalescence picture. J/$\psi$ can be suppressed by two effects namely (1) *'normal'* or (2) *'anomalous'* effect. Various contributions leading to normal J/$\psi$ suppression are:

- $D\bar{D}$ **threshold:** Number of primary J/$\psi$ particles are proportional to the number of directly produced $c\bar{c}$ pairs ($N_{c\bar{c}}$) with invariant mass below $D\bar{D}$ meson threshold. When the collision energy increases then the number of subthreshold pairs in total number of $N_{c\bar{c}}$ decreases.
- **Scattering :** Inelastic interaction of initially produced J/$\psi$ with colliding nuclei reduces its number which is more towards central collisions.
- **Co-Movers :** Secondary hadrons created in nucleus-nucleus collisions called co-movers destroying J/$\psi$, effect which is more prominent with increase in number of participant nucleons ($N_p$) and $\sqrt{s}$.

Whereas, dissociation of J/$\psi$ due to QGP formation at large $\sqrt{s}$ and $N_p$ leading to J/$\psi$ suppression is called *'anomalous J/$\psi$ suppression'*. At large incident energies like at RHIC and LHC J/$\psi$ regeneration will be dominant over J/$\psi$ dissociation leading to its enhancement and vice-versa for lower energies.

- **Low Mass Vector Mesons**

  Low mass vector mesons $(\rho, \omega, \phi)$ are important probes of in-medium modification in heavy ion collision. Strangeness enhancement estimation can be obtained from the $\phi$ yields [29, 64]. $\rho$ having very short lifetime, decays inside the QGP, hence giving the information about the chiral symmetry restoration [65]. Brief details of some LMVM's are given here:

### $\eta$ and $\eta^{'}$ mesons

The eta $(\eta)$ was discovered in pion-nucleon collisions at the Bevatron in 1961 by A. Pevsner et al. [131] and $\eta^{'}$ was discovered by two groups, Kalbeisch et al. [132] and Goldberg et al. [133], simultaneously in 1964 [66]. The $\eta$ is a pseudo-scalar mesons with spin $J = 0$ and -ve parity. The $\eta$ and $\eta'$ are made from mixing of up$(u)$, down$(d)$ and strange$(s)$ quarks with $11.5^o$ mixing angle. Mass of $\eta$ and $\eta^{'}$ are 547.853 $\pm$ 0.024 MeV, and 957.78 $\pm$ 0.06 MeV respectively. These particles have direct muonic decay channel as well as Dalitz channel:

$$\eta(\eta^{'}) \longrightarrow \gamma^{*}\gamma \longrightarrow \mu^{+}\mu^{-}\gamma \qquad \text{(Dalitz decay)}$$

The two-body decay of pseudo-scalar meson $\eta^{'}$ is strongly suppressed because of its low mass.

### $\rho$, $\omega$ and $\phi$ mesons

*Rho ($\rho$) and Omega ($\omega$):* Rho meson has a same quark composition as that of pion$(\pi)$, hence sometimes called as excited state of pion due to its mass which is 5.5 times higher than pion mass but quarks composing these mesons have spins which are parallel aligned while poin quarks have anti-parallel spins. Rho has a mass of 770 MeV, spin $J = 1$ and a very short life ( $4.5{\times}10^{-24}$s) with decay width having shape different than Breit-Wigner form. Mostly $\rho$ decays into pions with 99.9% branching ratio but it can also decay via leptonic channel with branching ratio $5{\times}10^{-5}$. Whereas, $\omega$ has a mass of 782 MeV with

life time $8 \times 10^{-23}$ s and, hence, its spectral function shows sharp peak. Quark composition of these particles are:

$$\rho = \frac{1}{\sqrt{2}}(u\bar{u} - d\bar{d})$$
$$\omega = \frac{1}{\sqrt{2}}(u\bar{u} + d\bar{d})$$

*Phi ($\phi$) meson:* Phi meson is a pure $s\bar{s}$ state having mass of 1020 MeV which a large mean lifetime ($\sim 20^{-23}$s) resulting in very narrow width. Phi meson (as strangeness) enhancement is considered one of the important signature of QGP formation in heavy ion collisions. Phi meson decays mostly into kaon pairs, whereas leptonic decay channel is also an important one.

Medium created in heavy ion collisions may change kaons and phi meson masses. If there is decrease in mass of kaon $(K + \bar{K})$ pairs than $\phi$, which is reflected as broader phi spectrum and vice-versa is prohibited. Kaon pair$(K^+K^-)$ final state interactions limit the detection of only those $\phi$ mesons that decay at the time of freeze-out (outside fireball) while leptonic channel has an advantage of containing the information of $\phi$ meson decayed inside the hot and dense fireball created in heavy ion collisons.

Apart from direct muonic decay channel for all low mass vector meson sources, $\omega$ also has a Daltiz decay channel as:

$$\omega \longrightarrow \gamma^*\pi^0 \longrightarrow \mu^+\mu^-\pi^0 \qquad \text{(Dalitz decay)}$$

- **Thermal Electromagnetic Radiation**

  Thermal electromagnetic radiation converted into lepton pairs (and photons) from newly created partonic medium in heavy ion collision is another important source. Hence, di-leptons can serve as thermometer of the newly formed medium. Thermal lepton pairs are emitted all over the course of the collision, and, hence, can provide an information about the temperature evolution. Di-lepton spectra from QGP is expected to

be observed superimposed on the Drell-Yan contribution in the mass region between $\phi$ and $J/\psi$ [67]. Isolating a possible thermal component from hadronic contributions is quite challenging, experiments like at SPS-CERN and at RHIC have done with good precision.

- **Drell-Yan contribution**
  When hadron-hadron scatter in heavy ion collisions, a quark of one hadron and an anti-quark of another hadron can annihilate by creating a virtual photon or Z boson which then decays into leptons pairs. It is an important background process for resonances decaying via leptonic pairs and thermal emission of di-lepton pairs in heavy ion collision.

## 3.3 Dimuon Continuum

Invariant mass continuum of muon pairs is usually divided into three regions: (1) Low Mass Region (LMR) upto 1 GeV ($\sim m_\phi$), (2) Intermediate Mass Region (IMR) 1 - 3 GeV ($\sim m_\phi - m_{J/\psi}$) and (3) High Mass Region (HMR) above 3 GeV ($\sim m_{J/\psi}$). LMR region spectrum is dominated by the resonances of low mass vector mesons, IMR region is dominated by dimuon source of thermal production, and HMR is dominated by the different quarkonia resonances important for study of heavy flavor physics. IMR region is more difficult to study because it is not easy to disentangle two or more processes contributing to a continuum and because of its sensitivity to a correct combinatorial background subtraction. Apart from resonances from vector mesons, LMR region is mostly due to uncorrelated muon pairs coming from the semi-leptonic decays of open charm and Drell-Yan process. An important finding in SPS (Super Proton Synchrotron)-NA60 experiment at CERN is the large excess of low-mass di-leptons in Pb+Au collisions compared to expectations from proton-proton collisions [68] which is explained by medium modifications of the $\rho$ meson [69] but not so conclusive.

## 3.4 Combinatorial Background

While measuring signal dimuons there are certain level of events where we have combinatorial background contribution from uncorrelated muon pairs mostly coming from pion and kaon decays. Source of uncorrelated muon pairs are two different particles, contribute to both opposite-sign and like-sign pair samples. In analysis, such contribution is estimated through a super-event (SE) or mixed event technique. In SE technique single like-sign or unlike-sign muons are combined to from muon pairs of all charge combinations from different events. Like-sign technique gives the background contribution while unlike-sign gives total contribution of both signal as well background from which signal can be extracted, as done by NA60 experiment, by subtracting like sign background. Matching procedure of detector system may also introduce contribution to the background and hence, final dimuon continuum need to be corrected for such contributions.

## 3.5 Experimental Results

At CERN-SPS, NA60 experiment has measured di-muon spectrum with unprecedented precision at 158 AGeV In+In collision energy. A strong excess of muon pairs is observed in the mass region $0.2 < M < 2.6$ GeV. We will discuss the three regions of experimental di-muon continuum in the following subsections.

### 3.5.1 Low Mass Vector Mesons

The di-muon invariant mass distributions for In+In collisions at 158 AGeV measured by the NA60 collaboration [70, 71] is shown in figure 3.1. The black line in the figure represents mass spectra from the opposite-sign muon pairs while blue line represents the combinatorial background from like-sign muon pairs. After subtraction of the combinatorial background and of the fake matches (as shown by blue dashed-dotted line) the signal pairs (red line) of about 440,000 muon pairs roughly 50% of the total available statistics is

obtained. Fake match contribution is only 7% at the combinatorial background level. The combinatorial background is obtained from uncorrelated muon pairs from $\pi$ and K decays using a mixed-event technique. Two single muons from different like-sign dimuon triggers are combined while keeping accurate account for details of the acceptance and trigger conditions. Like-sign distributions generated from mixed events and the measured like-sign distributions agrees remarkably. The average charged-particle multiplicity density measured by the vertex tracker is 120 and the 1/7 is the average signal-to-background ratio. Signal pairs are shown in fig. 3.2 (red dotted line) together with a cocktail. We observe unknown excess in case of central collisons which is not present for peripheral case. After subtracting the resonances like phi, omega, eta and corresponding Dalitz decays, we obtain an unknown "excess yield" containing the rho meson contribution (line with black triangles).

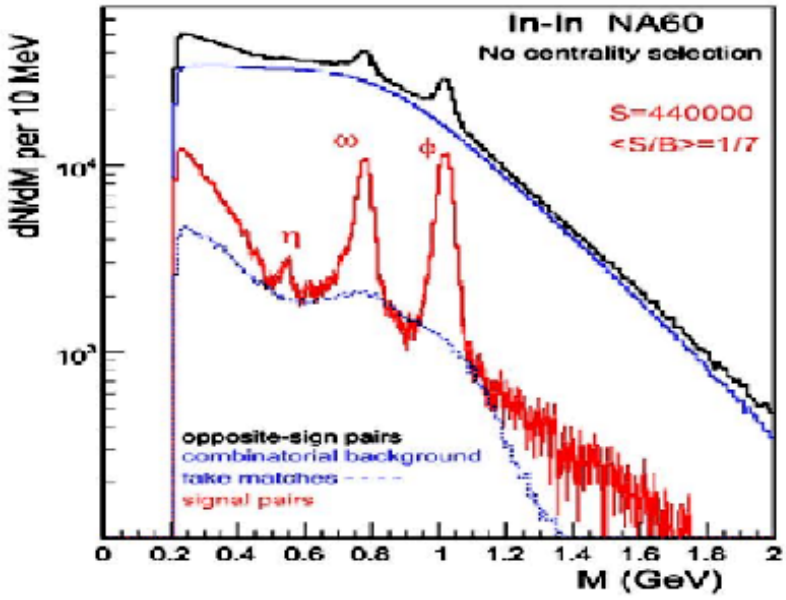


Figure 3.1: NA60 dimuon invariant mass distributions measured in In+In collisions at 158 A GeV. Mass spectra of the opposite-sign dimuons (upper black), combinatorial background (blue line), signal pairs (red line), and fake matches (blue dotted)

The excess mass spectra for 4 multiplicity bins, resulting from subtraction of the hadron decay cocktail from the measured data, are shown in Fig 3.3.

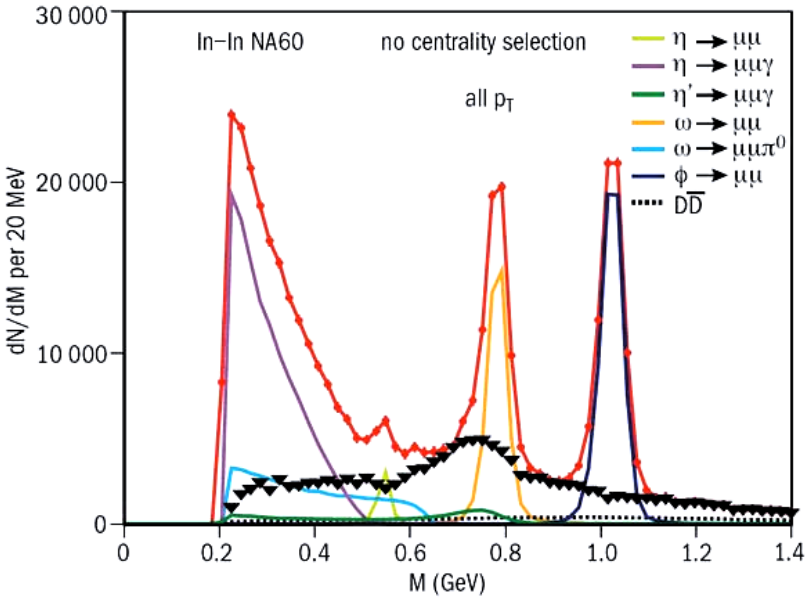


Figure 3.2: Signal pairs (red dots), excess yield (black triangles, see text)

From the plot, a peaked structure is seen in all cases which is broadening strongly with centrality but remains essentially centered around $\rho$. At the same time, the total yield increases relative to the cocktail, $\rho$ increases most in the most central case. In simple terms, $\rho$ primarily shows broadening without any noticeable shift in mass in In-In collisions.

Fig. 3.4 depicts the acceptance corrected excess yield (black dots with error bars). Moreover, a cocktail of various contributions to the access yield is shown as calculated with an expanding fireball models which also include a phase transition [72]. According to these model calculations, the low-mass range is dominated by the broadened of in-medium rho meson (red dashed-dotted line), the radiations from the QGP (orange dotted line), and by the freeze-out rho (black solid line). It is argued that the melting of the rho resonance is compatible with chiral symmetry restoration and suggesting a gradual change in the effective degrees of freedom in the system created in heavy ion collisions. Coupling of the vector mesons to the baryons explains the data in the low mass range. In the intermediate mass range the major contributions are QGP radiations, multi-hadron annihilation (blue dashed

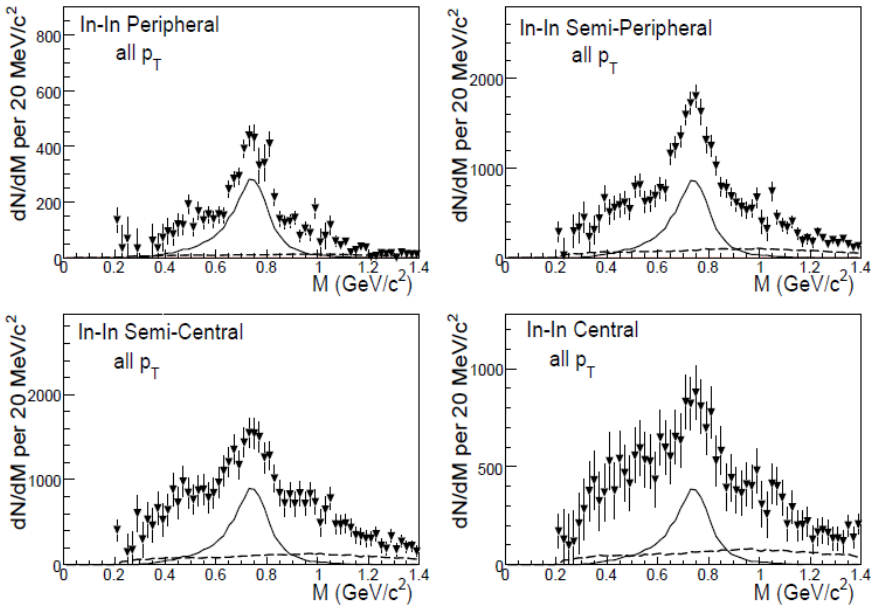


Figure 3.3: Excess mass spectra of dimuons. The cocktail $\rho$ (solid) and the level of uncorrelated charm decays (dashed) are shown for comparison.

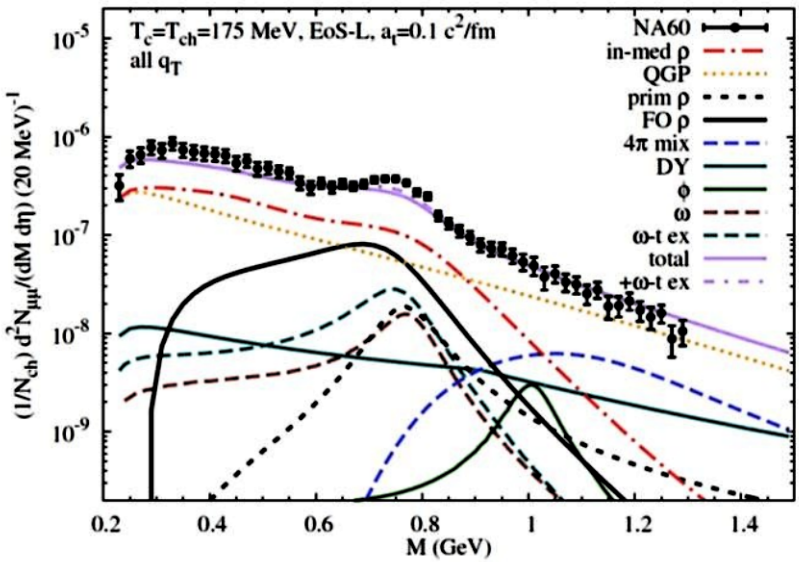


Figure 3.4: Acceptance corrected dimuon excess spectra measured in In+In collisions at 158 A GeV by NA60 compared to theoretical calculations with in-medium vector spectral functions

line), and quark-antiquark annihilation like Drell-Yan (solid turquois line). These calculations have assumed a lattice EoS and a critical temperature coinciding with the chemical freeze-out temperature ∼175 MeV, and 245 MeV as initial temperature reflected in the slope of the spectra.

### 3.5.2 Thermal Radiation

The dominant contribution to the intermediate mass region of the dimuon excess spectrum shown in figure 3.4 has been predicted to be from QGP thermal radiations (by R. Rapp et al [134]). Information about the QGP temperature can be extracted from the slope of the invariant mass spectrum and transverse momentum spectra of dimuons with different masses as shown in Fig. 3.5 where open charm contribution has been subtracted throughout. The normalization of the measured region is independent of the rapidity in absolute terms.

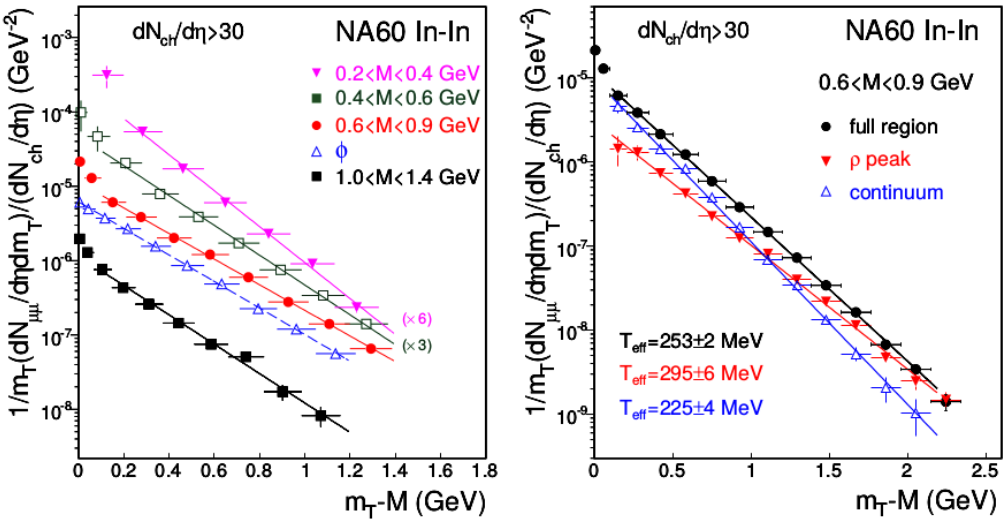


Figure 3.5: (Left) Transverse mass spectra of the excess dimuons for different mass windows and the $\phi$. (Right) A decomposition into peak and continuum for the $\rho$-like window

Effective temperature $T_{eff}$, which is an inverse slope parameter of the exponential fits to the $m_T$ spectra, is plotted for combined LMR and IMR regions of the dimuon excess yield with Drell-Yan contribution subtracted

as shown in Fig. 3.6a [73]. In the low-mass range, the effective temperature increases with invariant mass as observed for the hadrons which is attributed to the increase of collective flow in the late phase of the heavy ion collision. In the intermediate mass range, the effective temperature drops suggesting emission from early(partonic) phase of the dimuons in the heavy ion collision where the collective flow is not yet developed. Hadrons with masses upto charmonium shows very similar pattern of the effective temperature as shown in Fig. 3.6b [74]. Temperatures extracted from the invariant mass spectrum of the dimuon excess yield and from the transverse momentum spectra exceed the critical temperature ($T_c \sim 170MeV$) providing evidence for radiation from the QCD partonic region formed in heavy ion collisions.

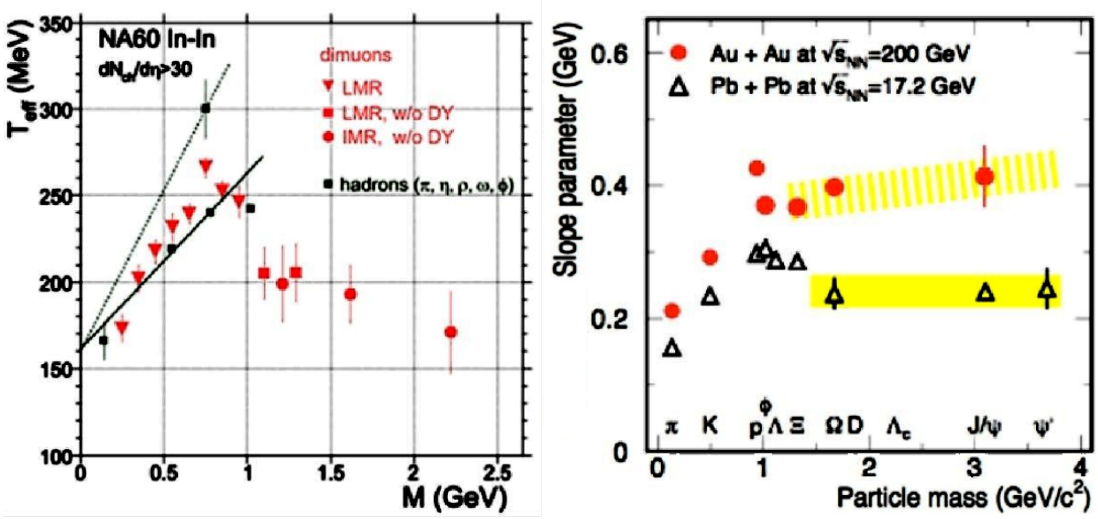


(a) (b)

Figure 3.6: (a) Inverse slope parameter $T_{eff}$ versus dimuon mass M for the low and intermediate mass range measured in In+In collisions at 158 A GeV.(b) Inverse slope parameter versus particle mass for hadrons measured in Pb+Pb collisions at 158 A GeV and for Au+Au collisions at $\sqrt{s_{NN}} = 200$ GeV.

In summary, The low mass dimuon spectrum is consistent with a dominant contribution from $\pi^+\pi^- \longrightarrow \rho$ with $\rho$ decaying via di-muonic channel and $\rho$ spectral function shows a strong broadening without shift in its mass. The excess is found to be prompt, not due to enhanced charm production, with pronounced differences to Drell-Yan pairs for intermediate and high mass region. The slope parameter $T_{eff}$ extracted from transverse momen-

tum spectra rises with mass up to the $\rho$ then follows a sudden decline. Initial rise in $T_{eff}$ is consistent with radial flow of a hadronic emission source and decline in $T_{eff}$ hints about the absence of flow which is related to parton-hadron duality, suggesting a dominant partonic emission source in the region.

### 3.5.3 Charmonium

Heavy flavor quarks are produced predominantly in hard scatterings during the initial stage of the collision. They are unique probes to study the initial conditions and the properties of the quark gluon plasma formation in heavy ion collisions. In heavy ion collision as initial state is of highest temperature/density where phase transition to deconfined phase is expected, dissociation of D-mesons and charmonium are expected resulting in their suppressed production. Matsui and Satz predicted the charmonium suppression due its dissociation by color screening effect in a deconfined medium. Experiments at NA50 and NA60 collaborations investigated charmonium suppression in Pb+Pb and In+In at 158 AGeV collision energy and plotted the ratio of the measured $J/\psi$ yield over the expected yield as function of participating nucleons $N_{part}$ shown in Fig. 3.7 [75]. Proton-nuleus(p+A) central collions were used to calculate expected yield of the $J/\psi$ production cross section at the same beam energy. For both In+In and Pb+Pb collisions, data shows no deviation from expectation up to about 200 $N_{part}$, whereas for central Pb+Pb collisions an anomalous $J/\psi$ suppression of the order of 20-30% is seen.

Measurements of charmonium at future experiments at FAIR energies ($E_{Lab}$ =2-45 AGeV) are challenging due to the very low charm production cross section. Figure 3.8 depicts a total charm production compilation from experimental results as a function of particle energy, together with a NLO-pQCD calculation and its uncertainty [76]. There is no data available at FAIR energies ($\sqrt{s_{NN}} < 8$ GeV). FAIR intend to provide new precision data on charm production which will be important for the clarification of the charm production mechanism close to its threshold.

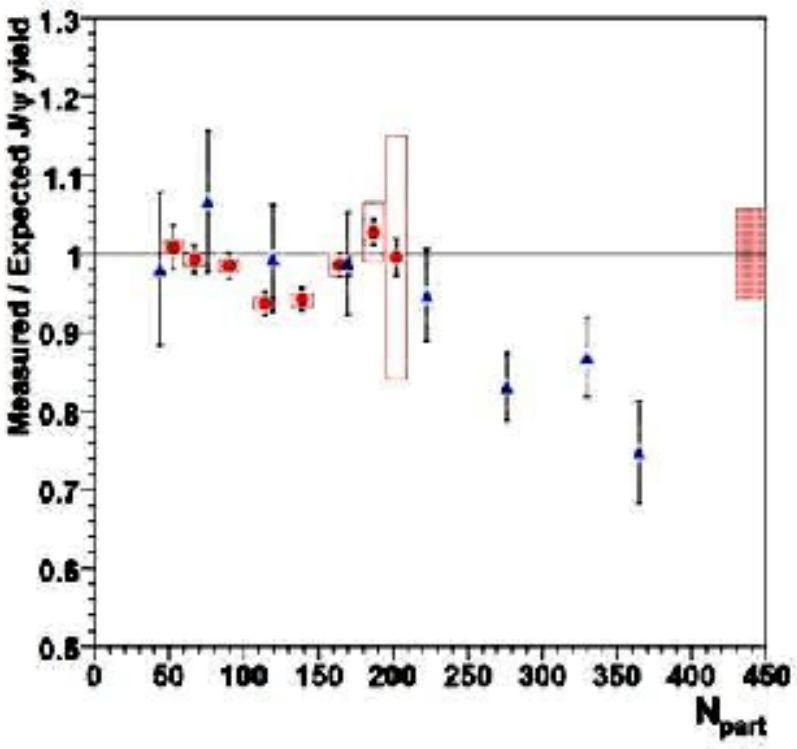


Figure 3.7: $J/\psi$ suppression pattern in In+In collisions (red circles) and Pb+Pb collisions (blue triangles) at 158 A GeV

## 3.6 Summary

The comparison of experimental data with theoretical models have demonstrated that dimuon spectrum provide important information on the evolution and on the properties of the hot and dense fireball created in heavy ion collisions. In-medium mass distribution of short-lived vector mesons is modified both due to their coupling to baryon resonances and by their interaction with the chiral condensate. When measured dilepton mass distribution is subtracted with the contribution from vector mesons, allows to extract the thermal radiation, and, hence, the temperature evolution of the fireball. We observed that at top SPS energies, the di-muon mass distribution in the intermediate mass range is dominated by radiation from a deconfined partonic phase. The comparison of charmonium yields measured in nucleus-nucleus

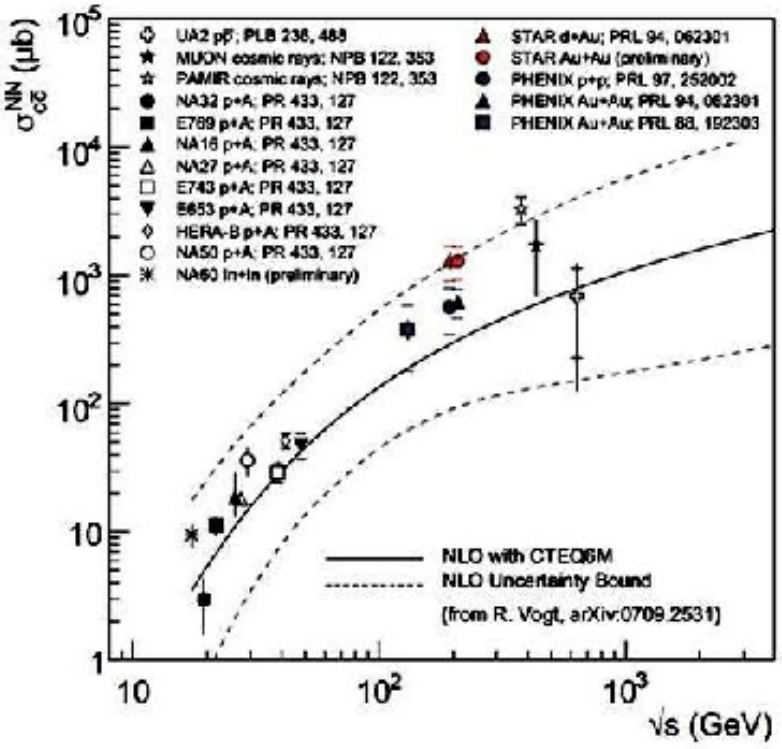


Figure 3.8: Compilation of total charm production cross-section measurements compared to pQCD NLO calculations (solid line). The dashed lines represent the uncertainty bands of the calculations

with proton-nucleus collisions has showed an anomalous suppression of charmonium yeild in central collisions of heavy nuclei which was explained by considering dissociation of charmonium due to color screening in the quark-gluon phase. This conclusive observation is one of the most convincing experimental facts hinting towards the existence of quark gluon plasma phase formation at top SPS energies. Mainly, the dilepton measurements have been performed at 158 AGeV by SPS at CERN, except one spectrum that has been taken at 40 AGeV in Pb+ Au collisions by CERES collaboration where even an increased excess in the yields has been seen [68]. To search for the onset of in-medium mass modifications of vector mesons or for partonic contributions, a systematic beam energy scan of the dilepton yields has not been performed yet.

CBM is set to scan the beam energy range from 2 to 40 AGeV where

matter at the highest net-baryon densities are expected to be created in the laboratory, where no dilepton measurement has been done so far in heavy ion collisions, and which will, certainly, open a new era in dilepton experiments. Plan at CBM experiment is to measure systematically both di-electrons, using RICH detector, and di-muons, using MuCh detector in place of RICH in the set-up, for p+p, p+A and A+A collisions as a function of incident beam energy and system size. High precision data of two leptonic channels of low mass vector mesons and charmonium will complement each other to provide a consistent picture on di-leptonic radiation from dense baryonic matter. Therefore, one can say that the CBM experiment has a large discovery potential.

# Chapter 4

# DIMUON DETECTION SYSTEM FOR CBM

One of the major challenges of muon measurements in heavy- ion collision experiments is the muon identification over a wide range of momenta so as to cover all three regions of the dimuon invariant mass namely: (1) low mass vector mesons region, (2) intermediate mass region, and (3) high mass charmonium and bottomonia region. At FAIR (Facility for Antiproton and Ion Research), one of the goal is to measure the dimuon spectra over a broad region of invariant mass in heavy ion collision in beam energies from 2 to 45 A GeV where matter at highest baryonic density is expected to be created. The modifications of vector meson spectral functions in low mass region ($< M_\phi \approx 1\ GeV/c^2$ ) due to in-medium modifications during dense medium formation created in heavy ion collisions, will be signature imprint of chiral phase transition. Intermediate mass region ($M_\phi - M_{J/\psi}$) could be used to extract the thermal radiation from the dense and hot fireball. High mass region around 3 GeV/c$^2$ ($\approx M_{J/\psi}$) could be used to get the signature for deconfinement by charmonium dissociation [77, 27, 70, 71, 72, 75]. Muon detection system usually consists of a thick hadron absorber to absorbe hadrons, photons and electrons, but due to its thickness it also stops the low momentum muons and hence capable of detecting only mainly high momentum muons. Experiments like PHENIX [78], ALICE [79], CMS [80] etc. use

a muon detection system using conventional technique which effectively puts a cutoff on the reconstructed muon momentum. These muon detection systems can be placed at forward rapidities where the muons are boosted to higher momenta perticularly in fixed target experiments. Problem at lower energies like FAIR range and low mass vector mesons is that the low momentum muons are highly likely to get absorbed in the thick absorber and only high momentum muons could be detected. For the detection of all kinds of muons, wether soft or hard, we propose a novel muon detection setup design for the Compressed Baryonic Matter (CBM) experiment [81] at the upcoming facility of FAIR at Darmstadt, Germany. Proposed set-up is called muon chambers (MUCH) [82] and idea is to divide the total absorber into thinner segments along the beam direction with tracking chamber triplets placed in between the absorber segments. By doing this we are able to identify muon candidates over a wide range of momenta depending on the number of absorber segments that the particles have passed through and hence improves the detection efficiency of the low momentum muons. MUCH will be placed upstream the Silicon Tracking System (STS) [83] which is inside the gap of a large acceptance dipole magnet. In this chapter, we will present the studies related to the detector R&D with optimized parameters like the number, thickness and materials of the absorber segments, and the number and granularity of the tracking detectors and in next chapter feasibilty studies at 25 AGeV central Au + Au collisions will be given by using UrQMD event generator [84].

PLUTO Monte Carlo generator [85] is used to model the phase space distribution of di-muon signals. Simulated particles have been transported using GEANT3 [86] transport code. In order to determine the efficiency and signal to background ratio in dimuon measurements over a wide range of invariant mass i.e., from low mass vector mesons to charmonia, full reconstruction has been performed.

This chapter is organized as follows: Sections 4.1, 4.2 and 4.3 discusses the concept of the muon system, processes and cuts used in simulation and the simulation procedure respectively. Section-4.4 gives account on the progress in beam-pipe and beam-pipe shielding for MUCH. We discuss the results of

performance studies in next chapter (5) followed by discussions in the end.

## 4.1 Muon Chamber (MUCH)

In order to build a segmented absorber system for muon detection system of CBM, careful analysis of different materials and their thickness, gap in between absorbers and tracking detectors is required. Required thickness of the hadron absorber segments of MUCH detector at FAIR energies can be estimated from Fig. 4.1 where the absorptions of various particles are shown as a function of thickness of an iron absorber. In this simulation, pions, protons, $\omega$ and $J/\psi$ have been transported individually through iron, which is commonly used as a hadron absorber. The study with individual particle species helps to understand the basic responses of these particles in the detector setup. For this estimation, to start with, iron has been taken as the absorber material like other existing muon experiments. Iron has considerably small interaction length $\lambda_I$ making it a good hadron absorber and fairly large radiation length $X_0$ which reduces multiple scattering.

For all species, equal number of particles have been taken as input. While pions and protons were produced by the UrQMD event generator at $E_{lab}$ = 25 A GeV, $\omega$ and $J/\psi$ have been generated by PLUTO event generator. It should be mentioned that the Pluto generator produces particles from a thermalized source with given slope parameter representing the temperature and rapidity width. The produced particles are decayed intrinsically by the event generator itself. As seen in Fig. 1, the higher momentum muons from $J/\psi$ decays are less strongly absorbed than the softer ones from $\omega$ decays. Moreover, it can be seen that beyond an iron thickness of 1.5 m, slopes of the reduction of intensity of pions and protons are similar to that of the muons from $\omega$ which means that the signal-to-background ratio (S/B) will not improve further by inclusion of additional absorber. In conclusion, for efficient and low back-ground detection of low mass vector mesons the total thickness of the iron absorber could be kept at about 1.5 m, whereas for the measurement of muons from $J/\psi$ decays, the background can be further reduced by adding an additional iron absorber of about 1 m thickness.

Apart from the total absorber thickness, in a segmented absorber system, the thicknesses of the individual absorbers also need to be fixed.

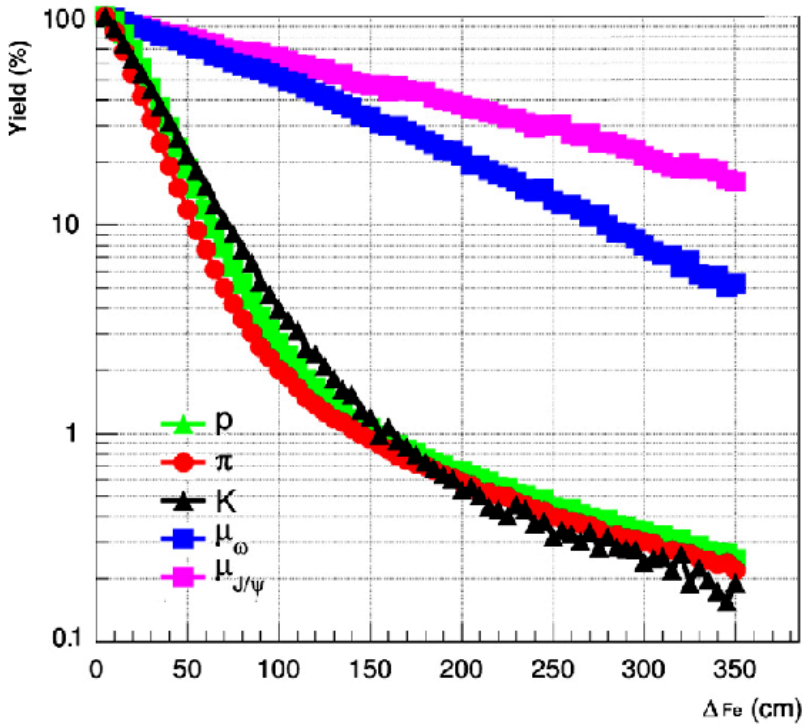


Figure 4.1: Fraction of different types of surviving particles as a function of the transverse length in iron. The simulation has been performed for Au + Au collisions at a beam energy of 25 AGeV using the UrQMD event generator and the GEANT3 transport code. The vector mesons have been generated with the PLUTO event generator.

### 4.1.1 First Absorber

Particle multiplicity in front of first absorber will be large, so one need to optimise it in terms of its material and thickness. Its the first absorber who will decide the occupancy of the first detector station and hence its required rate capability. In the following, discussion on the selection of first absorber is given in more detail.

Even though simulation has been done with iron as the only absorber material initially, subsequently, for the first absorber, decision to use 60 cm carbon instead of 20 cm iron has been made on the reasons which are outlined

below. The thickness and material composition of the first absorber segment are of particular importance as one has to find a compromise between hadron absorption and multiple scattering, the effects of which play most important roles in the first absorber. The hit rate on the detectors after the first absorber should be within the limit that the tracking chambers will be able to operate efficiently. On the other hand, due to enhanced multiple scattering, the tracks might be deflected in the thick absorber resulting in mismatch of the MUCH track segments with the STS track segments. This finally leads to an increase of the reconstructed background. In our simulation, the selection of material and thickness of the first absorber segment is performed by two parameters:

1. The multiplicity of secondaries at the end of the first absorber that produces hit on the tracking detectors. The hit density decides the technology of the chambers in the first (most upstream) set of chambers that face harshest radiation environment.

2. The performance of tracking in two setups for selection of muon candidates. In the reconstruction procedure, the STS track segments are propagated through the MUCH hits starting with the hits from the most upsteam chamber, and therefore any MUCH hits unrelated to STS tracks would add to the number of possible background combinations. Finally, muons are selected by using different cuts on track parameters as discussed in next chapter.

In Fig. 4.2, the variation of particle multiplicity as a function of absorber thickness for central Au + Au collisions at 25 AGeV beam energy has been shown. Simulations have been performed for two types of materials for the first absorber, i.e., iron Fig. (4.2a) and carbon Fig. (4.2b). The simulation indicates that for both the absorber materials the particle multiplicity is dominated by the yield of secondary electrons that rises initially and then drops with increasing material thickness. The vertical dotted lines show the proposed thicknesses of the first absorbers for two types of materials of similar interaction lengths. The density of secondary particles at those thicknesses is within the detectable limit of tracking chambers. Another important feature

seen in Fig. 4.2 is that for iron, the absorption is stronger as compared to carbon favoring the selection of iron as subsequent absorber materials.

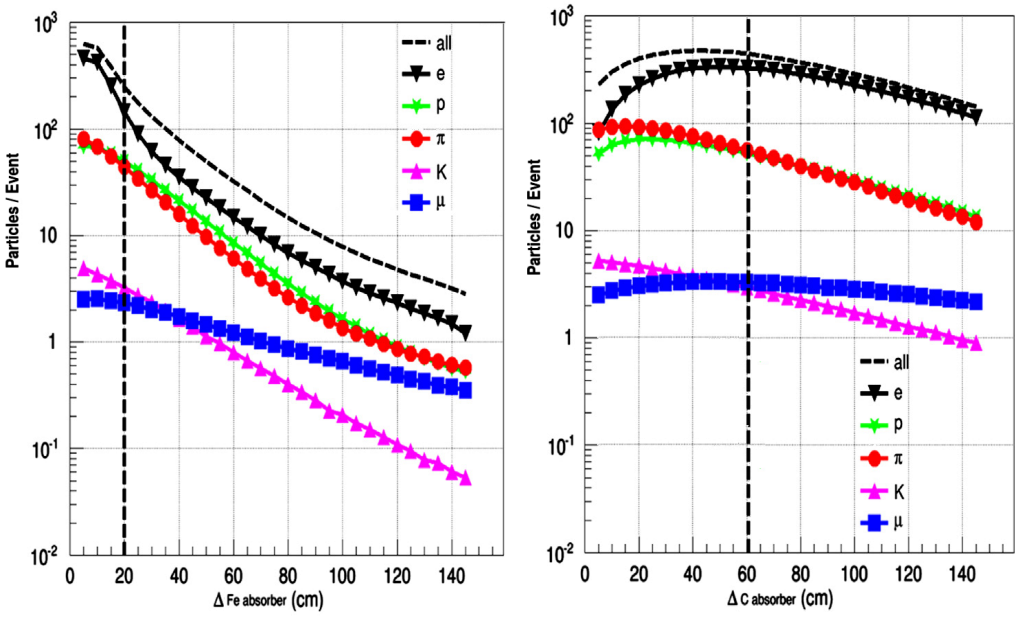


(a) Iron Absorber (b) Carbon Absorber

Figure 4.2: Variation of particle multiplicity per central Au+Au collision at 25 AGeV as a function of the thickness of (a) Fe (b) C

After an initial estimate based on single particle simulation, the final selection of the first absorber has been performed based on the simulation of background for fully reconstructed events. The results are illustrated in Fig. 4.3 where the ratio of the number of reconstructed tracks to that of the accepted input Monte-Carlo tracks is shown as a function of the thickness of the first absorber. Selected tracks have combinations of 4 STS hits and 2 MUCH hits. These selected tracks also include wrong combinations such that the STS hits are from a particle which is absorbed and MUCH hits are from secondary particles like electrons produced in the absorber. In such a case, the number of reconstructed tracks is one, but the valid number of Monte Carlo tracks to detect by MUCH is zero. This mismatch probability increases with increasing thickness to be reflected by the ratio of the reconstructed to Monte Carlo tracks.

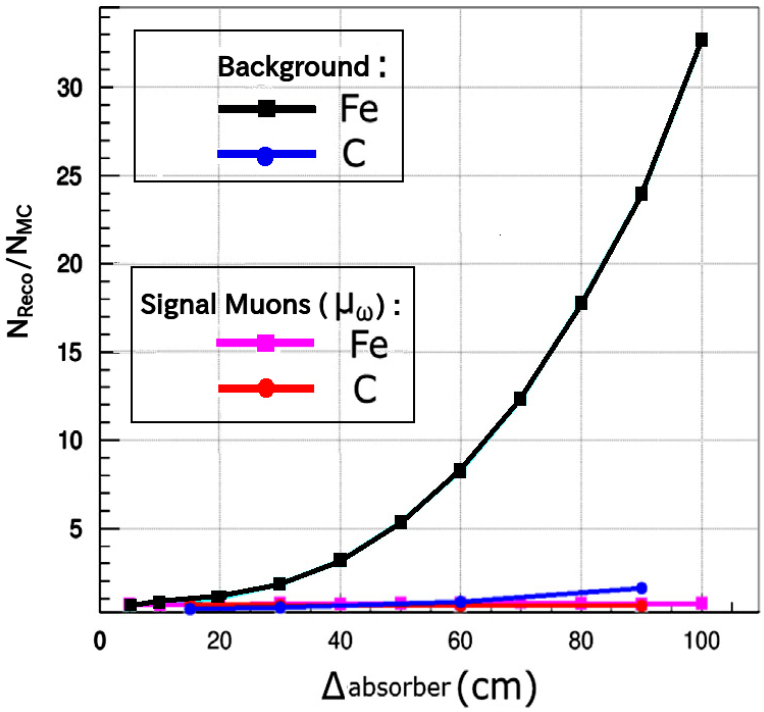


Figure 4.3: Ratio of the number of reconstructed tracks to the number of accepted Monte Carlo (MC) tracks (for definition, see text) as a function of the thickness of the first absorber. The simulation was performed for central Au+Au collisions at 25 AGeV with iron and carbon as absorber materials.

From Fig. 4.3, two cases i.e., 60 cm carbon and 20 cm iron as the first absorber have been compared. A detailed look at the ratio being discussed here shows that carbon is likely to preferable as the first absorber and for a thicker iron absorber, the probability of secondary tracks increases sharply. The properties of $\chi^2$ MUCH , the $\chi^2$/dof for the track segments taking only the MUCH points in fitting, an important track parameter for selection of muons in two setups, i.e., first absorber with carbon and with iron have also been studied. Fig. 4.4 shows the distribution of $\chi^2$ MUCH for signal muons from $\rho^0$ and backgrounds for two different setups. For muons from other LMVM, performance is similar. It is seen clearly that the background is about an order of magnitude lower for the setup using carbon as the first absorber for two cases of similar signal strengths. This basic property could be used to have a smaller background in case of carbon-based setup.

In addition to the consideration of smaller number of secondary tracks,

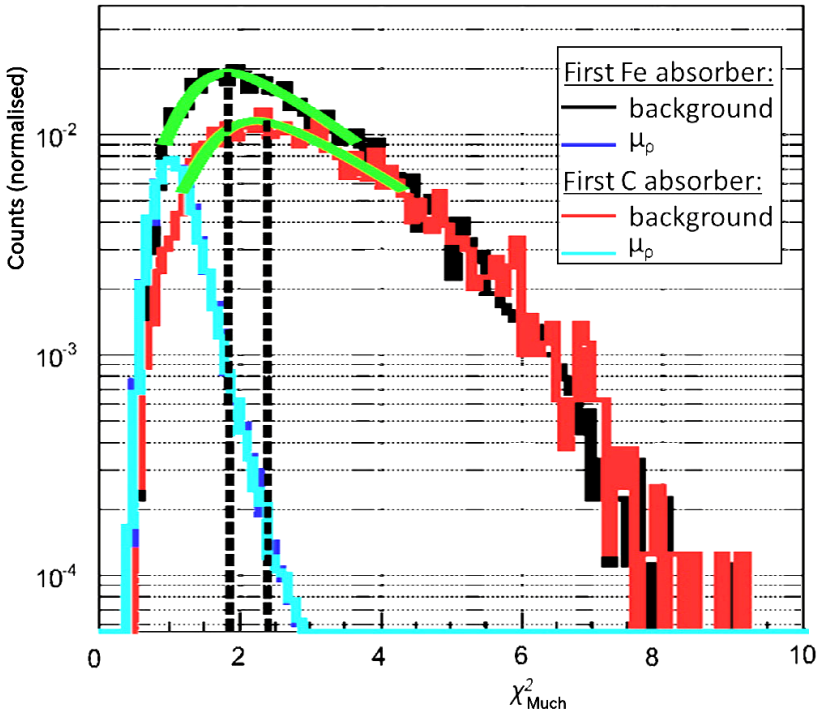


Figure 4.4: $\chi^2_{MUCH}$ of the tracks from signal muons and backgrounds for two absorber setups. It is seen that for the setup using carbon in the first absorber shows better signal to background discrimination power using $\chi^2_{MUCH}$ based cuts.

carbon as the first absorber material has the added advantage over iron is that it is more suitable to place carbon inside a magnetic field. For the subsequent simulation, 60 cm carbon has been chosen as the first absorber material. The absorbers are made of iron in order to have a compact absorber which reduces the background of muons from weak decays of pions and kaons. Moreover, it is illustrated in Fig. 4.2 that the absorption of hadrons as a function of absorber thickness is much stronger for iron than for carbon, where the absorption of muons are similar for two cases.

### 4.1.2 MUCH Layout

The final layout of the MUCH detector system is shown in Fig. 4.5. The muon system is followed by a Time of flight (TOF) system for additional reduction of background (not shown in figure). MUCH setup as shown in

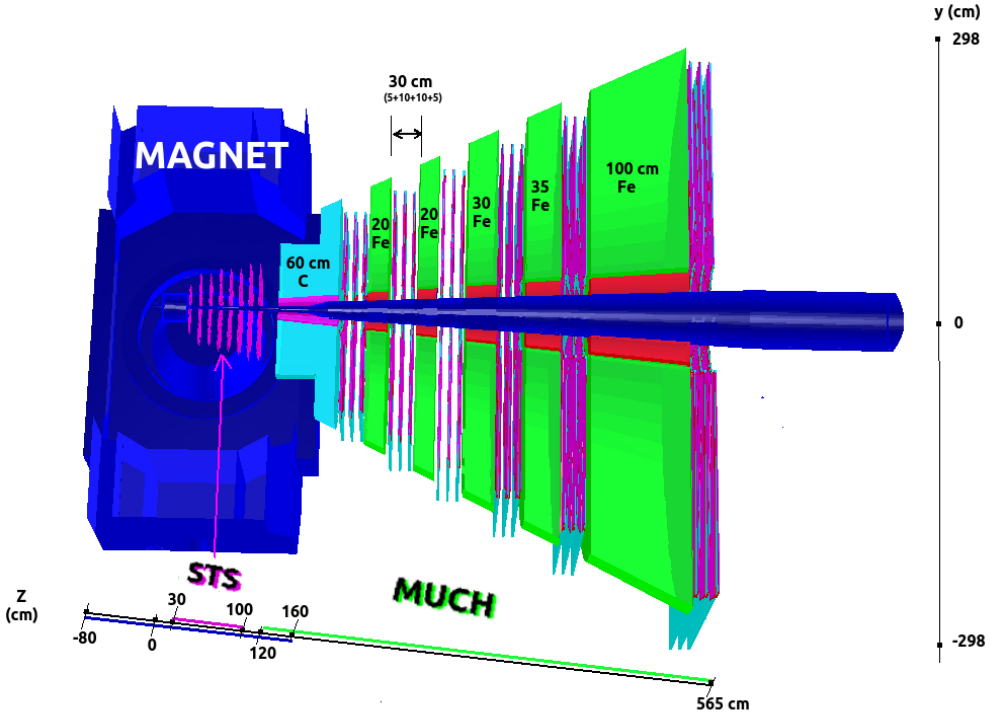


Figure 4.5: A schematic view of MUCH layout. It is located at a distance of 120 cm downstream the target. A part of the first MUCH absorber (40 cm carbon) is placed inside the magnet. It consists of 18 detector layers and 6 absorbers with total absorber thickness of 265 cm. The last 3 layers are used for charmonium trigger and hence the effective number of layers for the measurement of low mass vector mesons is 15. The TOF wall is not shown in the setup

Fig. 4.5 comprises of 6 absorbers, first one made of 60 cm carbon and the rest made of iron of varying thickness and with 6 tracking stations sandwiched between absorber layers. The total absorber length in the current design amounts to 265 cm divided into 60 cm carbon and (20 + 20 + 30 + 35 + 100) cm of iron which is equivalent to 13.5 times the hadronic interaction length ($\lambda_I$).

The angular acceptance of the detector spans from $5.7^o$ to $25^o$ excluding the detector dead area. In the following, we define the nomenclatures used in the discussions.

- **Station :** A station is the combination of tracking detectors sandwiched between two absorber segments. Much Layout in Fig. 4.5 consists of 6 stations.

- **Layer :** Each station consists of three planes of tracking detectors.

Each plane is called a detector layer. Much Layout in Fig. 4.5 consists of $6 \times 3 = 18$ layers.

- **Modules :** Each layer consists of a varying number of detector modules on two sides of an aluminium support plane.

Each tracking station consists of triplet of detector layers resulting in the number of layers to be 18. The gap between two successive absorbers is set to be 30 cm. This geometry is designed to be used both for the identification of charmonium and low mass vector mesons. As discussed earlier, low momentum muons from LMVM are identified by taking hits up to the $15^{th}$ layer, i.e the maximum number of detector hits for low mass vector meson measurement is 15 and the corresponding total hadron absorber thickness is 60 cm of carbon and 1.05 m of iron. All stations including the 100 cm thick absorber downstream is used for the identification of muons from the charmonium decay.

### 4.1.3 Tracking Detectors

Sector-shaped gaseous chambers has been used as sensitive detectors. The gaseous detectors are one of the promising candidates for this type of systems where a large detector area is to be covered and the detector is required to handle very high hit density at high rate. It has been found that Micromegas [88] and GEM [87] are the possible candidates that suit the **high rate capability** especially for the first few tracking chambers of MUCH. Considering the further advantage of GEM like isolation of readout from the multiplication region, thereby reducing the spark probability. For the advantages mentioned above, GEM has been chosen as the baseline technology option for the tracking chambers. Present simulation therefore assumes GEM as the tracking detector and a fast simulation for signal generation has been implemented in this work as discussed later. Argon gas used as active medium has thickness of 3 mm. Cables, gas tubes, PCBs and front-end-electronics are not included in the present version of simulation. The distance between the chamber centers is 10 cm to provide enough space for accommodating the

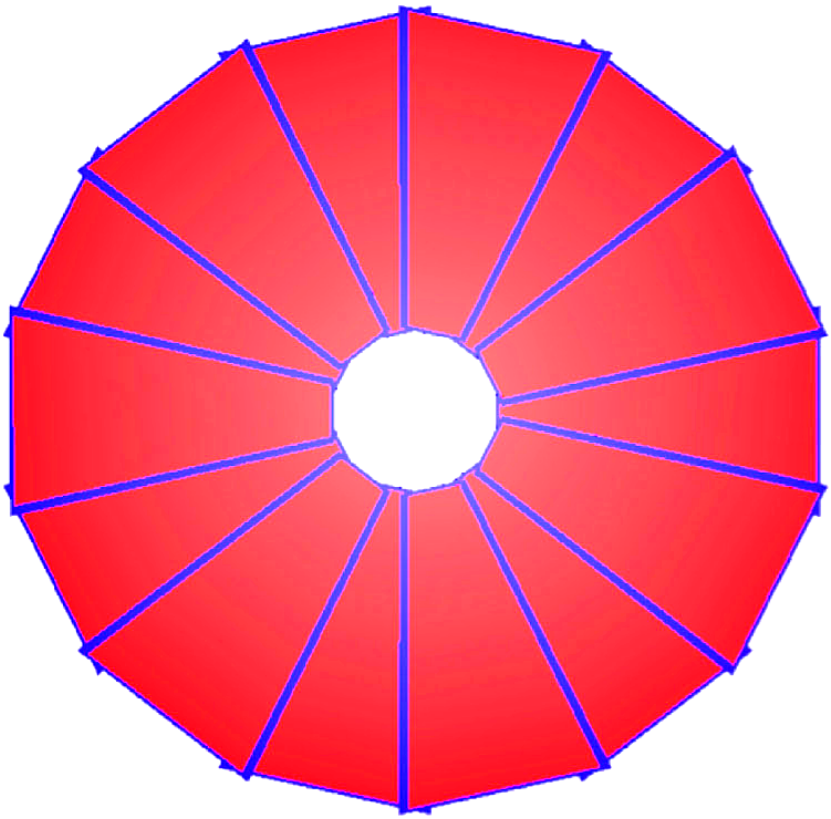

Figure 4.6: The arrangement of sector-shaped chambers on a layer of the first MUCH station is shown. Alternate sectors are placed in opposite sides (front and back with respect to the beam direction) of the layer. The notches at the corner show the overlap regions between the modules

detector profile that includes electronics boards, mechanics, cooling arrangement among others. An overlap between the sector-shaped modules that are placed on two sides of the support structure has been kept to 2 cm along the radial direction to avoid possible dead zones. A detector layer of the first station with 14 sectors as implemented in the simulation is shown in Fig. 4.6. The number of sectors in a particular detector plane depends on the radii of the station.

### 4.1.4 Beam Conditions

CBM experiment which aims to detect rare probes like charmonia, reaction rates of up to 10 MHz are required which is two order of magnitudes higher

compared to the requirement for low mass vector mesons in dimuon channel. Assuming a 1% interaction target, this requirement results in a beam intensity of $10^9$ ions/sec (for Au beams). At CBM, the beam conditions are proposed to have following features:

- **Extraction:** Low extraction, duty cycle better than 50%.
- **Emittance:** 3.0 mm mrad
- **Halo:** Below $10^{-5}$ of the total beam intensity at a distance greater than 5 mm
- **Spill structure:** Intensity fluctuations below a factor of 3 down to tens of nano-second time scale.

## 4.2 Simulation Tools

The simulation has been performed using the UrQMD event generator for input and GEANT3 for particle transport. All the physics processes which affect the production of hits on muon chambers have been switched on in GEANT3. Important GEANT3 processes which are included in our simulation are listed below:

- *Pair production with generation of* $e^-,\ e^+$
- *Compton scattering with generation of* $e^-$
- *Photo electric effect with generation of electron*
- *No photofission*
- *Delta-rays with generation of* $e^-$
- *Positron annihilation with generation of photons*
- *Bremsstrahlung with generation of gamma*($\gamma$)
- *Hadronic process with generation of secondaries*

- *Muon nuclear interaction with generation of secondaries*
- *Decay inflight with generation of secondaries*
- *Contineous energy loss with generation of delta-ray above DELTA_CUT & restricted landau fluctuation below DELTA_CUT*
- *Multiple scattering according to Moliere Theory*

**1 MeV** cut is used in different processes involving different particles like:

- *gammas ($\gamma$)*
- *electrons ($e$)*
- *neutral hadrons*
- *charged hadrons*
- *muons ($\mu$)*
- *electron bremsstrahlung*
- *muon and hadron bremsstrahlung*
- *delta-rays by electrons ($\delta_e$)*
- *delta-rays by muons ($\delta_\mu$)*
- *direct pair production by muons*

And time of flight (ToF) cut is **1 sec**.

It can be seen that cut is significantly below the average momentum of the particles of interest (e.g. muons, pions). The tracks are then reconstructed from the hits of STS and MUCH.

## 4.3 Simulation Procedure

The entire simulation procedure can be divided into following steps:

1. *Geometry implementation and transport*
2. *Segmentation and digitization*
3. *Hit formation*
4. *Track propagation in tracking chambers, and*
5. *Selection of tracks as muon candidates*

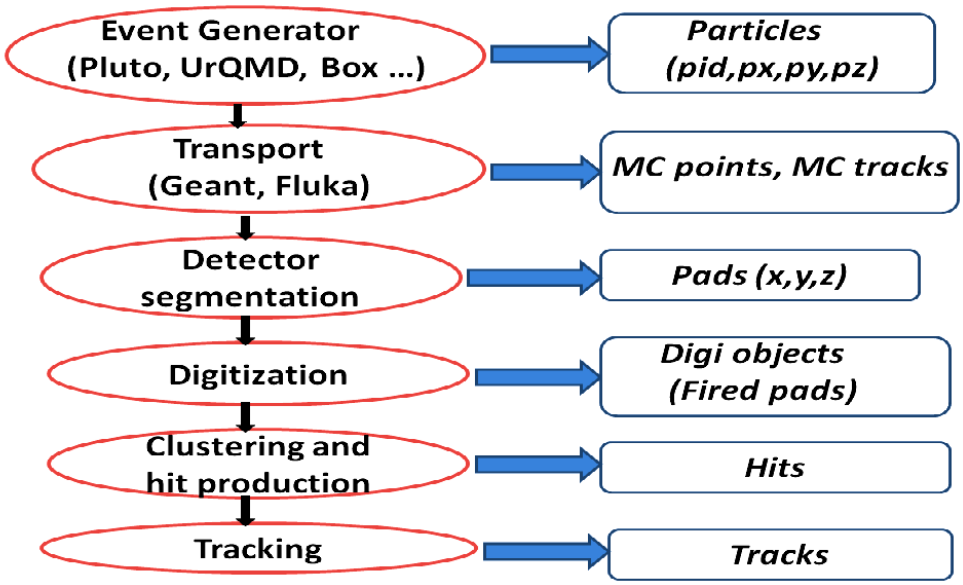


Figure 4.7: Schematic layout of the simulation chain for CBM muon detection system.

This is shown in figure 4.7. Event generators give particle information interms of four-momentum, particle-id etc in an ascii/root file format. This information is taken by the GEANT3 to transport the particle via the detector set-up implemented using the latest geometry. Output of the transported information is stored interms of MC (monte-carlo) points and MC tracks which form the simulated input for our detector. Next detector response is implemented first by implementing detector segementation and then digitization.

Output of the digitization is stored interms of digi objects/fired pads which contain the information about the smallest detector element called pads if fired (hit by the particles). Then clustering algorithems are used to group or subgroup the digis which are called hits. Hits are used to reconstruct the tracks. The final identification of muon tracks is a part of the dimuon analysis. Detailed discussion of the simulation chain will follow in subsequent sections.

### 4.3.1 Geometry implementation and transport

The incident particles from the event generator are transported through STS and MUCH geometries. The implementation of geometry therefore involves the implementation of conical absorbers of varying sizes placed around the conical beam pipe. Conical absorbers are used to accept the forward focused particles. The detector modules are of trapezoidal profiles that are placed behind each absorber block. Three layers of detector planes are positioned in between two absorbers. Each tracking layer consists of a thin support structure and an equal number of sector-shaped modules are placed on two faces of th aluminium support structure. For reducing the dead-space, modules on two faces are placed in such a way that a border of the module on one side has overlap with an active zone of the module on the opposite side. The number of stations, their shape, size and number of modules are varied for optimization of efficiency and signal to background ratio (S/B) for detecting both low mass vector mesons and charmonia. Muon detector geometry information is provided using an ASCII input file which containing different parameters as shown in Fig. 4.8. The file contains the information like the start position of detector, positions of numbers of absorbers and detector layers, distance between the layers, type of tracking detector to be used and so on..

Information contained in the input file is implemented using GEANT3. Then GEANT3 uses the geometry to transport the input particles and secondaries created during the transport.

Geometrical acceptance of muon chamber goes from $5.7^o$ to $25^o$ whereas

```
# General information
MuchCave Zin position [cm]  :     120
Acceptance tangent min      :     0.1
Acceptance tangent max      :     0.5
Number of absorbers         :       6
Number of stations          :       6

# Absorber specification
Absorber Zin position [cm]  :       0      50      100     150     210     275
Absorber thickness [cm]     :      20      20       20      30      35     100
Absorber material           :       I       I        I       I       I       I

# Station specification
Station Zceneter [cm]       :      35      85      135     195     260     390
Number of layers            :       3       3        3       3       3       3
Detector type               :       3       3        3       3       3       3
Distance between layers [cm]:      10      10       10      10      10      10
Support thickness [cm]      :     1.5     1.5      1.5     1.5     1.5     1.5
Use module design (0/1)     :       1       1        1       1       1       1

# GEM module specification (type 1)
Active volume lx [cm]       :    25.6
Active volume ly [cm]       :    25.6
Active volume lz [cm]       :     0.4
Spacer lx [cm]              :     0.5
Spacer ly [cm]              :       5
Overlap along y axis [cm]   :       2

# Straw module specification (type 2)
Straw thickness [cm]        :     0.4

# Sector-type GEM module specification (type 3)
Number of sectors/layer     :      14      18      22      26      32      42
Active volume lz [cm]       :     0.3
Spacer in r [cm]            :       2
Spacer in phi [cm]          :       2
Overlap in r [cm]           :       2
```

Figure 4.8: Format of input ASCII file conatining the information about different parameters of the MUCH detector.

beam-pipe acceptance angle goes from $0^o$ to $2.9^0$ and shielding from $3^o$ to $5.7^o$. There is no shielding below the stations where as iron is used below the absorbers as shielding which virtually means to lower the iron absorbers till the beam-pipe except first absorber. Shielding used below the first absorber is of lead (Pb). Section-4.4 will give some results about the shielding material as well as beam-pipe for MUCH. All the materials and configuration has been optimised with respect to the better S/B ratio and lowest possible detector occupancy in simulation before we have decided to use them. Figure 4.15 sketches the same picture of much detector along with the beam-pipe and shielding.

Apart from using GEANT3 for particle transport, we have performed simulation using FLUKA [89] as well to estimate the hit density on the chambers of first station. The setup used in FLUKA represents a realistic

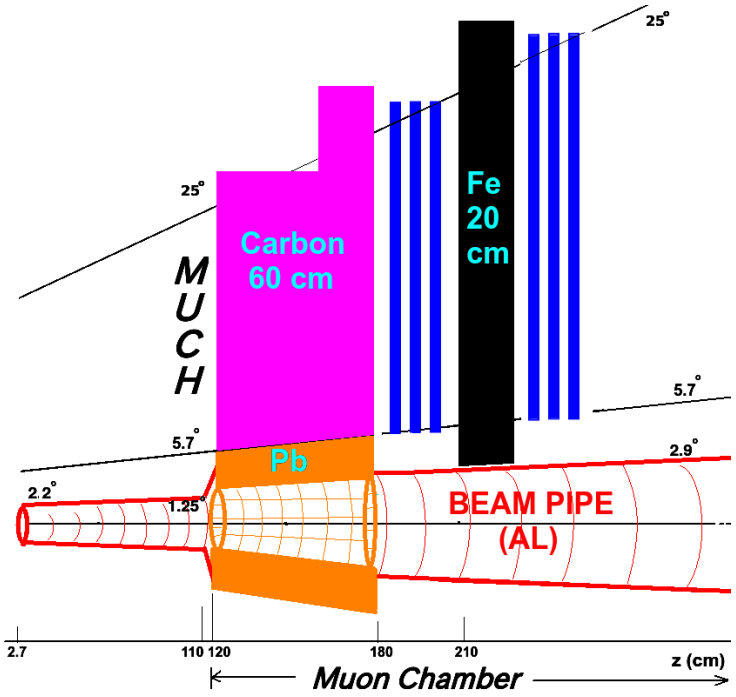


Figure 4.9: Muon Chamber detailed geometry sketch showing the beam-pipe and shielding along with the detector. Only first two stations and absorbers have been shown here.

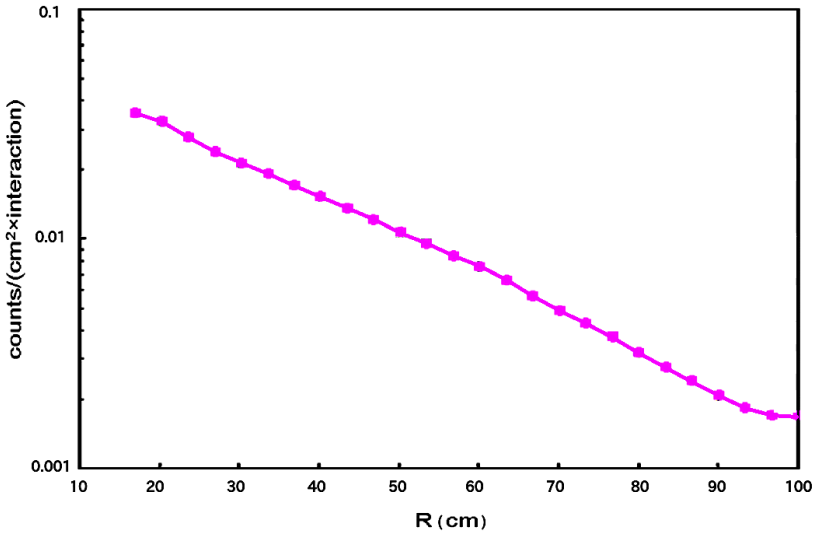


Figure 4.10: Radial distribution of the hit density of first station using FLUKA for carbon absorbers

configuration including cave architecture, beampipe, shielding around the beampipe and the beam-dump. Results from FLUKA simulation at 10 MHz interaction rate are shown for the first MUCH layer in Fig. 4.10 for 35 AGeV Au + Au collisions. The maximum hit density is about 350 kHz/cm$^2$.

### 4.3.2 Digitization

GEANT3 provides the position of energy deposition inside the detector volume. These locations along with energy depositions taken together are called **points**. To account for a realistic signal generation, the readout planes of the modules are segmented into 2-dimensional pads for obtaining final detectable response. The procedure of distributing points to pads could be divided into two steps:

1. Segmentation of the modules, and

2. Response of the detector materials to the input particles

The response function projected on a pad gives the signal on that pad and is called a **digit**. The readout plane has been divided in azimuthal direction into lines of $1^o$ separation and radially into different rings that are separated by $(r \times \phi)$, where phi corresponds to $1^o$ and r being the radial distance of the corresponding ring. This way we get 360 pads on each ring. The projective segmentation scheme has been implemented as per the optimization requirements of the modules. The pad dimensions are varied to reduce the pad occupancy and the multi-hit probability. Fig. 4.11 shows the segmentation of the

readout plane of a detector module on a layer of the first station by semi-projective pads as described in the text. The response of the detector, i.e., the distribution of the points to pads involves a fast simulation procedure of implementing the response of a gas detector to the energy deposition inside the chamber. In the detector response scheme used here, points are subjected to create primary ionization according to the Landau distribution. The multiplication follows an exponential distribution with average gain of $10^4$ to form avalanches. The avalanche spot for each primary electron is

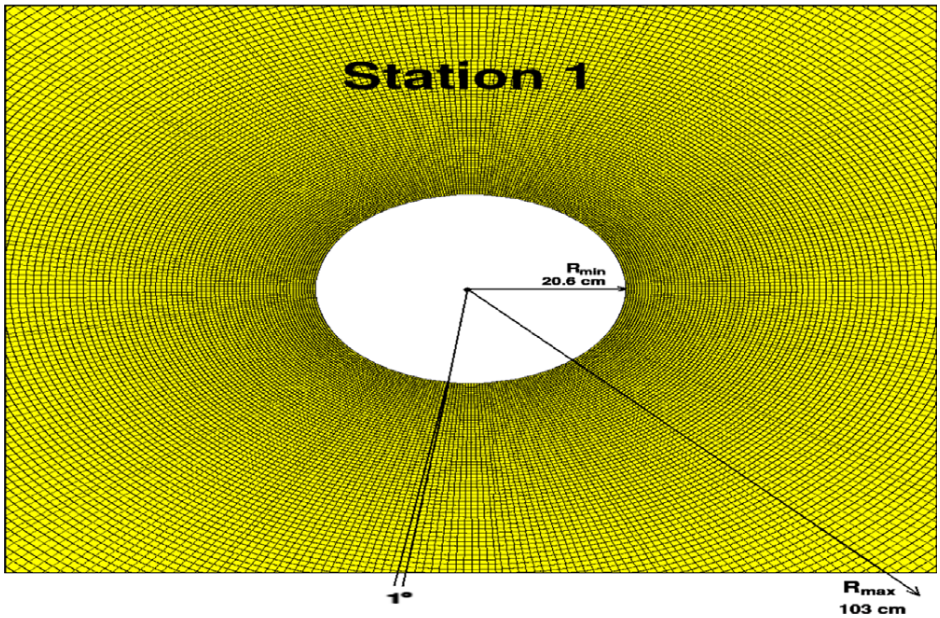


Figure 4.11: Segmentation of the readout plane of a layer of the first station of MUCH, as seen in the figure, pad dimension increases with radial distance. The azimuthal angular region has been divided into 360 lines each of $1^o$ separation.

projected to the pad plane as per the spot radius of GEM and the sum of charges on each pad has been calculated. Apart from the spot radius one can also tune the parameters like ADC resolution, the maximum charge that can be collected by a pad and the threshold charge. The maximum charge ($Q_{max}$) defines the dynamic range of the readout ASIC. If for a particular channel, the corresponding energy deposition goes beyond the specified dynamic range, the channel gets saturated. The threshold charge ($Q_{th}$) is set above the expected noise level. We set following threshold values to the above-mentioned parameters:

- *Number of ADC Channels:* 256
- $Q_{max}$ *:* 80 fC
- $Q_{th}$ *:* 1 fC and
- *GEM spot radius:* 600 $\mu$m

### 4.3.3 Clustering and Hit-Finder

Digits are grouped into **clusters** using a suitable cluster finding algorithm. Based on the particle multiplicity and associated cluster overlap, the clusters are either broken into several sub-clusters which have been treated as hits in advanced hit finder or each cluster is treated as one hit in simple hit finder. The centroids of the sub-clusters in case of broken clusters or of the main cluster in case of simple hit finder are assigned to be the locations of hits. In this simulation, advanced hit finder has been used. It is found tha for central Au+Au collisions at 25 AGeV, on an average, 1.3 tracks fall on one cluster.

### 4.3.4 Track Propagation

The main challenge of the track recognition is caused by the large multiplicity in heavy-ion collisions. About 1000 charged particles are incident from the event generator in central Au+Au collisions at 25 AGeV energy which in addition create a similar amount of secondaries via reactions in the target and detector materials. Additionally, the beam pipe shielding plays an important role in controlling the hit density on the chambers. The track reconstruction algorithm developed for MUCH is based on *track following* using the reconstructed tracks in the STS as seeds. The STS track reconstruction is based on the **cellular automaton method** [90] and STS track parameters are used as a starting point for the subsequent track prolongation. The track propagation has been performed using the **Kalman filter** procedure which takes the absorber and other materials into account [91, 92].

Tracks are propagated using the Kalman Filter technique to pass through the absorber layers. Energy loss, multiple scattering and error propagation are implemented while propagating the track [93]. Hits located within $3.5\sigma$ around the propagation point are taken as the members of the propagated track. There are two possibilities i.e., **nearest neighbor** and **branching trackings**. In the first case we take the nearest hit. In the second case we create a separate track branch for each hit in the validation gate.

For final analysis, $\chi^2$ of track and vertex fitting, number of STS tracking stations inside the magnet and the number of MUCH layers associated to

the propagated tracks are taken as track validation parameters.

### 4.3.5 Muon identification

First of all **global reconstructed tracks** are obtained by joining the STS and MUCH segments, then set of selection cuts are applied at the analysis level to identify muons. The aim is to reduce background due to hadronic tracks and muons from weak decays of pions and kaons. The selection cuts that have been applied on reconstructed tracks for the selection of muon candidates are on:

1. *STS Hits:* Number of hits from STS segment on STS detector. Maximum number of hits can be 8 corresponding to 8 STS stations

2. *MUCH Hits:* Number of hits from MUCH segment of the track on MUCH detector. Depending upon the MUCH geometry maximum number of MUCH hits may varry. For SIS300 geometry having 6 detector stations corresponding to 18 detector layers, maximum hits can be 18.

3. $\chi^2_{(STS)}$**:** $\chi^2$ of the STS segment of the track.

4. $\chi^2_{(MUCH)}$**:** $\chi^2$ of the MUCH segment of the track.

5. $\chi^2_{(Vertex)}$**:** $\chi^2$ of the track from vertex.

Based on the separation power of these cuts between signal and background, we obtain a set of final cuts for selection of muon candidates. As mentioned earlier, two different sets of cuts have been applied for the selection of muons from low mass vector mesons and charmonia. For example, while for low mass vector mesons the number of much layers could reach 15, however, for charmonium it should have more than 15 MUCH hits in order to ensure that the corresponding track has traversed the thick absorber. Set of cuts used for two cases is shown in Table 4.1.

| *Particle* | *STS hits* | *MUCH hits* | $\chi^2_{(Vertex)}$ | $\chi^2_{(MUCH)}$ |
|---|---|---|---|---|
| $J/\psi$ | 7 | 17 | 2.0 | 1.5 |
| LMVM | 6 | 14 | 2.0 | 1.5 |

Table 4.1: Sets of cuts used for low mass vector mesons and $J/\psi$ analysis. Note that for the case of low mass vector mesons, the stations beyond the thick absorber are not taken in the analysis

## 4.4 MUCH Beam-pipe and its Shielding

### 4.4.1 Beam-Pipe Shielding

In CBM experiment, probability of the primary beam interaction with the target is just 1%. Nearly 100% of the beam propagating till beam-dump might interact with the beam-pipe to generate radiation background affecting the detectors. Purpose of the beam-pipe shielding is to reduce such background without affecting the detection process.

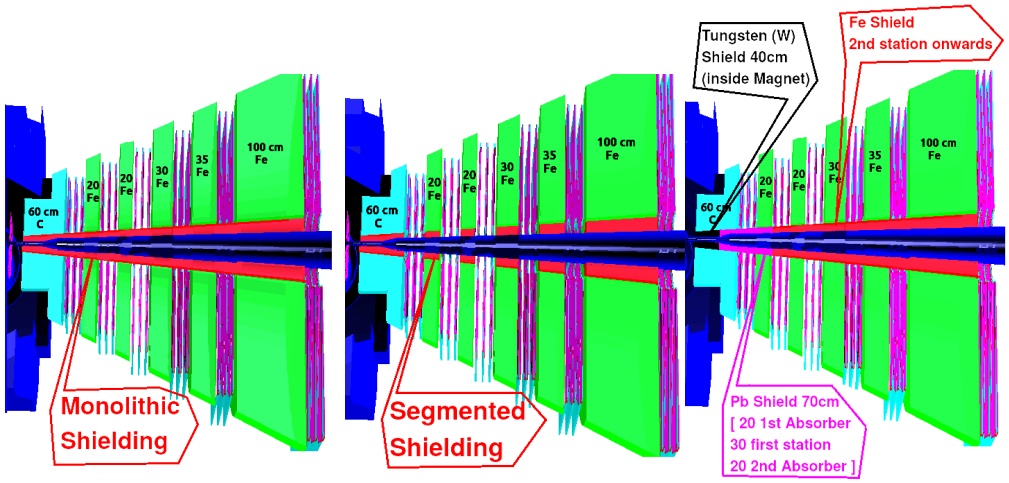


(a) monolithic (b) segmented (c) W+Pb+Fe

Figure 4.12: Muon Chamber with (a) Monolithic, (b) Segmented, and (c) New Optimized Combination [W(40cm) + Pb(70cm) + Fe(335cm)] beam-pipe shielding set-up for 25 AGeV central Au+Au collisions

Performance of muon chamber (SIS300 set-up) for different type of beam-pipe shielding materials (like tungsten, lead, iron) has been analysed in two ways: (1) using complete monolithic shielding as shown in Fig. 4.12a, and

(2) using segmented shielding with no shield beneath the stations as shown in Fig. 4.12b. Performance of a new monolithic shielding, which is a combination of 40cm W (tungsten), 70cm Pb (lead) and 335 cm Fe (iron), have also been demonstrated as shown in Fig. 4.12c. At present in simulation we are using segmented shielding with 60 cm Pb beneath the first absorber and Fe beneath the rest of the absorbers with no shielding below the detector stations.

Present work has been done using GEANT3 with heavy ion collision events at 25 AGeV Au+Au given by the UrQMD event generator for background and signal ($\omega$) from the PLUTO event generator.

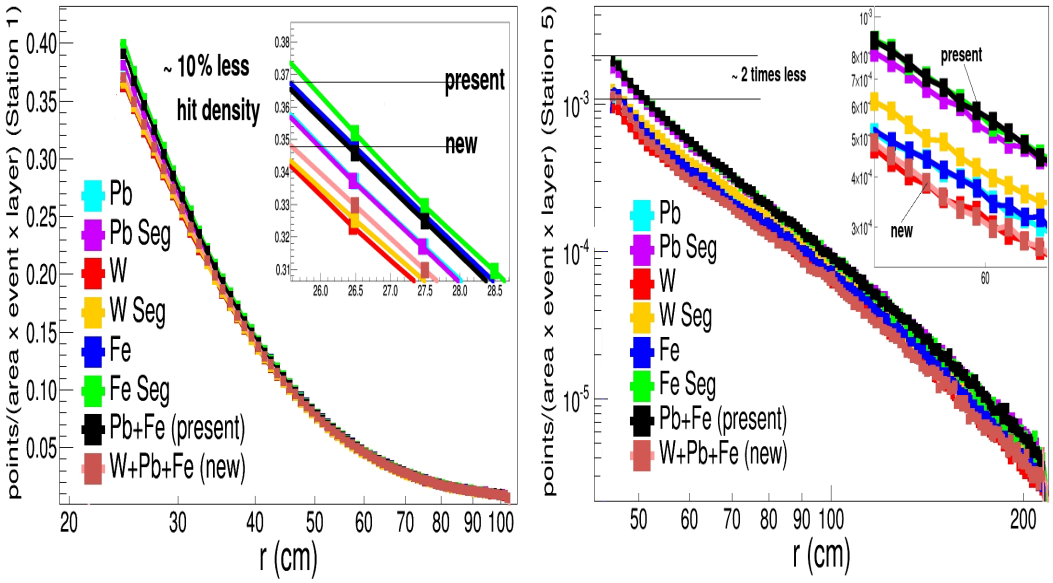


(a) $1^{st}$ station (b) $5^{th}$ station

Figure 4.13: point density at 25 GeV collision energy of MUCH detector station: (a) $1^{st}$ (left panel) & (b) $5^{th}$ (right panel) for different beam-pipe shielding materials (here **Pb/W/Fe** means monolithic lead/tungsten/iron shielding and **Pb/W/Fe seg** means segmented lead/tungsten/iron shielding)

Fig. 4.13 shows the point density at the $1^{st}$ station which is lowest for monolithic tungsten case and 10 % less for new combination than present shielding and at the $5^{th}$ detector station its minimum for monolithic tungsten and new combination but high for present scheme. It can also be seen that monolithic shielding is performing better than the segmented shielding on

$5^{th}$ station where hit density is relatively low. Same is true for occupancy results.

Next we analyzed the overall detector performance in terms of reconstruction efficiency and background reduction. Cuts used are: STS hits $\geq 6$, much hits $\geq 14$, $\chi^2_{vertex} \leq 2.0$, $\chi^2_{much} \leq 1.5$ The efficiency for $\omega$ is $\sim$1% which

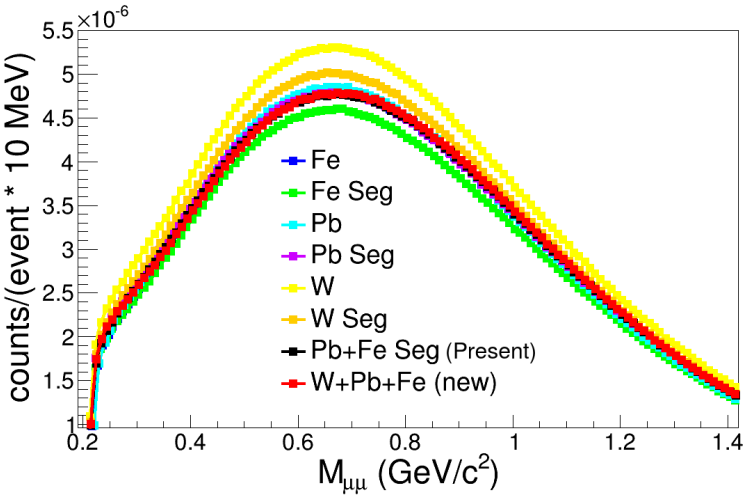


Figure 4.14: Combinatorial background from MUCH detector after applying the proper conditions at central Au+Au collisions at 25 A GeV

doesn't show any change for different shielding materials. From Fig. 4.14 one can see that highest background is for the monolithic tungsten shield which even though gives the lowest hit-density. Segmented iron shield gives the least background but high hit-density. Whereas, our new combination (W+Pb+Fe) gives both low hit-density as well as low background hence the best compromise between hit-density/occupancy and the background reduction.

### 4.4.2 Beam-Pipe for MUCH

Beam-pipe is one of the important component in the detector set-up to carry the beam till the beam-dump. This is more important in a sense as only 1% of the interaction is expected at the target in CBM scenario, which means almost 99% of the beam needs to be dumbed to avoid any radiation damage

etc. With time, geometry of the muon detector especially first absorber kept on changing, corresponding changes need to be incorporated in the beam-pipe for MUCH. Keeping in mind the present geometry information, Figure 4.15a shows the sketch of the configuration including the shielding and beam-pipe that is used in MUCH simulations. It is seen that this geometry leaves some empty spaces below the shielding and beam-pipe which is more prominent below first absorber, and between the MUCH absorbers and the shielding. These gaps need to be filled to avoid any secondary interactions and to absorb unwanted particles so that the detector occupancy could further be reduced without the deterioration of overall detection process.

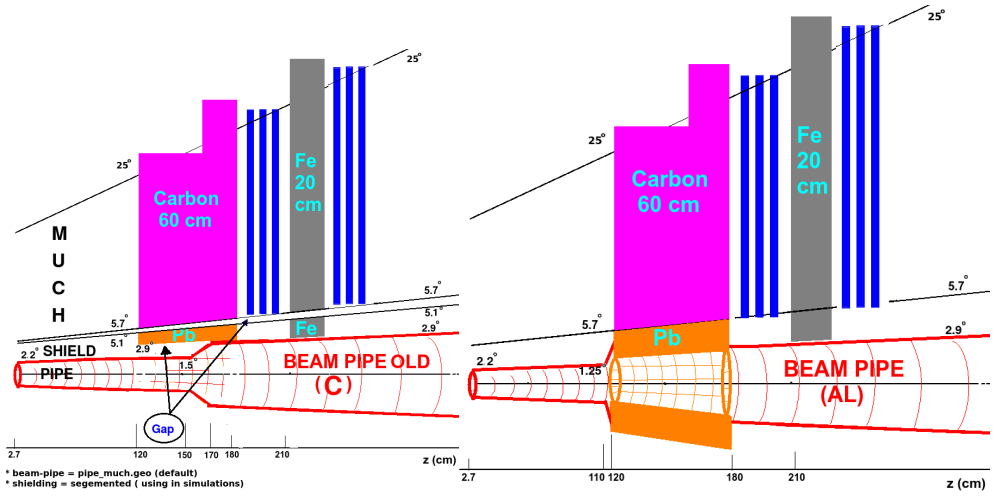


(a) old beam-pipe (b) new beam-pipe

Figure 4.15: Sketch of Muon detector first two stations & absorber with: (a) old MUCH beam-pipe (left panel) & (b) new MUCH beam-pipe

New geometry has been proposed, sketch shown in figure 4.15b, which fills all the unwanted gaps. Moreover, lead shielding below first absorber is made as a part of the beam-pipe. We expect an improvement in occupancy near the beam-pipe region of the detector station. Plot of the point-density for first detector station superimposed over the result of old-pipe is shown in figure 4.16a. It is seen that almost 10% reduction in occupancy is there for the first station near the beam-pipe region. Moreover, we tried different types of materials for the beam-pipe and analysed the same for effects, if any,

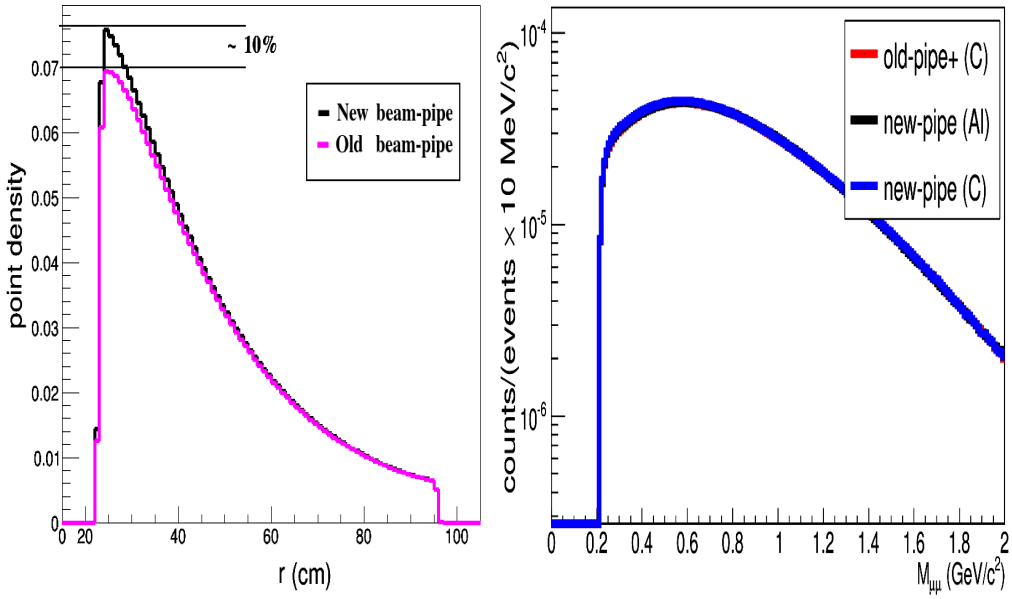


(a) old vs new (b) pipe materials

Figure 4.16: (a) Point density of first detector station of Much using two types of beam-pipe geometries (old & new).(b) reconstructed background for different type of beam-pipe materials

on the overall muon detection. Figure 4.16b shows that there is no effect on the reconstructed background. We have also seen no effect on the signal, hence there is no effect on S/B ratio if we choose any beam-pipe material among the options given. Certainly we would like to go with the cheaper one which is aluminium(Al) in this case.

As already discussed, lead shielding below first absorber is proposed to be part of beam-pipe, so one needs to optimise its opening-hole. For the purpose CBM-ION generator has been used which generates beam of Au (gold) ions. Shape of the beam is determined by the four gaussians, two gaussians represent the spatial distribution like vertical and horizontal (x,y) and other two gaussians represent angular distribution (Px/P, Py/P). Parameters for gaussian are taken from figure 4.17a which shows the beam spot diameter at different incident beam energies. For 4 GeV and 8 GeV beam-spot radius is expected to be 1 mm and 0.5 mm respectively. For the simple case we have first started beam just after the target and then transported it using

GEANT3 under magnetic field via beam-pipe allowing it to develop halos etc. Gold ions beams have been analysed in the energy range from 4 to 8 GeV where beam-halos are expected to be more prominent.

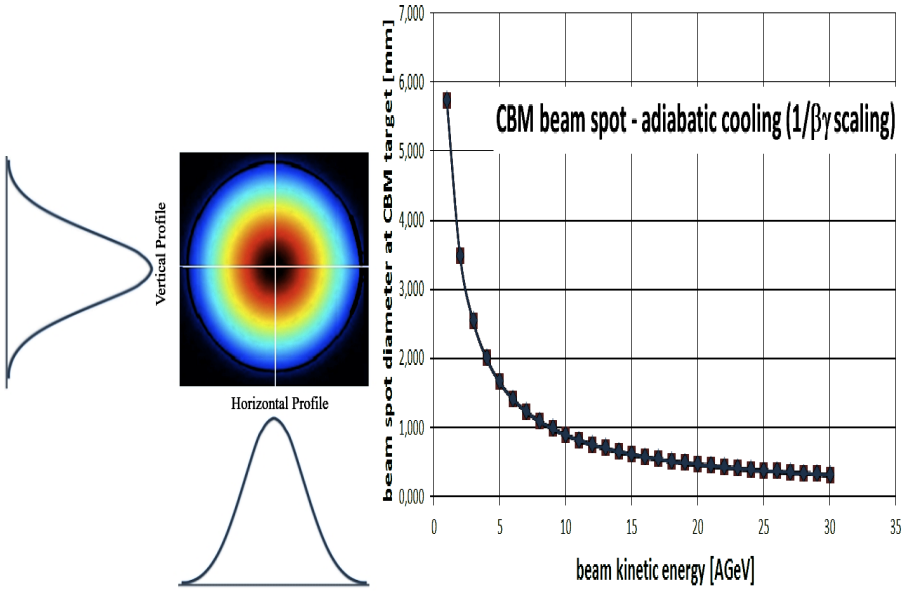


(a) beam spot (b) beam spot size

Figure 4.17: (a) Sketch of beam-spot (left panel) & (b) Beam-spot size with beam kinetic energy

We have used CBM-MUCH setup with ECAL (electromagnetic calorimeter) as shown in Figure 4.18a. Figure 4.18b shows view of lead with hole which is to be optimised. Procedure is to allow the incident ions to pass through the lead-hole whose radius is varied in steps and then after its passage it deposits its energy on ECAL. We integrate out all the energy deposited on ECAL then compare with the incident energy ($E_{ecal}/E_{in}$) to look for the losses expected when there is any interaction of beam and lead-hole. Moreover, we analyse the hits on both sides of the lead-hole. This is done by analysing hits on STS (downstream) and MUCH first station (upstream) to look for hits from the particles produced due to the beam and lead interaction, if any, as there is no other particle transport done.

From the Figure 4.19a it can be seen that till the 20 mm radius of lead-hole there is an interaction of the beam of incident energy 4 GeV per nucleon with

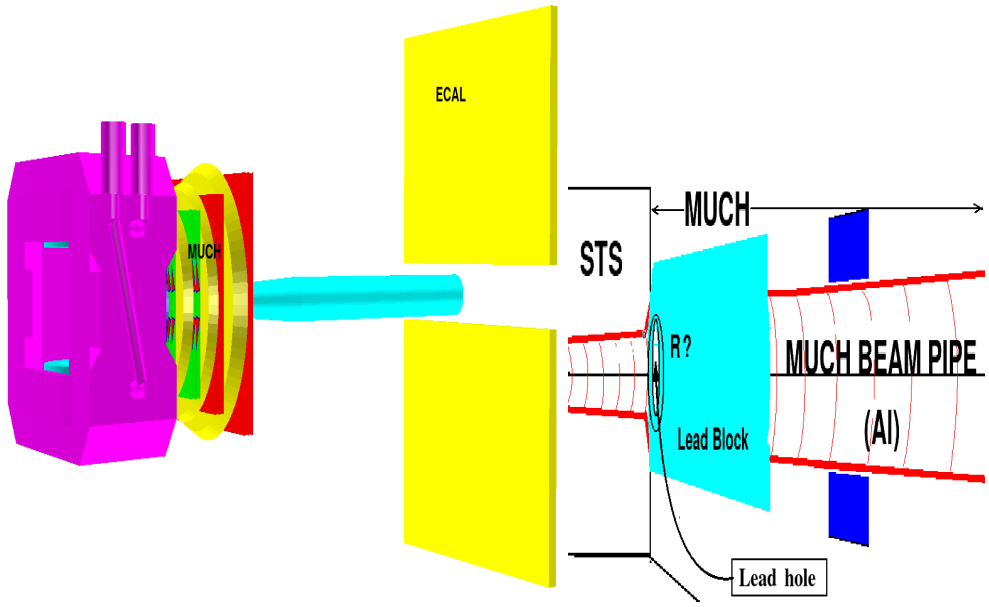


(a) MUCH+ECAL (b) lead opening view

Figure 4.18: (a) MUCH detector layout with ECAL in the set-up. (b) lead-opening view

lead producing secondaries which as a result give hits upstream the MUCH on STS last station. While if we keep increasing the radius of lead-opening there is reduction of hits seen on STS but hits on MUCH starts increasing till some radius of lead-hole ($\sim$ 30mm). There is an interaction of beam inside and downstream the lead-hole as a result of which secondaries are produced giving hits on the MUCH first detector station. If this is really the case then we should record the loss in the energy ($E_{ecal}$) deposited in the ECAL till 30mm. This is what has been seen from the ratio $E_{ecal}/E_{in}$ from figure4.19a, where $E_{in}$ is the incident energy of beam. It is clear from the above discussion that beam finds safe passage without the loss of any energy above 30mm radius of the lead-opening. It must be mentioned here since we have started beam just after the target so in case of beams interacting with the target we expect safer limit to be higher than the above findings. We usually take $3^o$ outer acceptance angle of the beam-pipe which is safest limit in any case.

One more important aspect studied is the effect of the magnetic field on the beam. For energies greater than 8 GeV, usually full strength of magnetic

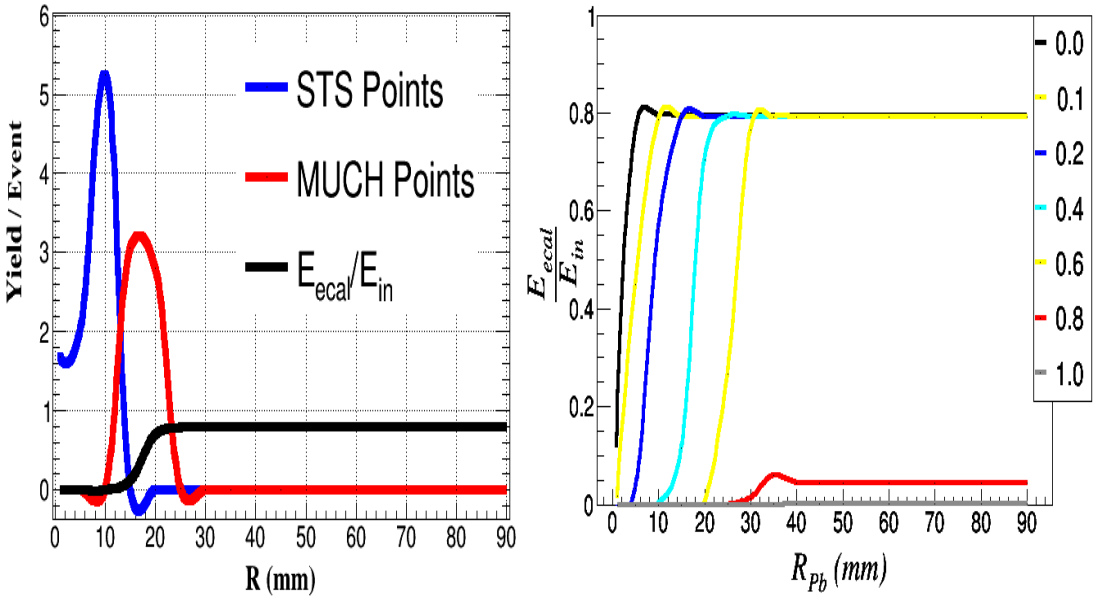


(a) hits Vs lead hole

(b) Energy loss Vs lead hole

Figure 4.19: (a) Hits(points) of STS & MUCH Sketch, and ECAL over incident energy range for different lead-hope radius at 4 GeV. (b) ECAL/ INCIDENT energy ratio with lead-hole radius at different magnetic field strengths ( scale 1 corresponds to 2 Tesla)

field ($\sim$ 2 $Tesla$) is used in simulations. But for lower energies say at 4 GeV magnetic field strength needs to be lowered to avoid any deflection in the beam which could stop its passage till the beam-dump. Magnetic field strength has been varied from scale 1 to 0 in steps and corresponding $E_{ecal}/E_{in}$ ratio has been analysed with lead-hole radius. Figure 4.19b shows the results where one can observe that upto 0.6 scale there is a corresponding value of lead-hole radius above which almost no loss in the incident beam-energy is seen. But above 0.6 its observed that beam gets lost reflected by zero energy ratio. If the same is repeated for 8 GeV, no such disappearance of beam is seen at any scale. In conclusion, magnetic field strength for lower energies need to be lowered below 0.6×2 Tesla when the incident beam-energy is 4 GeV. We have decided to take the value of 0.4×2 Tesla of Magnetic field for 4 GeV incident beam energy.

# Chapter 5

# PHYSICS PERFORMANCE OF MUCH

In this chapter the feasibility studies of muon detector will be discussed at 25 A GeV central Au + Au collisions given by the UrQMD event generator [84]. The phase-space distribution of dimuon signals is modeled using the PLUTO Monte Carlo generator [85]. In this simulation, GEANT3 [86] has been used as the transport code. Full reconstruction has been performed in order to determine the efficiency and signal to background ratio in dimuon measurements over a wide range of invariant mass i.e., from low mass vector mesons to charmonia. Results of performance studies will be discussed in this chapter followed by conclusions.

## 5.1 Input to the Simulations

In this study, the event generators PLUTO and UrQMD3.3 have been used for generating signals and background events, respectively.

### 5.1.1 Event Generator

#### PLUTO

PLUTO event generator was originally developed for the HADES experiment later used by other collaborations in the hadronic field as well as future FAIR experiments like PANDA and CBM. Pluto is a collection of C++ classes, adding up to the framework of a simulation package for hadronic physics interactions in the energy regime up to a few GeV makes use of ROOT only, without requiring additional packages. The output may be analyzed on line, or further forwarded to a digitization package. The Pluto framework includes models for hadronic and electromagnetic decays, resonance spectral functions with mass-dependent widths, and anisotropic angular distributions for selected channels. A decay-manager interface enables "cocktail" calculations. An extensive particle data base is available, with capabilities to support user-defined ones. Various particle properties and decay modes are included in the data base. Thermal distributions are implemented, enabling multi-hadron decays of hot fireballs.

PLUTO has been used to generate the phase space distributions and decay of the vector mesons and charmonia for CBM-MUCH detector simulations. The signal multiplicities required for estimation of signal to background ratio are taken from the Hadron String Dynamics (HSD), a transport model that has been found to match the global data in these energy ranges quite satisfactorily [94].

For simulating the performance of the muon detection system, we have taken two types of dimuon inputs: decays from low mass vector mesons and from $J/\psi$ in the charmonium channel. In the low mass region we considered channels like $\omega \rightarrow \mu\mu,\ \omega \rightarrow \pi^0\mu\mu,\ \eta \rightarrow \mu\mu,\ \eta \rightarrow \gamma\mu\mu,\ \rho^0 \rightarrow \mu\mu,\ \phi \rightarrow \mu\mu$ to form the cocktail. We define invariant mass $\mathrm{M}_{\mu^+\mu^-}$ of a pair of decayed muons as:

$$p^{\mu}p_{\mu} = (E_{\mu^+} + E_{\mu^-})^2 - \sum(p_{i,\mu^+} + p_{i,\mu^-})^2 = M_{\mu^+\mu^-} \tag{5.1}$$

Where $\mathrm{p}^{\mu}$ ($\mathrm{p}_{\mu}$) is 4-momentum, $\mathrm{E}_{\mu^+}$ ($\mathrm{E}_{\mu^-}$) is the energy of $\mu^+$ ($\mu^-$) muon,

and $p_{i,\mu^+}$ ($p_{i,\mu^-}$) is the i = x, y and z components of the $\mu^+$ ($\mu^-$) muon momentum. Rapidity of the muons pairs is defined as:

$$y_{\mu^+\mu^-} = \frac{1}{2} ln \frac{(E_{\mu^+} + E_{\mu^-}) + (p_{z,\mu^+} + p_{z,\mu^-})}{(E_{\mu^+} + E_{\mu^-}) - (p_{z,\mu^+} + p_{z,\mu^-})} \tag{5.2}$$

The invariant mass distribution of the cocktail taken as input for the simulation of 25 AGeV Au+Au collisions is shown in Fig. 5.1.

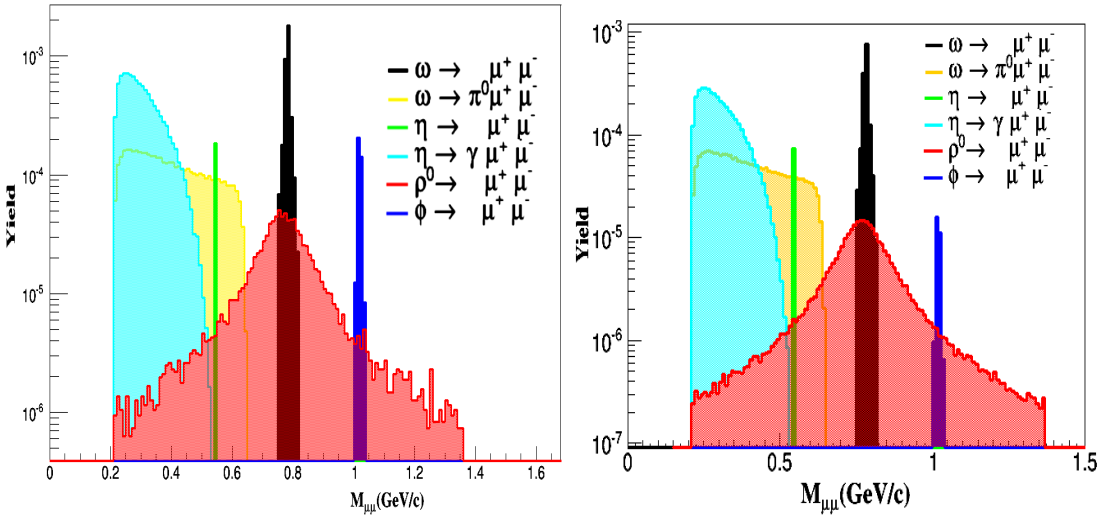


(a) 25 AGeV (b) 8 AGeV

Figure 5.1: Cocktail of different dimuon sources at the low mass region of the invariant mass spectra as used in the simulation for Au+ Au Collisions at energy: (a) 25 AGeV (b) 8 AGeV

Important effect that has been taken into account in PLUTO for realistic simulations of hadronic interactions is the deviations of resonance shapes from the fixed-width Breit-Wigner distributions, which is typically modeled as a mass-dependent in the resonance width. This is important for resonances with large widths, such as the $\rho$ meson. The $\rho$ meson mass distribution is generated by including a Breit-Wigner shape arround the pole mass, thermal phase space factors, and a factor $1/M^3$ to account for vector meson dominace in the decay into $\mu^+\mu^-$. Shape of the $\rho$ meson is shown in figure 5.2a.

Figur 5.2 shows different spectra of different cocktail resonances from PLUTO event generator. We can note that rapidity distribution for different

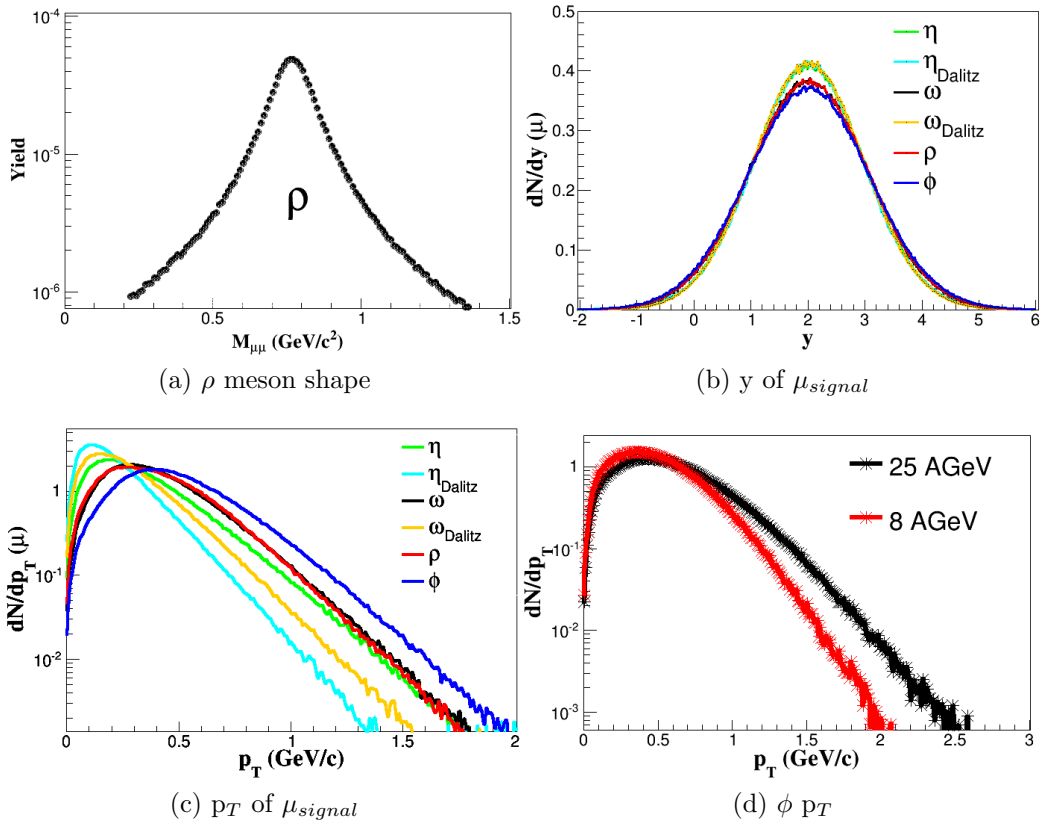


(a) $\rho$ meson shape (b) y of $\mu_{signal}$

(c) $p_T$ of $\mu_{signal}$ (d) $\phi$ $p_T$

Figure 5.2: Spectra of LMVM resonances from PLUTO at 25 AGeV Au+ Au collisions energy: (a) Shape of $\rho$ meson whose pole mass is fixed by Breit-Wigner distribution, (b) Rapidity distribution of muons from all resonances of cocktail superimposed over each other, (c) $p_T$ distribution of muons from all cocktail sources, (d) $p_T$ distribution of $\phi$ mesons at 8 AGeV and 25 AGeV superimposed.

low mass vector meson sources is nearly gaussian with rapidity distribution width ($\sigma_y$) $\sim$ 2. For $J/\psi$, $\sigma_y$ $\sim$ 0.23. Thermal $p_T$ distributions for different sources are nearly exponential with value for temperature (T) $\sim$ 140 MeV. Similarly, the values of temperatures used as slope parameters in PLUTO for $J/\psi$ is taken to be 170 MeV. Figure 5.2d shows the $p_T$ distributions at two different energy regions namely 8 AGeV and 25 AGeV, former will be available at FAIR in first phase called SIS100 and later at second phase called SIS300. Transverse flow factor ($\beta$) has been taken as zero ($0c$) for these resonances in the event generator. PLUTO uses these parameters i.e. $T$, $\beta$ & $\sigma_y$ for generating resonance decay events and their corresponding distributions.

| particles | M (MeV) | 10 AGeV | 15 AGeV | 20 AGeV | 25 AGeV | 30 AGeV | 35 AGeV |
|---|---|---|---|---|---|---|---|
| $\pi^0$ | 135 | 221 | 264 | 300 | 337 | 361 | 382 |
| $\pi^-$ | 140 | 233 | 293 | 333 | 368 | 397 | 423 |
| $\pi^+$ | 140 | 201 | 261 | 298 | 332 | 361 | 386 |
| $\eta$ | 550 | 16 | 23 | 29 | 33 | 37 | 40 |
| $K^0$ | 498 | 21 | 31 | 37 | 42 | 47 | 52 |
| $\bar{K}^0$ | 498 | 3 | 7 | 9 | 12 | 14 | 17 |
| $K^+$ | 494 | 20 | 28 | 35 | 40 | 45 | 48 |
| $K^-$ | 494 | 3 | 7 | 9 | 13 | 16 | 18 |
| $\rho^0$ | 775 | 9 | 15 | 19 | 23 | 25 | 26 |
| $\omega^0$ | 783 | 19 | 27 | 34 | 38 | 42 | 46 |
| $\phi$ | 1020 | 0.12 | 0.50 | 0.83 | 1.28 | 1.24 | 1.50 |
| $\Lambda$ | 1115 | 20 | 26 | 30 | 32 | 34 | 35 |
| $\Sigma^0$ | 1193 | 5.99 | 8.09 | 9.20 | 10.06 | 10.56 | 10.76 |
| $\Sigma^+$ | 1189 | 4.19 | 5.69 | 6.55 | 7.18 | 7.72 | 8.74 |
| $\Sigma^-$ | 1197 | 3.30 | 4.04 | 4.61 | 5.46 | 5.37 | 5.67 |
| $\Xi^0$ | 1315 | 0.13 | 0.20 | 0.34 | 0.40 | 0.45 | 0.45 |
| $\Xi^-$ | 1321 | 0.18 | 0.22 | 0.32 | 0.48 | 0.33 | 0.42 |
| $D^0$ | 1864 | $1.15E{-}11$ | $2.72E{-}7$ | $6.67E{-}6$ | $3.74E{-}5$ | $1.11E{-}4$ | $2.49E{-}4$ |
| $\bar{D}^0$ | 1864 | $8.76E{-}9$ | $2.97E{-}6$ | $3.05E{-}6$ | $1.15E{-}4$ | $2.78E{-}4$ | $5.43E{-}4$ |
| $D^+$ | 1869 | $1.67E{-}11$ | $3.34E{-}7$ | $7.71E{-}6$ | $4.17E{-}5$ | $1.21E{-}4$ | $2.67E{-}4$ |
| $D^-$ | 1869 | $6.76E{-}9$ | $2.28E{-}6$ | $2.34E{-}5$ | $8.91E{-}5$ | $2.16E{-}4$ | $4.23E{-}4$ |
| $D_s^+$ | 1969 | $2.13E{-}14$ | $1.71E{-}8$ | $7.50E{-}7$ | $5.43E{-}6$ | $1.84E{-}5$ | $4.53E{-}5$ |
| $D_s^-$ | 1969 | $2.18E{-}11$ | $6.67E{-}8$ | $1.26E{-}6$ | $6.59E{-}6$ | $1.92E{-}5$ | $4.29E{-}5$ |
| J/$\psi$ | 3097 | $1.74E{-}7$ | $2.44E{-}6$ | $8.37E{-}6$ | $1.92E{-}5$ | $3.45E{-}5$ | $5.49E{-}5$ |
| $\psi'$ | 3686 | $1.07E{-}10$ | $1.69E{-}8$ | $9.09E{-}8$ | $2.56E{-}7$ | $5.66E{-}7$ | $9.96E{-}7$ |

Table 5.1: Multiplicities of different particles calculated using HSD code for central (b=0.5) Au-Au collisions at different beam energies. Here say E-5 means $10^{-5}$ and M = mass.

As already mentioned, multiplicity of resonances from PLUTO is one per event which has been done to increase the statistics. In the analysis, contributions from these enhanced sources need to be normalized. Normalisation of PLUTO signals is done according to their mean multiplicities as predicted by the HSD model and the branching ratios. The mean multiplicities, decay channels and branching ratios of background and signal sources are presented in Table 5.1, 5.2.

### UrQMD

The simulation were perfomed for central Au-Au collisions at a beam energy of 25 AGeV. The final state phase space distributions of hadrons were generated using UrQMD the relativistic transport code. UrQMD forms the source of background in the simulations where signal particles from PLUTO are embedded event by event during the transport. Main source of background

| particles | decay channel | Branching Ratio |
|---|---|---|
| $\eta$ | $\mu^+\mu^-$ | $5.6\times10^{-6}$ |
| $\rho^0$ | $\mu^+\mu^-$ | $4.55\times10^{-5}$ |
| $\omega$ | $\mu^+\mu^-$ | $9\times10^{-5}$ |
| $\phi$ | $\mu^+\mu^-$ | $2.87\times10^{-4}$ |
| J/$\psi$ | $\mu^+\mu^-$ | $5\times10^{-5}$ |
| $\eta_{Dalitz}$ | $\gamma\mu^+\mu^-$ | $3.1\times10^{-4}$ |
| $\omega_{Dalitz}$ | $\pi^0\mu^+\mu^-$ | $1.3\times10^{-4}$ |

Table 5.2: Branching ratio of some important resonances taking from particle data group (PDG) data-base.

muons comes from pion and kaon decays. In central Au-Au collisions at 25 AGeV about $600\pi^{\pm}$ and $50K^{\pm}$ are produced per event in full phase space. Whereas, at 8 AGeV about $270\pi^{\pm}$ and $20K^{\pm}$ are produced per event in full phase space. Moreover, on an average there is one leptonic decay of low mass vector mesons, excluding $\eta$ Dalitz, in 400 events.

Figure 5.3 shows different spectra of pions and kaons from UrQMD. Comparison has been made at 8 GeV and 25 GeV collision energies for momentum spectra, transverse momentum spectra, rapidity spectra of pions and kaons generated by UrQMD event by event. UrQMD is used to calculate the combinatorial background in simulations using super-event technique already discussed in earlier chapters. Here we create pairs of the same-charge sign leptons in the event for like sign method, and opposite charged pairs for unlike-sign method. Since UrQMD is the only source of background, so combinatorial background (CB) for the two cases normalized per event is:

$$\mathbf{N}_{CB} = \mathbf{N}_{\mu^+\mu^-} \quad \text{(unlike sign)}$$
$$\mathbf{N}_{CB} = \mathbf{2}\sqrt{N_{\mu^+\mu^+}N_{\mu^-\mu^-}} \quad \text{(like sign)}$$

Where $N_{CB}$ is the yield per event from the combinatorial background in a certain invariant mass bin and $N_{\mu^+\mu^-}$, $N_{\mu^+\mu^+}$, and $N_{\mu^-\mu^-}$ are the number of counts from the postive-negative, positive-positive, and negative-negative charged sign muon pairs respectively in the same invariant mass bin. To obtain the signal this calculated combinatorial background is subtracted from

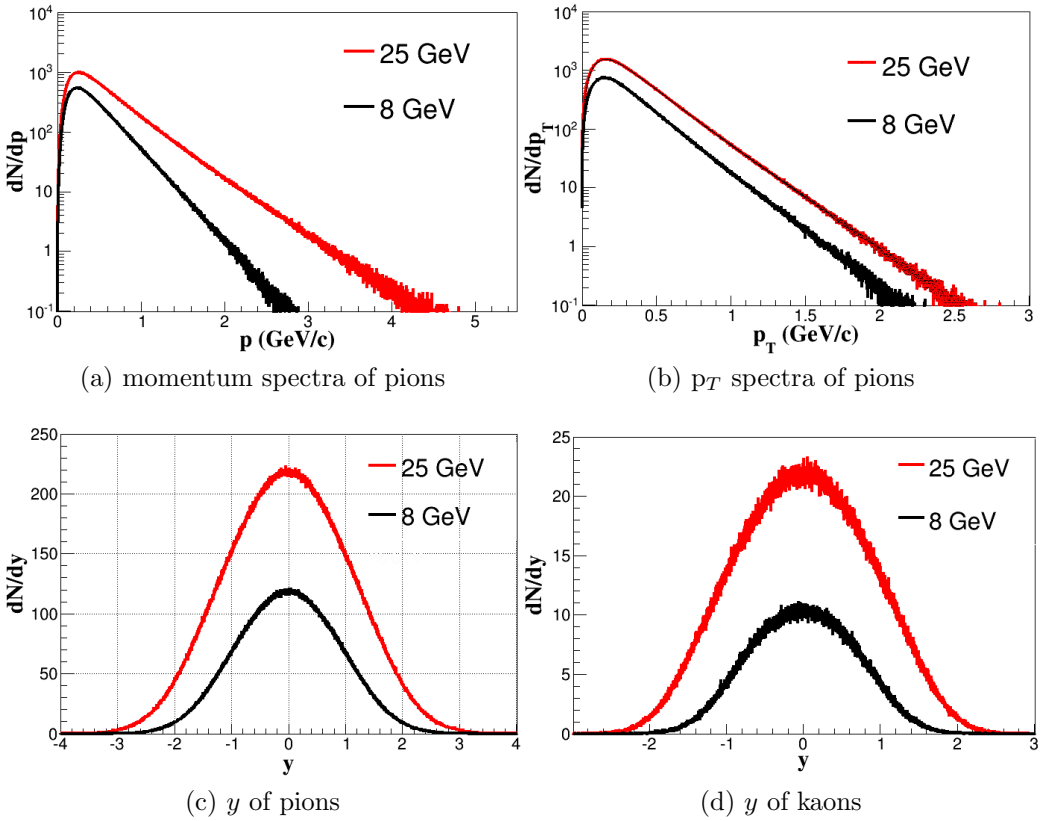


(a) momentum spectra of pions

(b) $p_T$ spectra of pions

(c) $y$ of pions

(d) $y$ of kaons

Figure 5.3: Spectra of pions and kaons from UrQMD at 25 AGeV compared with 8 AGeV Au+ Au collisions energy: (a) momentum spectra of $\pi$ meson, (b) $p_T$ spectra of $\pi$ meson, (c) Rapidity distribution of $\pi$ meson, (d) Rapidity distribution of $K$ meson, all are superimposed for two energies.

the full spectra (from experiment or simulation). Figure 5.4 shows the comparison of the combinatorial background from UrQMD for like sign and unlike sign reconstructed muon pairs at SIS100 MUCH detector configuration. One can see from the figure that $2\sqrt{N_{\mu^+\mu^+}N_{\mu^-\mu^-}}$ and $N_{\mu^+\mu^-}$ almost give the same combinatorial background while the number of $\mu^+\mu^+$ pairs are always much greater than $\mu^-\mu^-$ pairs. For CBM simulation we are using unlike sign method for the background estimation.

It must be mentioned here that UrQMD by default do the calculation in center of mass frame. In order to get the events in $E_{lab}$ one has to boost the particles manually in laboratory frame. Above spectra's from UrQMD are from centre of mass frame ($\sqrt{s}$) calculations and that of PLUTO are from laboratory frame ($E_{lab}$) calculations.

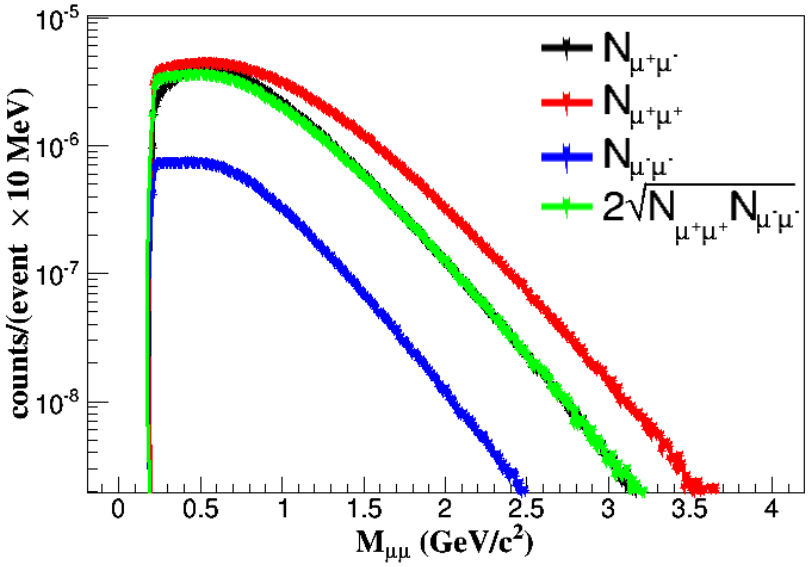


Figure 5.4: Comparison of combinatorial background using superevent technique for like sign and unlike sign reconstructed muon pairs at 10 AGeV Au + Au collisions.

## 5.2 Detector performace of low mass vector mesons at 25 GeV

In the following, the invariant mass spectra of the reconstructed dimuons have been discussed separately for low mass vector mesons and $J/\psi$. For background estimation, the invariant mass spectra has been calculated from the reconstructed muons from UrQMD-only events without embedding any signal into it. In order to increase the statistics in the background calculation the superevent technique has been applied, where reconstructed tracks from a large number of central UrQMD events were mixed, and then used to calculate the combinatorial background. The signal efficiency was determined by reconstructing the signal-particle (e.g. $J/\psi$, $\rho^0$, $\omega$ ) that was embedded event by event into the UrQMD events. For the calculation of the final signal to background ratio, the signal multiplicity and branching ratios were taken into account along with the proper normalization of the background. In Fig. 5.5a, the invariant mass distribution of the reconstructed muon pairs from low mass region is shown together with the combinatorial

background. Fig. 5.5b depicts the signal-to-background ratio, S/B as extracted from Fig. 5.5a. This value is important for the accuracy of the signal extraction and has been found to be comparable or better to the existing or planned muons systems in high energy heavy ion collision experiments at similar energies. The significances are 214.6, 21.4 and 44.7 for $\omega$, $\rho^0$ and $\phi$ respectively.

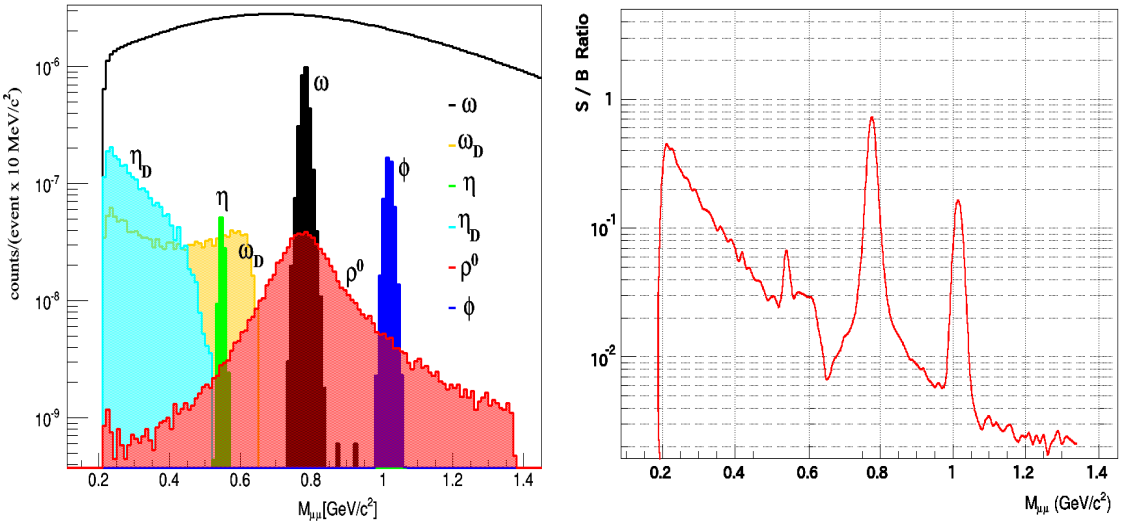


(a) Reconstructed Cocktail (b) Signal/Background Ratio

Figure 5.5: (a) Invariant mass distributions of reconstructed muon pairs from decaying low mass vector mesons together with the combinatorial background simulated for central Au + Au collisions at 25 AGeV. (b) Signal to background ratio of the low mass dimuon invariant mass spectra.

The overall efficiencies (including overall geometrical detector acceptance) are shown in table 5.3. These values depend strongly on the set of cuts used and could therefore be adjusted by varying the cuts. It should be noted that, a significant loss of efficiency takes place at different steps before it reaches the muon system. These include geometrical acceptance, STS track reconstruction efficiency, STS-MUCH track matching efficiency.

STS effeciency at MUCH optimised cuts is just $\sim 17\%$ for low mass vector mesons. If we consider the particles detected by the muon system in terms of the fraction of particles reconstructed by STS, then the efficiency goes up even by a factor of six varying somewhat with the particle type at 25 AGeV

| **Particle** | $\in (STS + MUCH)$ | $\in (STS)$ | $\in (MUCH)$ (%) |
|---|---|---|---|
| $\omega$ | 0.83 | 17.1 | 4.9 |
| $\omega_{Dalitz}$ | 0.29 | 16.5 | 1.8 |
| $\eta$ | 0.46 | 17.3 | 2.7 |
| $\eta_{Dalitz}$ | 0.22 | 16.4 | 1.3 |
| $\rho$ | 0.81 | 16.9 | 4.8 |
| $\phi$ | 1.47 | 17.0 | 8.7 |

Table 5.3: Reconstructed signal particle effeciencies of STS and MUCH for central Au+Au collisions at 25 A GeV

central Au+Au collision energy.

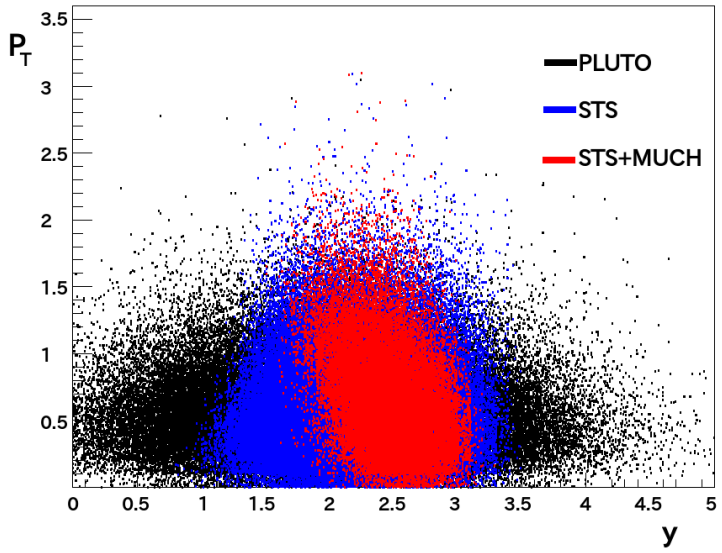


Figure 5.6: y-$p_T$ acceptance of the reconstructed $\rho^0$ superimposed over STS and input $4\pi$ acceptance from pluto at central Au + Au collisions at 25 AGeV.

Figure 5.6 shows the y-$p_T$ acceptance of the reconstructed $\rho^0$ mesons at STS and MUCH superimposed over input acceptance ($4\pi$) from PLUTO. There is a considerable acceptance loss at the STS before the MUCH detector of hadronic absorbers is placed. It is observed that only the region from mid-rapidity (1.99 for 25 AGeV Au + Au collisions) towards forward rapidity is covered by the detected particles.

The composition of the reconstructed background tracks per event for low mass vector mesons from central Au + Au collisions at 25 AGeV is shown in

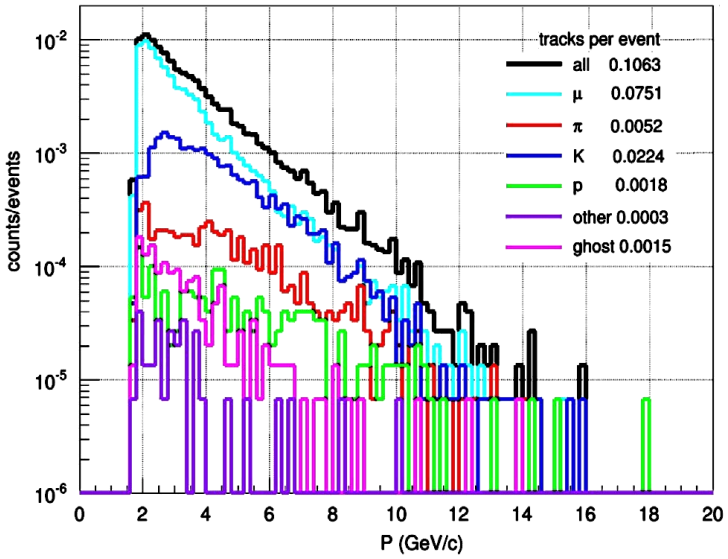


Figure 5.7: Composition of the reconstructed background tracks for low mass vector mesons from central Au + Au collisions at 25 AGeV.

Fig. 5.7. The dominant contributions are muons from weak decays of pions and kaons. At higher momenta, the yield of punch-through kaons is also significant. It is expected that the inclusion of TOF in the analysis chain will reduce this background even further by the use of timing cuts on particles like proton.

## 5.3 Using Time of Flight Detector

Primarily Time of Flight (ToF) detector is used for the particle identification (PID). The PID is done by first matching the resolved particle tracks with valid hits in ToF detector. After proper calibration, ToF detector is able to measure the particle velocity which together with the momentum information leads to partcile species identification.

Figure 5.8 shows the hit distribution from the time of flight detectors in $(p \times q, \beta^{-1})$ coordinates. The different particle species are clearly separated especially at low momentum ($p < 1.5 GeV/c$). The bands of hits have a non-zero width at a certain momentum, leading to overlapping between species

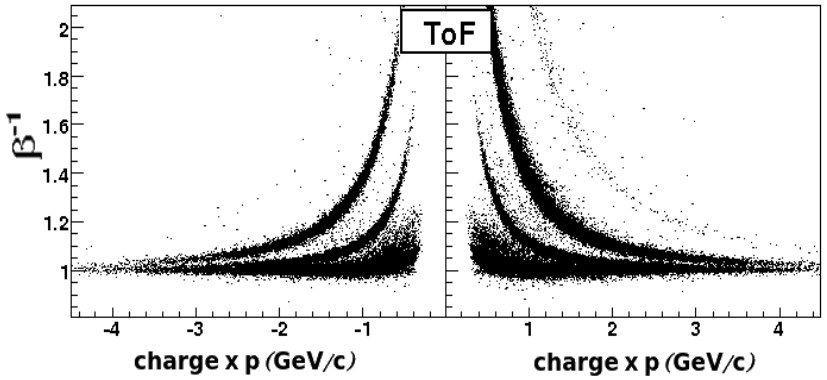


Figure 5.8: Inverse velocity ($\beta^{-1}$) as a function of momentum magnitude × charge in ToF.

at increasing momentum. This is due to uncertainties in flight time, $t_{TOF}$, momentum and trajectory length, $L$.

Instead of $\beta^{-1}$, we use cuts on mass squared $m^2$ to separate charged particles as a function of momentum, because of the independence of the expected $m^2$ on momentum. $m^2$ is obtained experimentaly as:

$$m^2 = p^2(\frac{1}{\beta^2} - 1) \tag{5.3}$$

Where $\beta = L/t_{TOF}$

For di-muon analysis we have used the ToF detector along with the MUCH detector as shown in figure 5.9. Main purpose of including the detector is to identify the background and signal particles which are left over after MUCH hadron absorbers. Figure 5.10a shows the ($m^2$, $p$) scatter plots of ToF used after MUCH detector. Hit distribution from the plots clearly distinguishes contributions from kaons and pions to the background along with proton distribution. The hit distribution of muons from $\omega$ meson is plotted in the left panel of figure 5.10a. After putting appropriat cut on $p$ or $m^2$ one can reject more background than signal. Two parameters ($m^2$, $p$) have been used in the form of a curve to eliminate most of the background with minimal loss to the signal, e.g. reject particle if $m^2 - 0.004 \times p > -0.0118$. After cutting the background using the time of flight information as mentioned above, S/B ratio has been improved as shown in figure 5.10b, where ToF

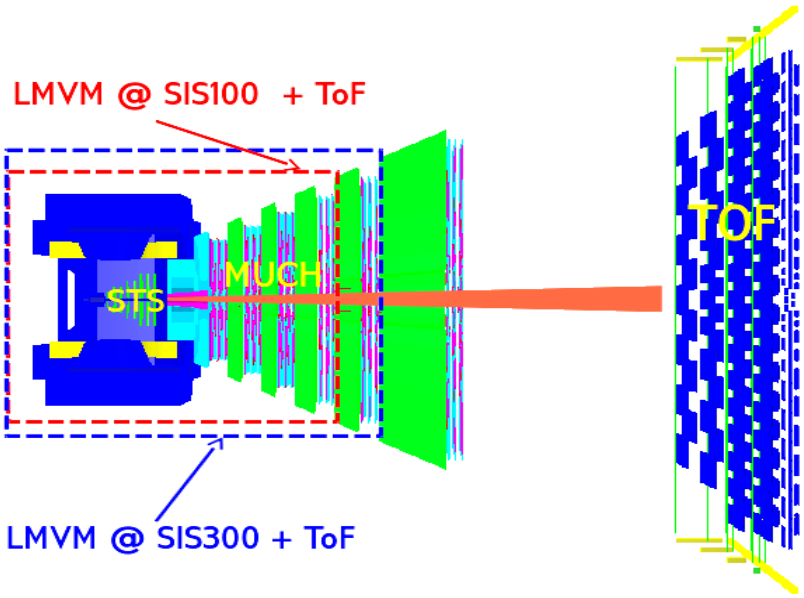


Figure 5.9: Time of flight detector with much detector set-up. For SIS100, last two absorbers are not used for low mass vector meson and for SIS300 last absorber is not used. Last absorber is used for *charmonium* analysis.

results have been superimposed over with out ToF results for comparison. Even though there is a considerable loss in the signal, almost two fold, but with better S/B ratio loss can be compensated by allowing detector a more time for data-taking for enough signal statistics.

## 5.4 Combinatorial Background/Signal

Combinatorial background to singal ratio (B/S) is very important in the invariant mass window 0.5 to 0.6 GeV/$c^2$ of hadronic cocktail because of the following reasons:

- This point is free from prejudices on any excess as there is no 'bootstrap' effect. Hence the region is most sensitive one.
- There is an unambiguos scaling between experiments with B/S $\propto$ $dN_{ch}/dy$

Table 5.4 shows B/S at 0.5-0.6 (GeV/$c^2$) of hadronic cocktail obtained by different experiments and from simulations for some experiments like CBM.

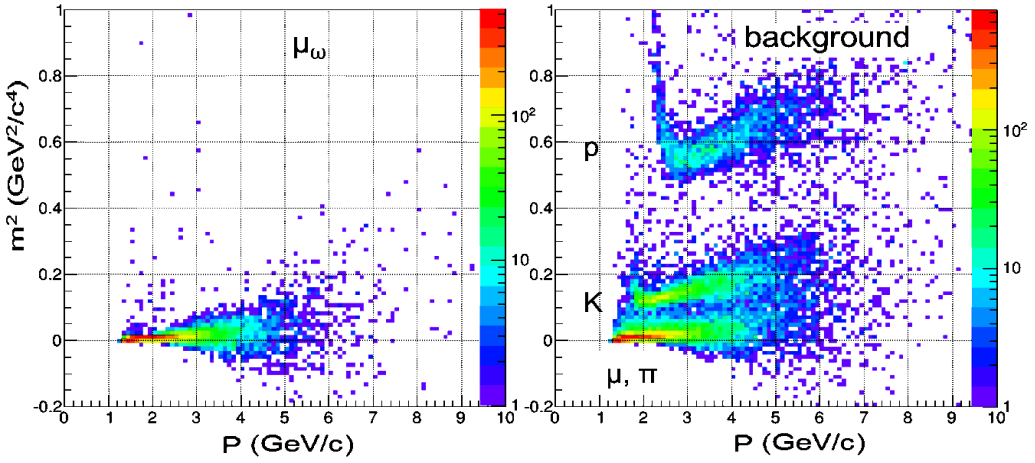


(a) TOF Hits

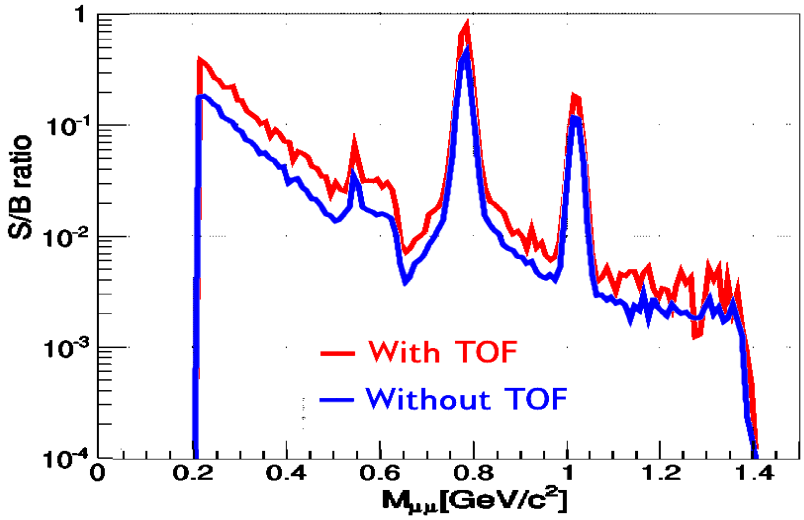


(b) S/B Ratio

Figure 5.10: (a) Time of flight hits for signal muons (left panel) and hits from particles constituting background (right). (b) S/B ratio of two configurations, with and with-out TOF.

CBM is expected to have better B/S value using the muon detector at SIS300 as well as SIS100.

| **Experiment** | **Centrality** | **Lepton flavor** | **B/S (exp./simu.)** | **B/S rescalled to $dN_{ch}/dy$** |
|---|---|---|---|---|
| HADES-SIS100 | semi | $e^-e^+$ | 20 | 60 |
| CERES DR | semi | $e^-e^+$ | 80 | 100 |
| CERES SR/TPC | central | $e^-e^+$ | 110 | 100 |
| PHENIX with HBD | central | $e^-e^+$ | 250 | 100 |
| PHENIX w/o HBD | central | $e^-e^+$ | 1300 | 600 |
| STAR | central | $e^-e^+$ | 400 | 200 |
| ALICE Upg. ITS | central | $e^-e^+$ | 1200 | 200 |
| CBM-SIS100 | central | $e^-e^+$ | 80 | 100 |
| CBM-SIS300 | central | $e^-e^+$ | 100 | 100 |
| NA60 (ln-ln) | semi | $\mu^-\mu^+$ | 35 | 80 |
| NA60 -like(20 AGeV) | central | $\mu^-\mu^+$ | 90 | 110 |
| CBM -SIS300 (5 stations) | central | $\mu^-\mu^+$ | 30 | 30 |
| CBM -SIS300 (6 stations) (NA60-like Accep.) | central | $\mu^-\mu^+$ | 20 | 20 |
| CBM -SIS100 (4 stations) | central | $\mu^-\mu^+$ | 50 | 50 |

Table 5.4: combinatorial background/signal in dilepton experiments with reference to masses of 0.5-0.6 ($GeV/c^2$) from the hadronic cocktail

## 5.5 Detection of $J/\psi$ at SIS300

The measurement of $J/\psi$ mesons is favored by the full absorber technique as the decay muons from charmonium exhibit harder momentum spectra as compared to those from $\rho^0$ or $\omega$ mesons, and, hence, are much less absorbed. The invariant mass spectra of $J/\psi$ after applying cuts have been superposed in Fig. 5.11a on the background for central Au + Au collisions at 25 AGeV. The $J/\psi$ peak is clearly visible over the combinatorial background. The efficiency, S/B and the mass resolution of $J/\psi$ are 8.2%, 0.94 and 29.6 MeV respectively.

The significance of the peak is 32.6. The corresponding acceptance plot is shown in the right panel of Fig. 5.11b illustrating that the majority of the phase-space is covered. The composition of the reconstructed background tracks per event for $J/\psi$ mesons from central Au + Au collisions at 25 AGeV shows that background is completely dominated by muons from weak decays of pions and kaons. The resulting background pair multiplicity would be

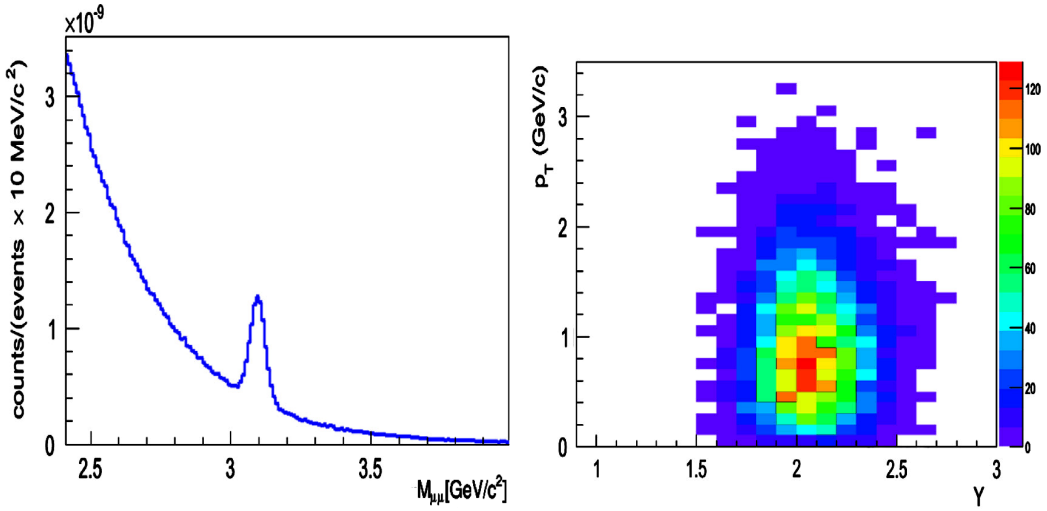


(a) Reconstructed dimuon spectra arround $J/\psi$

(b) Acceptance of $J/\psi$

Figure 5.11: (a) Reconstructed invariant dimuon mass distribution around 3 GeV/c$^2$. (b) Acceptance for $J\psi$ mesons as function of transverse momentum and rapidity.

$\approx 2.5E{-}5$ in minimum bias collisions making it possible to run at reaction rates of 10 MHz using a trigger on 2 tracks in the last detector station.

## 5.6 Summary

In last two chapters (4 & 5), discussion has been made on the design of a novel muon detection system based on segmented and instrumented absorbers as it will be built for the CBM experiment at FAIR. In this experiment, the muon system is located behind a silicon tracking system that provides particle tracks and momenta. The design goal was to identify muon candidates over a wide range of momenta. The layout of the muon detector system has been studied with simulations of central Au + Au collisions at $E_{lab}$ 25 AGeV with respect to acceptance, efficiency, and signal-to-background (S/B) ratio. Both for low mass vector mesons and $J/\psi$ mesons, the phase-space acceptances cover the midrapidity. For $\omega$ mesons emitted in central Au + Au collisions the S/B ratio is about 0.5 and the overall reconstruction efficiency is of the order of 1% at 25 AGeV beam energy. For $J/\psi$ mesons from central Au+Au

collisions at 25 AGeV the overall reconstruction efficiency is 8.2% and the S/B ratio is close to unity. It should be mentioned that, even though in the present case, the performance of the system has been shown for the CBM experiment, the concept of this detector setup could be applied to any such experiment on high energy heavy ion collisions at similar energy range.

# Chapter 6

# PHYSICS AT FAIR

## 6.1 FLUCTUATION

In high energy heavy ion collisions studied at RHIC and LHC, the conclusion so far is that a high temperature, low density partonic medium has been formed [95, 96]. As per Lattice simulations, the corresponding transition from hadronic to partonic phase is believed to be a cross-over [97]. Presumably due to continuous nature of the transition at RHIC and LHC, no 'smoking gun' signal to the phase transition has been observed. However, among the myriads of proposed observables, one that is believed to give unambiguous signal to the interesting phenomenon like phase transition or critical point is the event by event fluctuations of the conserved quantities [98].

In these collisions, the statistical models can explain the global properties of particle production reasonably well. In the context of such a picture, fluctuations of conserved quantities, which could be connected to the susceptibility, meaning the response to an external influence, are sensitive to the above mentioned phenomena. At $T_c$, the phase transition temperature, the derivatives of free energy diverge inducing fluctuations to show clear discontinuities. For a $2^{nd}$ order phase transition, for example, the fluctuation reduces drastically if matter freezes out at $T_c$ [99]. On the other hand, for a first order phase transition, the fluctuation increases sharply due to droplet

formation [100]. This variable has been said to thus classify the order of phase transition.

Experimentally, a variable (e.g. net-charge) of interest is measured event by event and the moments of the distribution of the variable concerned are the measures of its fluctuations. The quantity of interest in the context of fluctuation measurement depends on its sensitivity to the phenomena of interest. The range of quantities for which fluctuations have been measured at SPS, RHIC and LHC include multiplicities of produced particles, ratios of yields, total measured energy (or $E_T$), particle-averaged transverse momentum. Among the observables used in these measurements, prominent ones include $\Phi_q$ by NA49 [101], $\nu_{\pm,dyn}$ by STAR [102] and $\nu$(Q) as well as $\nu_{\pm,dyn}$ used by PHENIX [103]. Even though the observables are constructed differently, a common framework has however been made to relate all these observables [104, 105].

One common complexity associated with the fluctuation measurement in high energy heavy ion collisions is to construct a variable free from effects like efficiency, acceptance, impact parameter fluctuations among others. One approach to eliminate the impact parameter fluctuation, commonly known as volume fluctuation is to take the ratio of event by event yields of two types of particles e.g., K/$\pi$, p/$\pi$. Fluctuation of K/$\pi$ ratio and its charge dependence are of particular interest as they represent the fluctuations of strangeness production. The $\sqrt{s}$ dependence of K/$\pi$ at mid-rapidity measured at AGS and SPS energies shows a "horn"-like structure at $\sqrt{s} \approx 7$ GeV [106]. This interesting structure has been explained by invoking a QGP-based model that enhances the strangeness significantly at the point of transition. Measurements have also been performed of the event by event fluctuation of K/$\pi$ ratio and their charge dependence at SPS, RHIC top energy and RHIC beam energy scan (BES). While in SPS data we see a sharp fall of fluctuation with $\sqrt{s}$ before saturation [106, 107], the RHIC BES does not show any such trend at similar $\sqrt{s}$ [108].

It should be mentioned that associating a physical phenomenon like phase transition, critical point with the measured fluctuations is relevant for a thermalized system, in which fluctuation of conserved quantities(Q) is related to

susceptibility via $< \delta Q_i \delta Q_j > = \mathrm{VT}\ \chi_{i,j}$. Results of statistical simulation of QCD on lattice showed that higher order moments like skewness and kurtosis are having better sensitivity to the critical point due to a higher power dependence on correlation length ($\xi$) [109, 110]. The dependence of skewness (S) goes as $\xi^{4.5}$ and for kurtosis ($k$) it goes as $\xi^7$. At RHIC, variables like $\kappa\sigma^2$ and S$\sigma$ have been derived for net-proton and net-charge measured at different $\sqrt{s_{NN}}$. Using these variables, data could be compared directly with the lattice results[111].

Experimentally, fluctuations are measured at final freeze-out and depending on the time of origin of the phenomenon of interest, it might have propagated from the interesting region over the period of evolution through the processes like particle production, equilibration till freeze-out. If for example, a transition takes place at the pre-equilibrium stage leading to a large fluctuation at that moment, the system will then evolve till complete freeze-out of all particles and by that time the fluctuations might get modified. No significant works have been done to study the propagation of fluctuation initiated at the pre-equilibrium phase. Recently [112], investigations have been made to study the propagation of a point like disturbance initiated at 1 fm/c till freeze-out. Detailed hydrodynamical calculation shows that the disturbance results in an azimuthal distribution which could be explained to be a convolution of various flow components e.g. $v_2$, $v_3$, $v_4$.

For heavy-ion collisions at relatively lower energy, likely to be accessible at FAIR, as per the transport model calculations, a net-baryon density of the order of 1.5/fm$^3$ is likely to be produced for a very short period during the overlap of the nuclei. At such a high density, the collision zone might transform into a partonic medium which will eventually equilibrate and then convert into hadrons. The extremely dense region might result in large event by event fluctuations of specific quantities as the density might also fluctuate event by event. It will be useful to study the propagation of these fluctuations in terms of their survival at detection.

In this work, we have used UrQMD 3.3 version to study the space-time evolution of the fluctuations in Au+Au collisions at $E_{lab}$ ranging from 10 AGeV to 90 AGeV. Two modes of UrQMD have been used, one with hy-

dro evolution (known as hybrid model) included and another without the inclusion of hydro expansion. We have studied the correlated production of particles by measuring the event by event ratio of particle yields. This work does not include the study of the moments of the azimuthal distributions as measures of fluctuation.

The document is organized as follows, in section-6.1.1, we give a brief introduction to UrQMD. We discuss the methodology of this analysis and the descriptions of the variables used in this analysis in section-6.1.2. In the section-6.2.2, we present results of the time evolution of fluctuations of the ratio of kaon and pion multiplicities ($K/\pi$) and of the ratio of total positive and negative charges ($Q^+/Q^-$). We have also extracted the results for those fluctuations at freeze-out and in presence of hydrodynamical expansion. In section-6.1.3, we have discussed the time evolution of the net-proton distributions using the higher order moments. The work has been summarized in section-6.1.4.

### 6.1.1 UrQMD Hybrid version

UrQMD model is being used widely in describing the results of high energy heavy-ion collisions. The initial version of the model (hadronic version) was based on the use of transportation of hadrons with the implementation of various intermediate phenomena. The model includes transportation of various degrees of freedom (e.g. baryons and mesons) and the production of new particles and their interactions. It treats the production of particles via fragmentation of strings made of valence quarks from the original colliding hadrons [113, 114, 115]. The model did not have any equilibration implemented and therefore represents the non-equilibrated mode of transport. The final hadrons might be the decay products of hadronic resonances formed during the transportation. It should be noted that no phase transition could be implemented in this form of the model, which has found wide ranging applications in explaining the data like particle multiplicity, their species dependence, energy flow, azimuthal distributions among others. Various properties of the medium like net-baryon density could be calculated

during the transportation. As the model implements only the hadronic form of the medium, it has been used at several places to represent the hadronic reference. The model has been used to explain data from a wide range of collision energy i.e. from SPS to RHIC.

In the 'hybrid' version of UrQMD, the transportation of hadronic medium is stopped and hydrodynamical flow is set in [116, 117, 118]. The equation of state represents the type of medium under the hydrodynamical expansion. The time after which hydrodynamical flow sets in could be an input parameter but is set as default to be the time of crossing of two Lorentz-contracted nuclei via,

$$t_{start} = \frac{2R}{\sqrt{\gamma^2 - 1}}$$

After the initial pre-equilibrium stage of UrQMD, the subsequent hydrodynamic evolution is performed using the SHASTA algorithm [119, 120]. In this algorithm, cells are formed with specific thermodynamic parameters to implement the hydro transport. There are provisions of using different types of equations of state e.g., hadronic EOS which does not have any phase transition and the chiral EOS with the phase transition built in. In the 'hybrid' model, the hydrodynamic evolution is stopped after the energy density reaches below a given threshold as compared to the ground state energy density (e.g. $\sim$ 730 $MeV/fm^3$). Finally particles are formed by using the Cooper-Frye equation on an isochronous hyper-surface of the fields under hydrodynamic evolution. The hadrons thus formed might interact again using the hadron cascade before being detected. It has been shown that the model could be used over a wide range of collision energy i.e. $E_{lab}$ of 1 AGeV to 160 AGeV and then at RHIC top energy [121].

### 6.1.2 Methodology

The transport model UrQMD has been used to produce particles at different time slices after the collision. In this work, 5 million events have been generated using the default version of UrQMD at each energy studied. For

UrQMD with hydro, the number of events used is 0.25 M at each energy and at each EOS. The particle yields at different time bins are analyzed to study the time evolution of the event by event fluctuations using the measures discussed below. In the first part of the analysis studying fluctuations of K/$\pi$ and $Q^+/Q^-$, particles of all $p_T$ and in the pseudo-rapidity region of $\pm$ 1 around mid-rapidity are selected. For higher moment analysis of net proton, we have used 8 M events of UrQMD default version taking particles of similar acceptance as of STAR ($\eta$ cut of $\pm$ 0.5 and $p_T$ region of 0.4 to 0.8). Particles are said to be finally frozen out and streams freely to the detector at 100 fm/c after the start of the collision.

The present work is focused on nuclear collisions at FAIR energy range producing matters of high net-baryon density. As the time progresses, net-baryon density decreases, it will therefore be useful to study if the fluctuations present at the initial time of collision remain unaltered with time. In general the procedure that is adopted in such a study is to introduce a fluctuation from outside to study its propagation with time. In this study however, we refrain from doing this, as the procedure of introduction of an external source of fluctuation is debatable and vary from one physical process to another. We have however studied the fluctuation as it comes in an expanding medium as given by the transport model.

In this work, following studies have been performed: (a) evolution of fluctuations represented by the measures discussed below at time bins of 0.5 fm/c starting from the time of collision up to 30 fm/c (b) the effect of change of equation of state has been studied by comparing the fluctuations of the quantities concerned at freeze-out for three cases, pure transport model without the use of hydrodynamical evolution and then with hydro evolution using two equations of state.

We discuss below the construction of the observables used as measures of fluctuations in this analysis. The aim of the construction of specialized variables is to eliminate fluctuations from trivial effects like statistical fluctuation, volume fluctuations among others. Depending on the type of observable being studied, these effects might be different. For various ratio fluctuation studies, we have used a variable known as $\nu_{dyn}$, that is being used extensively

in data analysis and is said to a robust observable for the study of ratio fluctuations. $\nu_{dyn}$ was originally introduced to study the net-charge fluctuations [122, 102]. The $\nu_{dyn}$ in its final form is given by the equation below, where m and n represent multiplicities of two species.

$$\nu_{dyn} = \frac{< m(m-1) >}{< m >^2} + \frac{< n(n-1) >}{< n >^2} - 2\frac{< mn >}{< m >< n >} \tag{6.1}$$

To describe the dynamical fluctuation in $K/\pi$ ratio, we can write

$$\nu_{dyn,K/\pi} = \frac{< N_k(N_k-1) >}{< N_k >^2} + \frac{< N_\pi(N_\pi-1) >}{< N_\pi >^2} - 2\frac{< N_K N_\pi >}{< N_K >< N_\pi >}$$

where $N_K$ and $N_\pi$ are the event-wise number of kaons and pions in a given acceptance, respectively. Similar formula can be constructed for $Q^+/Q^-$, $p/\pi$, $K/p$ and other ratios. By definition, $\nu_{dyn}$=0 for the case of a Poisson distribution of both the yields. It is also largely independent of the detector acceptance and efficiency in the accepted phase space[102, 123].

### 6.1.3 Results

**Time evolution of net-baryon density, particle multiplicity and ratio fluctuations**

Fig. 6.1 shows the time evolution of the net-baryon density at three different incident energies. The flat top depends on the incident energy being longer-lived at lower energy. The density reaches 10 times the nuclear matter density and is expected to satisfy the criterion for a transition to a non-hadronic state. The Fig. 6.1, which shows the variation of net baryon density with time at different collision energies, demonstrates the importance of heavy-ion collisions at FAIR energies that generate high density matter. As expected from the time required for two nuclei to pass each other, the peak density is longer lived at lower beam energies. It will therefore be very interesting to study the variation of particle multiplicity with time and its correlation with the net-baryon density. It should be mentioned that, the time of reaching the peak net-baryon density might not coincide with the equilibration

time especially at lower collision energy. A high density matter undergoing a transition to a partonic state at the highest net-baryon density might undergo re-scattering to reach equilibration at a later time. The signals like fluctuation of a specific quantity might then undergo evolution to reach the freeze-out stage via equilibration. The main aim of this work is to study this effect.

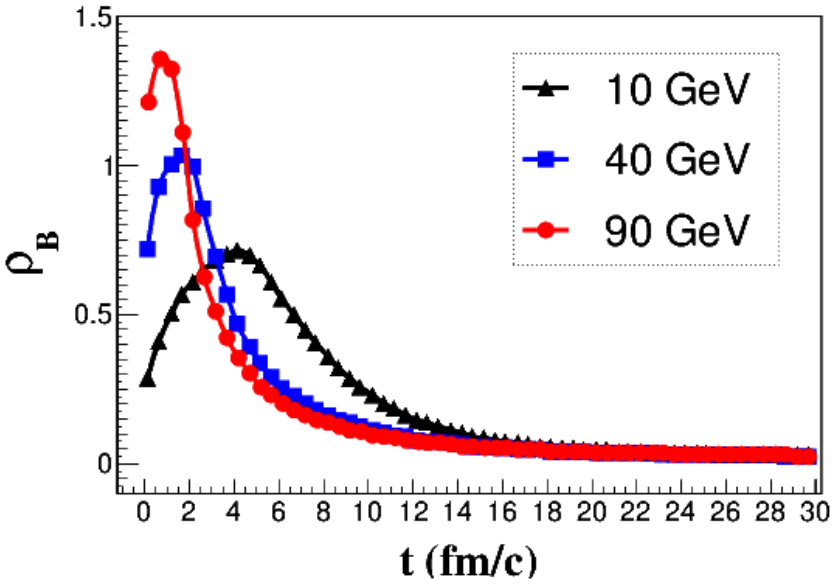


Figure 6.1: Evolution of net-baryon density with time elapsed after collision

Fig. 6.2 and the Fig. 6.3 show the variation of average multiplicities with time for pions and kaons respectively at three different beam energies. It is clearly evident from the figures that for two types of particles, the multiplicities at different times elapsed after collision show peak structures at around the highest net-baryon density, the time of complete overlap of two nuclei and subsequently rises towards the finally detected multiplicity. At 10 AGeV, the multiplicity increases slowly to reach near saturation and the initial peak structure is not prominent. At that energy, the density also shows a smoother behavior.

The individual particle multiplicities go through peaks and valleys, the ratio of total multiplicities of kaon and pion shows a peak around the overlap region saturating at later times as seen in Fig 6.4.

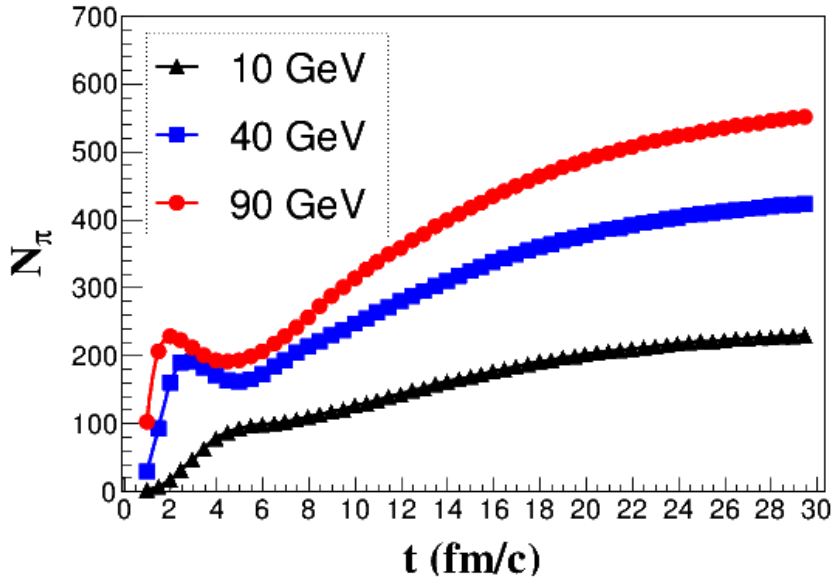


Figure 6.2: Mean multiplicities of pion with elapsed time at different collision energies

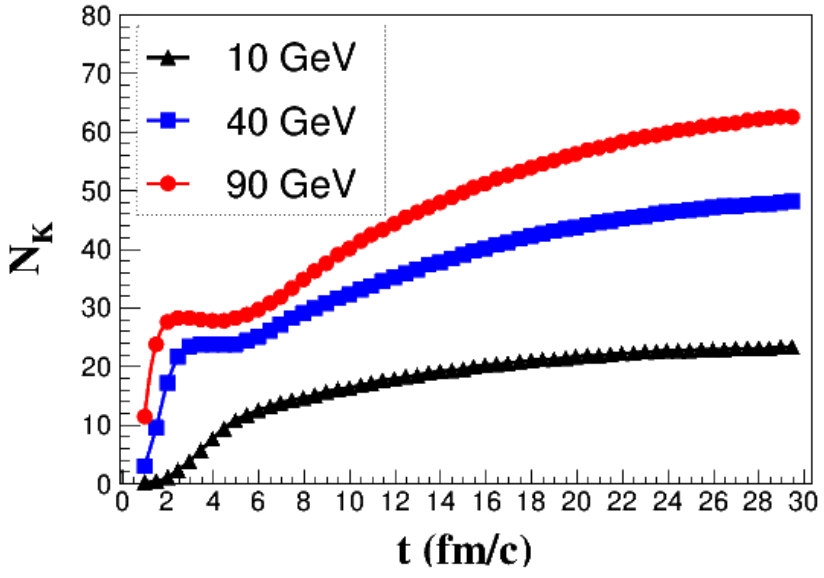


Figure 6.3: Mean multiplicities of kaon with elapsed time at different collision energies

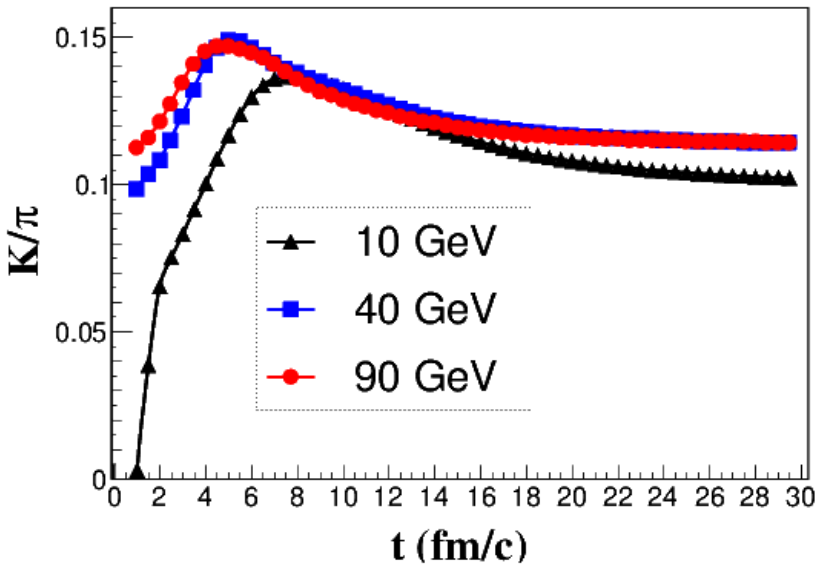


Figure 6.4: Evolution of $K/\pi$ ratio with time at different collision energies

The time dependence of the fluctuation measure of the ratios i.e. $\nu_{dyn}$ are shown in Fig. 6.5 and Fig. 6.6 for Au + Au collisions at three different energies for K/$\pi$ and $Q^+/Q^-$ respectively.

In case of both kinds of ratio, we see that $\nu_{dyn}$ starts with a large absolute value and subsequently reduces to saturated values. The reduction is faster for the case of 10 AGeV in comparison to the higher collision energies. As the $\nu_{dyn}$ for K/$\pi$ essentially represents the fluctuation in strangeness production, higher fluctuation at lower beam energy represents the fact that the multiple interaction, the prominent mechanism of production of strangeness at lower energy also leads to larger fluctuations. For the case of $Q^+/Q^-$, the initial charge conservation have been the cause of the correlated production of oppositely charged particles leading to a negative $\nu_{dyn}$ and then the correlation term reduces with the production of more charged particles and it reaches a value close to zero.

Interestingly, at lower collision energy (10 AGeV), the reduction of fluctuation of K/$\pi$ is faster starting with a higher $\nu_{dyn}$ at the beginning and it crosses the values for higher beam energies at detection. In both cases, the initial fluctuations get diluted with time.

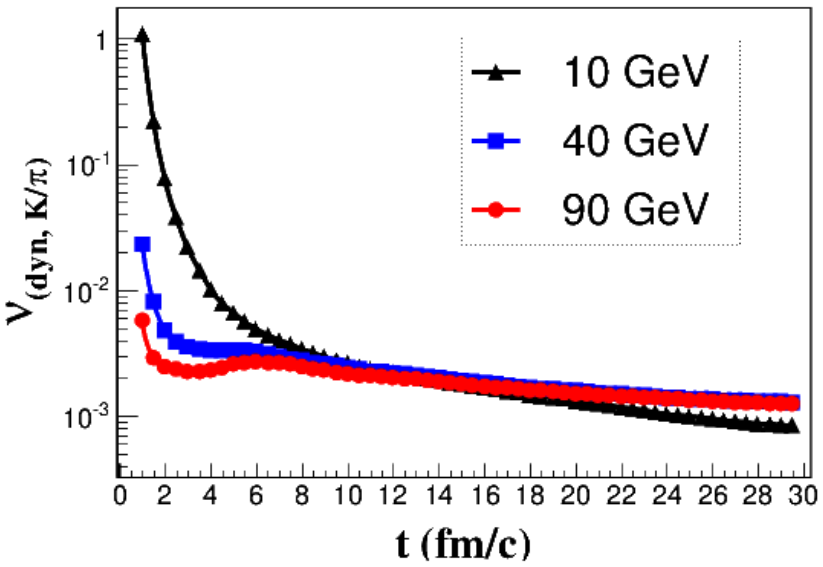


Figure 6.5: Time evolution of $\nu_{dyn}$ of $K/\pi$ at different collision energies

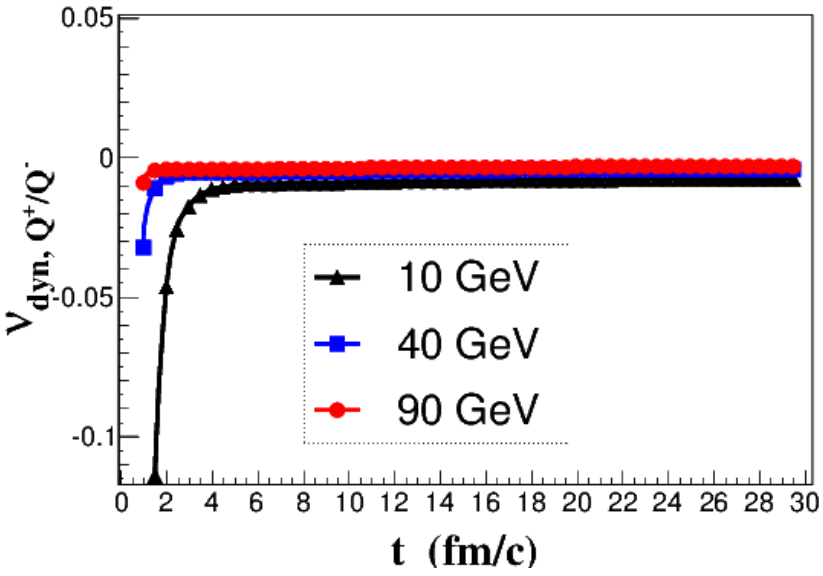


Figure 6.6: Time evolution of $\nu_{dyn}$ of $Q^+/Q^-$ at different collision energies

### Energy dependence of fluctuations at freeze-out

The Figure 6.7 and Fig. 6.8 show the energy dependence of multiplicities of kaons and pions and of their ratio respectively at freeze-out.

Fig. 6.9 shows the energy dependence of $\nu_{dyn}$ of $K/\pi$ at freeze-out. The

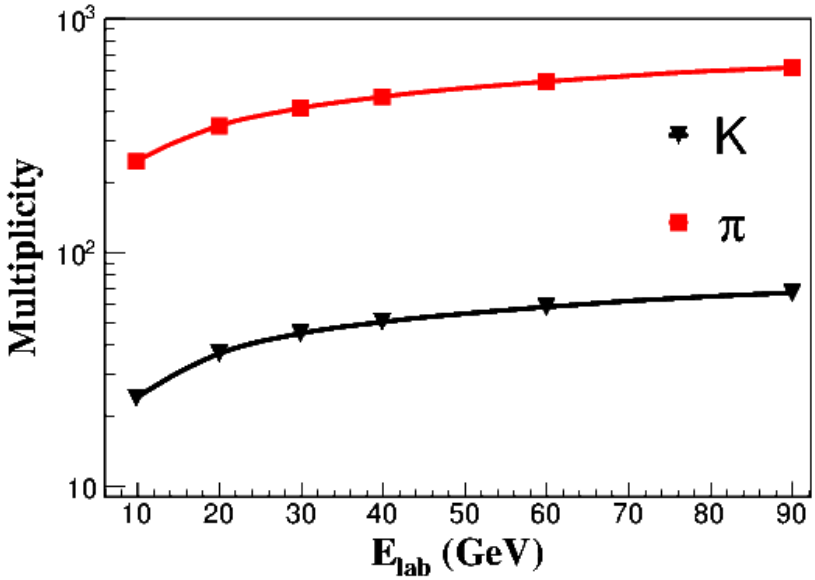


Figure 6.7: Beam energy dependence of kaon and pion multiplicities at freeze-out

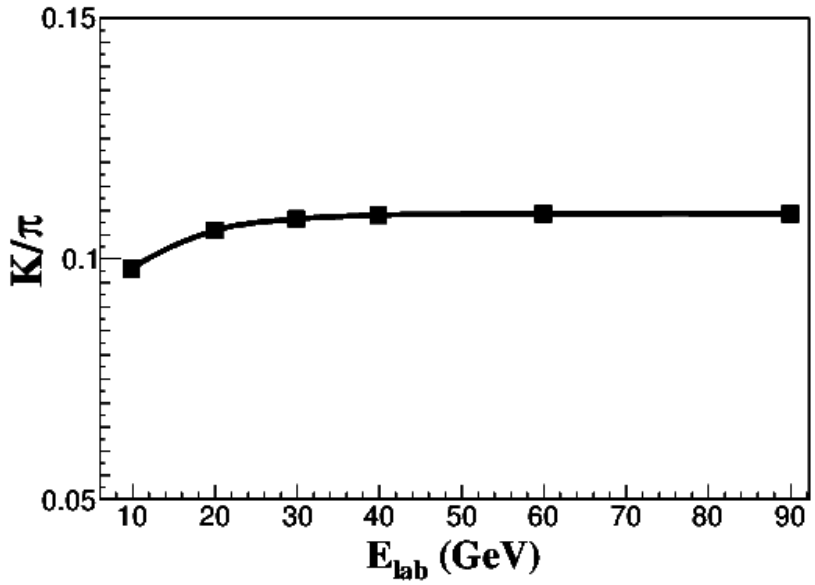


Figure 6.8: Beam energy dependence of the ratio of kaon to pion multiplicities at freeze-out

trend can be seen at the end points of Fig. 6.5 and 6.6 as well. It is positive for K/$\pi$ showing the dilution of the correlation between kaons and pions at later times after collision. We selected 1% events of highest net-baryon density

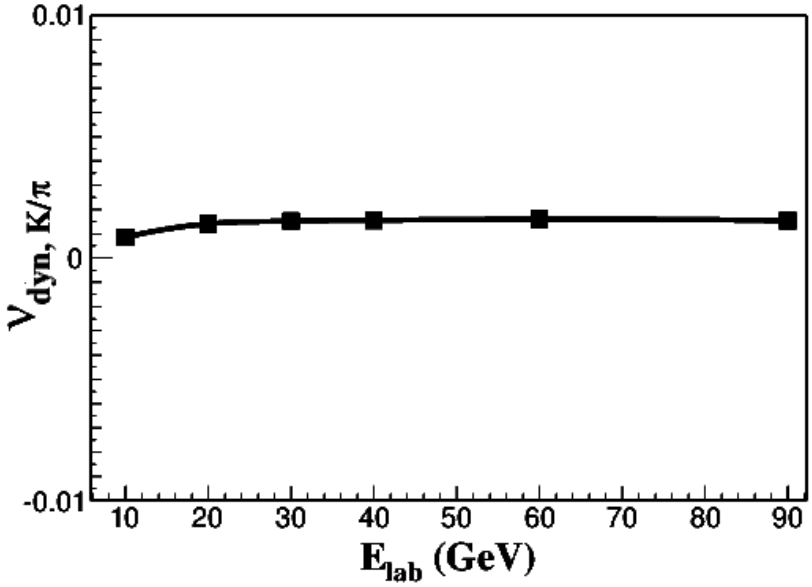


Figure 6.9: Beam energy dependence of $\nu_{dyn}$ for $K/\pi$ at freeze-out

and compared $\nu_{dyn}$ for K/$\pi$ and $Q^+/Q^-$ with the bulk of events. These top 1% events do not show significant differences in the time evolution of the fluctuations compared to the value averaged over all events.

**Effect of hydrodynamical evolution on fluctuation**

Recently the role of hydrodynamic evolution to the initial fluctuation present primarily at the geometrical overlap of the colliding nuclei are being discussed extensively. In those discussions, inferences have been drawn on the signatures of azimuthal distributions of the produced hadrons that have been reflected by the higher harmonics of azimuthal distributions. In the present discussions, to study the effect of hydro on the overall freeze-out particle, the hydro evolution has been switched on at times of 5.56, 3.94, 3.22, 2.79, 2.28, 1.86 (fm/c) for beam energies of 10, 20, 30, 40, 60, 90 (GeV) respectively, to be followed by the evolution discussed earlier.

In Fig. 6.10 and Fig. 6.11, we have shown the energy dependence of $\nu_{dyn}$ at freeze-out for K/$\pi$ and $Q^+/Q^-$ respectively. We have calculated $\nu_{dyn}$ for three scenarios i.e., pure hadronic transport case with no hydrodynamic expansion, with hydrodynamic expansion using the "hadronic gas" equation

of state and then with the "chiral" equation of state. It is seen that at lower collision energies, fluctuation in $K/\pi$ ratio after hydro expansion with both types of equations of state are higher as compared to the pure transport results. The chiral equation of state however, shows more enhancement in fluctuation for K/$\pi$ at lower beam energies. This makes the measurement of fluctuation at lower beam energy more interesting. Whereas, there is almost no effect of EOS's seen on fluctuation in $Q^+/Q^-$ ratio in both pure and in hybrid UrQMD mode.

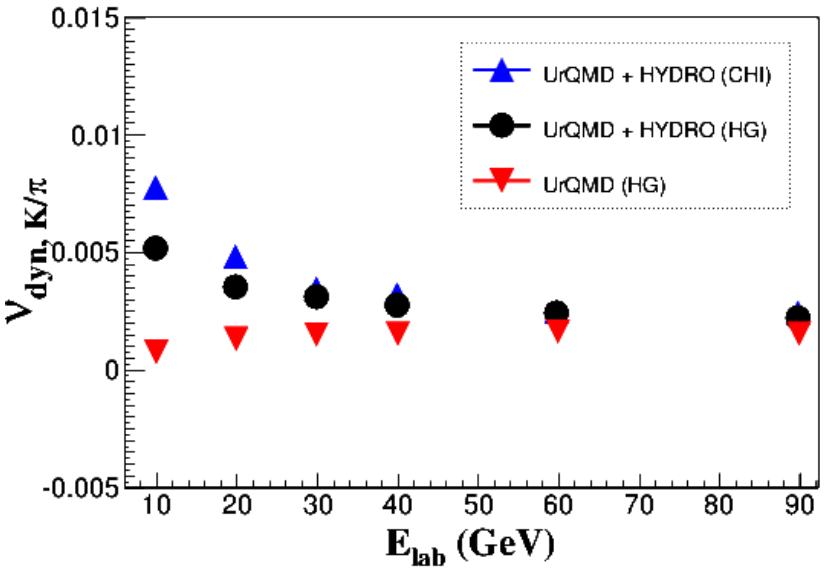


Figure 6.10: Beam energy dependence of $\nu_{dyn}$ for $K/\pi$ with pure transport and with hydro evolution using two equations of state

### Fluctuations of net-proton distributions

As mentioned earlier, measurements of the higher order moments of the conserved quantities have drawn a lot of attentions recently due to their higher sensitivity to the exotic phenomena like critical point. As a candidate of the net-baryon number, results have been presented for net-proton distributions by several experiments. We have therefore extracted the time evolution of net-proton fluctuations measured in terms of two widely used observables which represent the susceptibilities i.e., K$\sigma^2$ and S$\sigma$, where K, S and $\sigma^2$ rep-

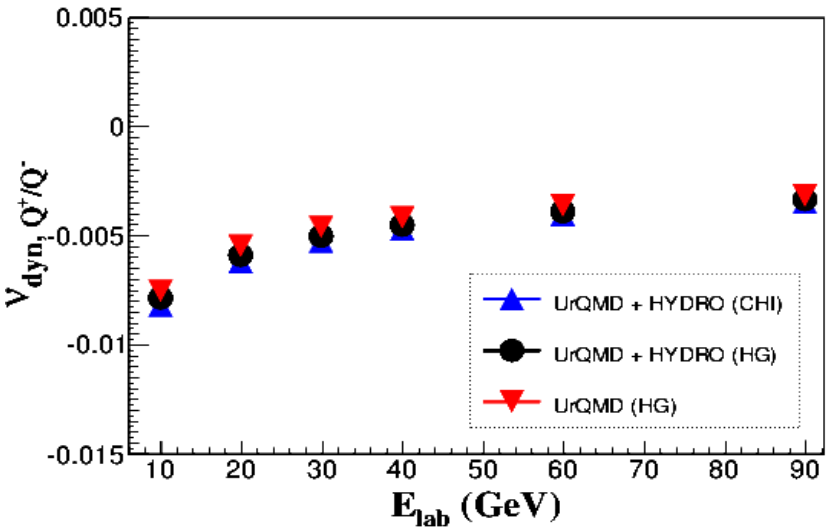


Figure 6.11: Beam energy dependence of $\nu_{dyn}$ for $Q^+/Q^-$ with pure transport and with hydro evolution using two equations of state

resent kurtosis, skewness and variance of the distributions. Here we have taken the same coverage and kinematic cuts as that of the STAR published results [111], i.e. pseudo-rapidity of 0.5 around mid-rapidity and $p_T$ in the range of 0.4 - 0.8 (GeV/c). It has been shown that these combinations of variables could be compared directly with the lattice simulation results.

In Fig. 6.12 and Fig. 6.13 we are showing the time evolution of S$\sigma$ and K$\sigma^2$ respectively at different beam energies. It is seen that $S\sigma$ is nearly flat with time except initially where it shows structure more prominent at higher energies which then grows to smooth value. K$\sigma^2$ however reduces from higher values. Moreover, K$\sigma^2$ shows structure at the time of nuclear overlap reflecting fluctuation more prominent at higher energies. It is interesting that the initial energy dependence in K$\sigma^2$ gets washed out at 30 fm/c. In the study of fluctuation, we look for a non-monotonic behavior of the fluctuation measures. In recent beam energy scan results from STAR, $\sqrt{s}$ dependence of these quantities have been measured and interesting structures are said to exist at around 19 GeV. It is evident from the present study that the values measured at freeze-out does not contain the structures which might have been present during the evolution. We therefore would like to study the energy dependence of the structures.

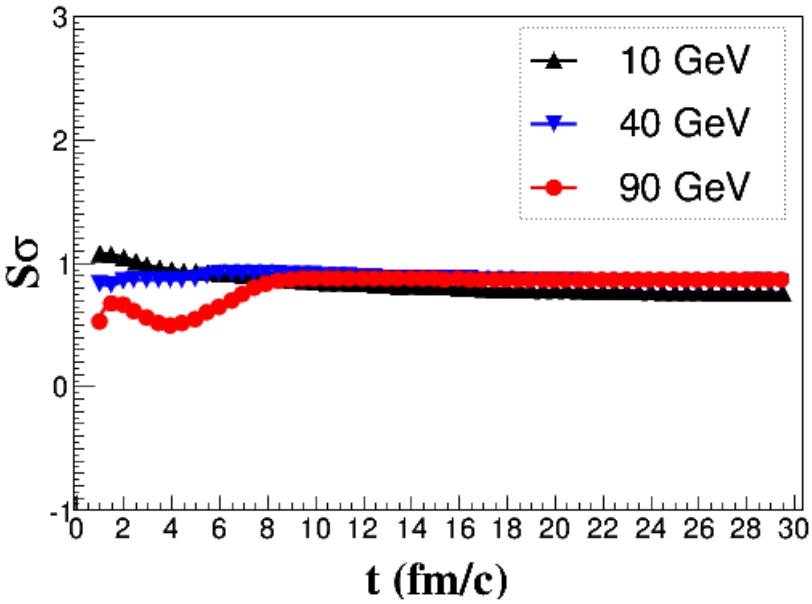


Figure 6.12: Time evolution of S$\sigma$ for net-proton at different collision energies

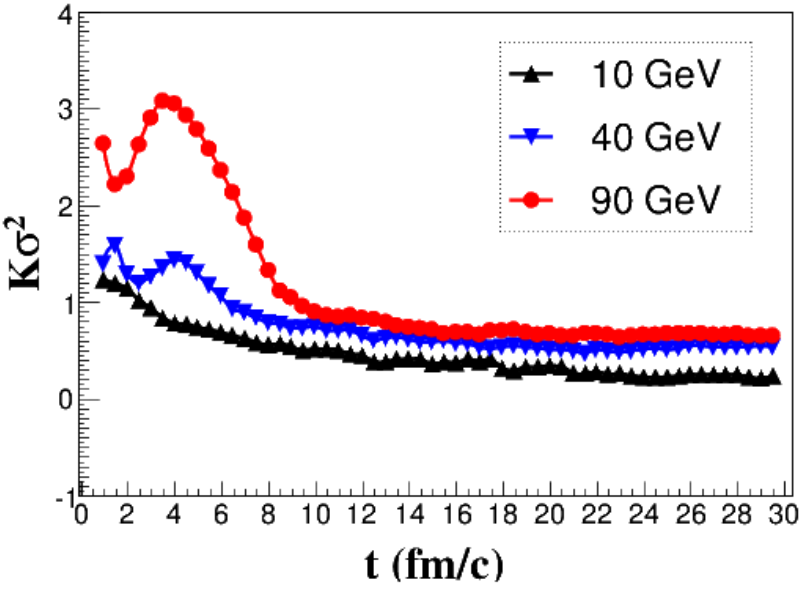


Figure 6.13: Time evolution of K$\sigma^2$ for net-proton at different collision energies

Fig. 6.14 and Fig. 6.15 are showing the energy dependence of S$\sigma$ and K$\sigma^2$ respectively at freeze-out. There is no non-monotonous dependence with $E_{lab}$ at FAIR-energy when calculated within the same coverage as of STAR. Even

though the energy dependence at detection looks flat, there were structures present at the beginning of the collision.

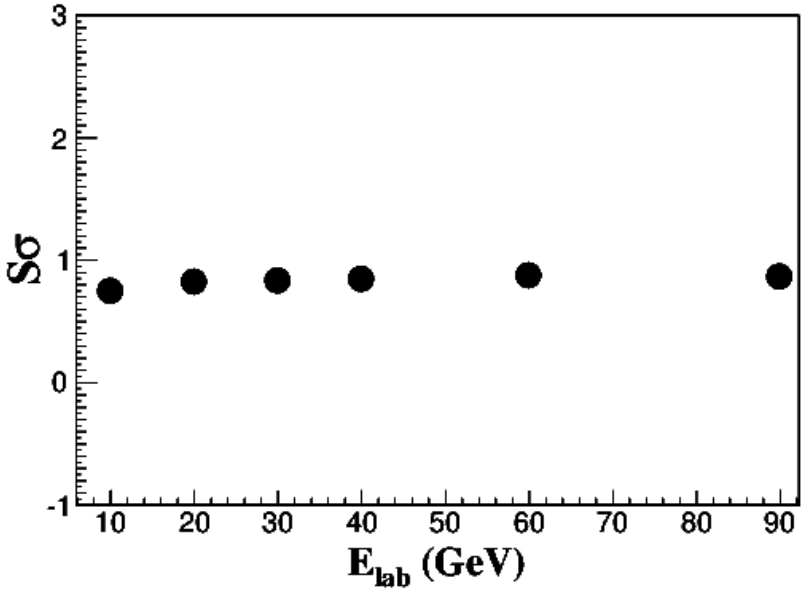


Figure 6.14: Beam energy dependence of S$\sigma$ for net-proton at freeze-out

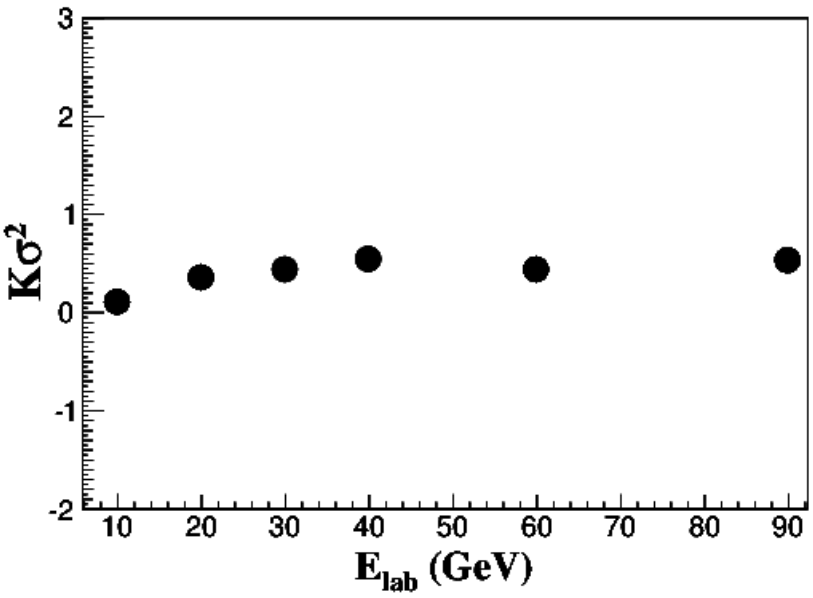


Figure 6.15: Beam energy dependence of K$\sigma^2$ for net-proton at freeze-out

### 6.1.4 Discussions

In this work, we have used UrQMD model to study the fluctuations of two important variables i.e the ratios of K/$\pi$ and $Q^+/Q^-$ and the higher order moments of net-proton. The fluctuations of these variables are being studied extensively in high energy heavy-ion collisions as they are to signify important phenomena like phase transition and the occurrence of the critical point. The results from UrQMD and other transport models have been used in the context of explaining the data from different experiments. The results from these models have been considered as reference data for finding interesting phenomena in high energy heavy ion collisions. The results from the models are conventionally obtained at final freeze-out for comparison with finally detected particles. The transport models however have the provision of providing space time history of the collision and can be used to understand the time evolution of signals till freeze-out. The fluctuations are usually discussed in literature only in the context of thermal production of particles, however, if a variable shows a large fluctuation at the pre-equilibrium stage, then it needs to be followed till freeze-out.

In the present study, we have put emphasis on the lower energy heavy-ion collisions to be available at FAIR. These collisions produce matter under very high net-baryon density. It is seen from the transport models that the net baryon density reaches maximum for a short time during the overlap of two nuclei. During this time, the particle multiplicity also reaches a peak and then slowly through the evolution reaches a near-saturated values at freeze-out. During this evolution, fluctuations at the beginning show structures which then smoothen out during the evolution. It therefore suggests that there is a considerable modification of the early fluctuation signals. From this analysis however, we might not be able to infer about the evolution of fluctuation signals that originate from an equilibrated thermal system. We have studied the effect of hydrodynamical evolution of the signals by comparing the results from transport only, hydro with hadronic EOS and chiral EOS. It is seen that at freeze-out, $\nu_{dyn}$, the measures of fluctuations of K/$\pi$ for hydro with both hadronic and chiral EOS show higher values at

lower beam energies as compared to the default version of UrQMD, with the chiral EOS being highest. However, the fluctuations with the chiral EOS shows more enhancement at lower beam energy. There is almost no effect seen on the charge ratio fluctuation in all the cases. This therefore suggests that even at freeze-out, at lower beam energy, fluctuations in K/$\pi$ might be considered to be important signals for identifying the EOS. For net-proton, fluctuation observables like S$\sigma$ and K$\sigma^2$ shows initial fluctuation, at the time of nuclear overlap, which washes out at freeze-out.

## 6.2 STRANGENESS PRODUCTION

One of the main purpose of relativistic heavy-ion collision experiments is to study the nuclear matter under extreme conditions of temperature and/or density. Under these extreme conditions, nuclear matter is expected to undergo a transition from confined hadronic medium to a free quarks and gluons medium, known as quark-gluon plasma (QGP) [124]. One of the signatures of formation of such a novel state of matter is the relative enhancement of strangeness production, measured by the ratios of their yields in nucleus-nucleus collisions in comparison to the yields in proton-proton collisions or in peripheral collisions. Main production mechanism of strangeness ($s\bar{s}$) in QGP is assumed to be through gluon-gluon fusion ($gg \rightarrow s\bar{s}$) followed by the chemical equilibration time ($\tau^{eq}_{QGP} \approx 10$ fm/c). Inside hadrons gluon density as well as energy density are lower due to the confined volume restricting such reactions [125].

Strangeness exchange reactions like $\Lambda K^- \rightarrow \Xi^-\pi^0$, $\Lambda\Lambda \rightarrow \Xi^- p$ and $\Lambda\Xi^- \rightarrow \Omega^- n$, $\Xi^- K^- \rightarrow \Omega^-\pi^-$ are one of the important production process for multi-strange hyperons as implemented in transport models [126]. Since, these multi-step strangeness processes depend on the density of the created medium, and, hence, one can use them to probe the density and the EOS of the medium. In experiments at AGS and SPS studied non-strange, singly-strange and at most doubly-strange particles up to beam energies of 30 AGeV but no $\Omega^-$ hyperons were found up to beam the energy range [127] due to low rate capability of the detectors used. In contrast, the CBM ex-

periment at FAIR is designed for unprecedented reaction rates (∼10 MHz), which will allow precision studies of multi-strange (anti-) hyperon production in heavy-ion collisions at beam energies close to their threshold [128].

Results of a systematic study of the production of multi-strange hyperons will be discussed, using different transport models, in central Au + Au collisions at 40 AGeV. The strange quark number dependence of the yields of strange particles have been fitted and then made an extrapolations at FAIR energy even for multi-strange particles. This article is arranged in the following manner: in Section-6.2.1 a brief description of the models used has been given. In Section-6.2.2, the model predictions for the production of multi-strange particles have been discussed. Finally, the findings are discussed in Section-6.2.3.

### 6.2.1 Models

In this work, two microscopic transport models like UrQMD (version 3.4 ) [84] and AMPT (version 1.26t4) [129] have been used. These models have been used extensively to explain the strangeness production from AGS to RHIC energies.

The UrQMD microscopic transport model uses string fragmentation to produce hadrons while taking into account the re-scattering of the strings and the products of their interaction. The production of particles proceeds through the meson and baryon resonance decays or string excitation and fragmentation.

In the AMPT transport model, initial spatial and momentum distribution of hard minijet partons and soft strings, which undergo re-scattering described by Zhangs parton cascade (ZPC), are obtained using HIJING model. ZPC uses two-body scattering where scattering cross-section for parton-parton scattering is obtained from pQCD along with screening mass. Produced partons or strings undergo hadronization by Lund String Fragmentation model in default mode or by Quark Coalescence model in string melting mode. The interaction of the produced hadronic matter during the transport is treated by ART. Both modes of the AMPT model, the string

melting (partonic matter) and the default mode (hadronic matter), have been used for calculating the particle yields to examine whether hyperon production is sensitive to the degrees of freedom in the collision volume.

### 6.2.2 Results

Multi-strange hyperon particle yields have been obtained in central gold-gold collisions (with b < 3 fm) at energy 40 AGeV using statistics of 1 million events. The analysis is done for the particles produced in the mid-rapidity region i.e. -0.5 < y < 0.5.

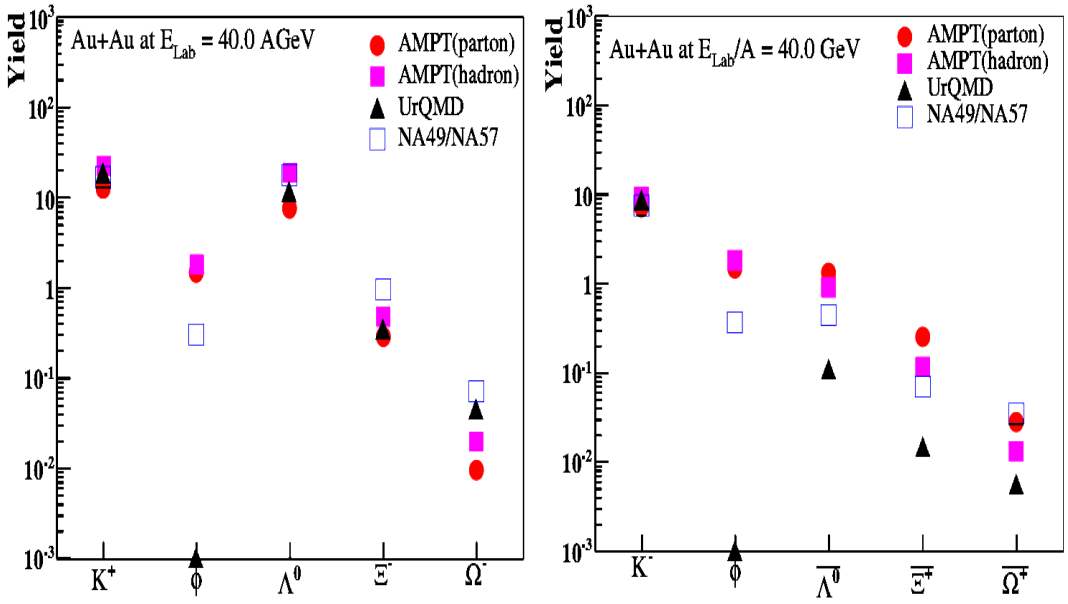


Figure 6.16: Mean multiplicities of strange particles at $E_{Lab}$ = 40 AGeV using various models. The solid symbols corresponds to model calculation and open symbol represents experimental data [130].

Figure 6.16 has been plotted to have a closer look of the strangeness content of various particles produced at top FAIR energy. Average yields of various strange particles at $E_{Lab}$ = 40 AGeV have been plotted along with the results from SPS experiment(NA49 and NA57) [130]. Figure shows that the multi-strange hyperon average yield decreases with increasing number of strange quarks. Two clearly distinct slopes are seen for the mesons and

the baryons respectively. Yield of kaons is reproduced but that of $\phi$ meson is underestimated by all models. In the baryon sector, the models underestimate the data points for $\mid s \mid \geq 2$ while all models give similar results for anti-hyperons except for $\bar{\Omega}^{+}$. The average yield measured by AMPT partonic version for $\bar{\Omega}^{+}$ nearly matches with the data

In order to understand the strange particle production mechanism, the average yields of the strange particles have been plotted with respect to the strangeness quantum number in Au + Au collisions at 40 A GeV as shown in Fig. 6.17. Interestingly all models show similar structures with a peak corresponding to strangeness quantum number -1, and the curve falls on both sides with faster fall for hyperons with positive strangeness quantum number. AMPT-partonic version shows the slower reduction in comparison to other models which shows enhanced production in multi-strange hyperons. It appears that there is an increase in yields for positive $s$ in the partonic mode, while it reduces for negative $s$ particles.

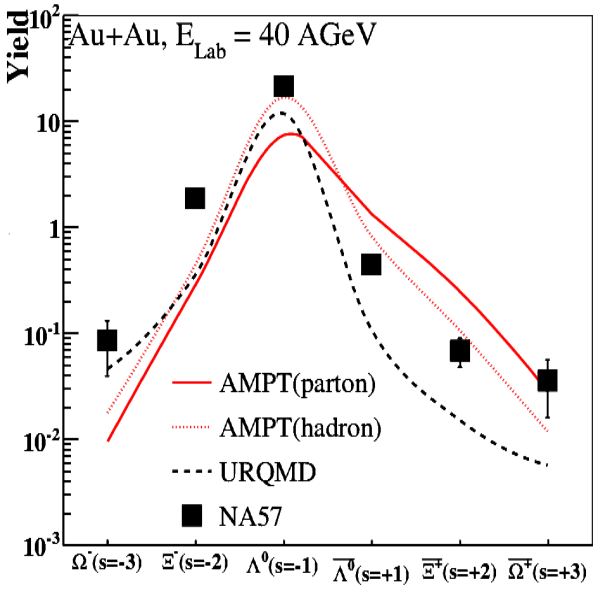


Figure 6.17: Average yields of strange hyperons with strangeness quantum number for Au + Au collisions at 40 A GeV by different models.

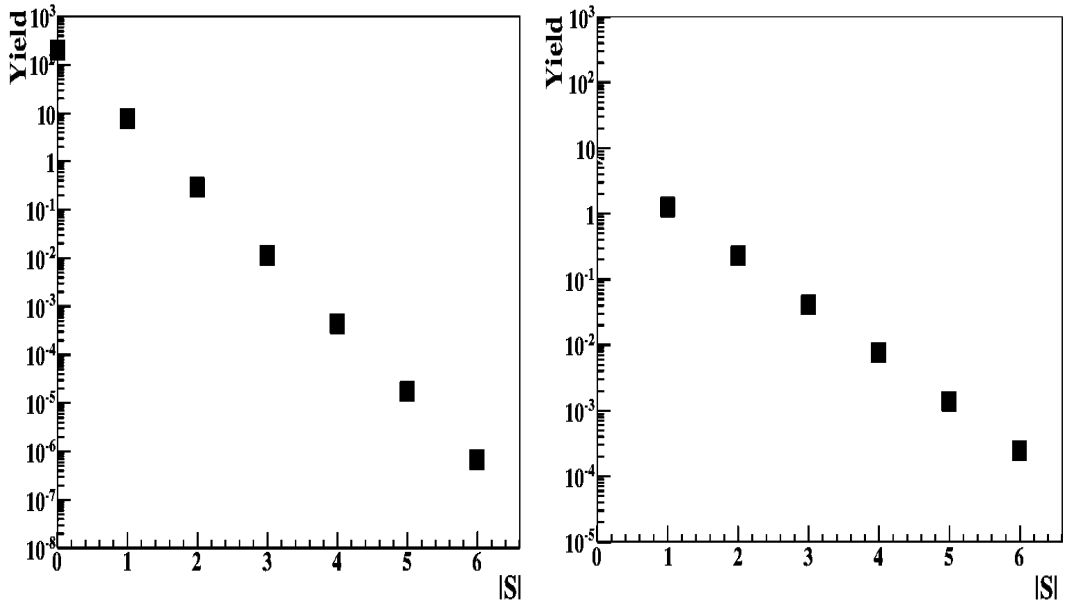


Figure 6.18: Average yields of multi-strange particles as a function of higher strange quark content. Left panel corresponds to average yields of hyperons and Right panel represents average yields of antihyperons

### 6.2.3 Conclusion

The measurement of strange particle yields is an important observable for studying the properties of the dense matter created in heavy ion collisions at FAIR energies. It has been proposed that the strange quark yields and thus, yields of strange mesons and baryons increases in a de-confined medium. The multi-strange hyperon yields could also be increased by exchange mechanism more prominently in baryon rich medium. FAIR provides the opportunities where high net baryon density medium can be created in the nuclear collisions at relatively lower energies which makes it an interesting place for studying the multi-strange production. Models like the AMPT predicts the enhanced production of multi-strange hyperons in the partonic medium in comparison to the hadronic scenario. The AMPT partonic version shows higher sensitivity to multi-strange hyperons as compared to the singly-strange particles.

In order to extrapolate the results towards the higher strange quark number particles and/or of higher mass, the dependence of yield has been fitted with strangeness shown in fig. 6.18 with polynomial functions for positive

and negative strangeness separately. It should be noted that production of particles beyond three quarks require special treatment and as per this simplistic model the yields of strange objects with six (anti-)strange quarks could be of the order of $(10^{-4})10^{-6}$. To provide the experimental verification of these predictions, detector system with high intreaction rates are required-for which the Compressed Baryonic Matter (CBM) detector system is being designed at FAIR in Darmstadt, Germany.

# Chapter 7

# Summary and Conclusion

High energy heavy ion collisions are used to create and study produced particles which have been classified using simple scheme in terms of quarks, leptons and intermediating gauge bosons in the Standard Model. Experiments are carried to test this model in all conceivable ways to discover whether something more lies beyond it. Quantum chromo-dynamics theory tries to describe the dynamics of quarks and gluons from "asymptotic-freedom" to "confinement" phase. In QCD, a state of matter consisting of asymptotically free quarks and gluon's (QGP) has been hypothesized to exist at extremely high temperature or density. This state of matter is believed to be there up to a few milliseconds after the Big Bang. Experiments like LHC at CERN is believed to have produced QGP by colliding protons with lead nuclei at high energy inside the Compact Muon Solenoid (CMS) detector. It has been shown that this new state of matter behaves like a fluid. Experiments at RHIC and LHC are exploring the de-confined QCD matter at very high temperatures and almost zero net baryon densities. There are experiments like STAR and PHENIX at RHIC, SPS at CERN, JINR at NICA which try to investigate the QCD phase diagram at high net-baryon densities and look for the critical endpoint. Due to low luminosity above mentioned experiments are constrained to look for the bulk observables which are predominantly sensitive to the late and dilute phase when most of the particles freeze out except elliptic flow. In contrast, Compressed Baryonic Matter (CBM) experiment

at FAIR (Facility for Anti-proton and Ion Research) will have high beam luminosity and fast detector system to focus on the measurement of rare and diagnostic probes of the early dense phase. This approach will help us to find signatures of partonic degrees of freedom, first order de-confinement phase transition and its critical endpoint, in-medium modifications of hadrons, and nuclear equation of state at high baryonic densities. Low mass vector mesons are considered to be the sensitive probes of in-medium modifications and chiral symmetry restoration. Whereas, charmonium suppression is considered to be good indication of QGP formation in heavy ion collisions. FAIR has proposed a muon detection system called MUCH for CBM experiment which will look for low mass vector mesons and charmonium via their di-muonic decay. Purpose of this thesis is to present the optimised and approved design of MUCH and its feasibility studies for cocktail sources at 25 AGeV energies. Moreover, results for physics issues like fluctuation and strangeness production have been provided at FAIR energy.

In chapter 1 brief introduction has been given about the QCD physics relevant to the heavy ion collisions. First the concept of confinement and asymptotic freedom is discussed and then the concept of new state of matter 'quark-gluon plasma' formation in heavy-ion collisions are introduced. Then a brief introduction of its phase-space evolution with time has been given. Next the different signatures of QGP has been discussed which have been extensively used by different experiments. Finally an idea about the different types of detectors have been given which are mostly used for the detection of variety of particles created in high energy heavy ion collisions.

In chapter 2 a general overview of the CBM experiment at FAIR has been given. The outline of the FAIR accelerator facility is presented first followed by the discussion on the different physics goals of the CBM experiment at two accelerators namely SIS100 & SIS00 and the corresponding potential observables. Then a brief account on the configuration of CBM experimental setup and each of its sub systems has been given. Chapter ends with a brief overview of tracking detector technologies to be used for the muon detection system.

The comparison of dimuon spectrum of NA60 experimental data with

theoretical models have been given in chapter 3. It has been argued that dimuon spectrum provide important information on the evolution and on the properties of the hot and dense fireball created in heavy ion collisions. Three region of the spectrum have been discussed separately. In the first region of the spectrum called low mass region an excess from the expected yield has been observed which has been associated with the modification of in-medium mass distribution of short-lived vector mesons when contribution of known sources have been subtracted at different centralities but no shift in the mass pole has been observed. In the intermediate mass region of the spectrum, when measured dilepton mass distribution is subtracted with the contribution from vector mesons, allows to extract the thermal radiation, and, hence, the temperature evolution of the fireball. We have observed that at top SPS energies, the di-muon mass distribution in the intermediate mass range is dominated by radiation from a deconfined partonic phase. In the high mass region of the spectrum, the comparison of charmonium yields measured in nucleus-nucleus with proton-nucleus collisions has showed an anomalous suppression of charmonium yeild in central collisions of heavy nuclei which could be explained by considering dissociation of charmonium due to color screening in the quark-gluon phase. This conclusive observation is one of the most convincing experimental facts hinting towards the existence of quark gluon plasma phase formation at top SPS energies. To search for the onset of in-medium mass modifications of vector mesons or for partonic contributions, a systematic beam energy scan of the dilepton yields has not been performed yet. CBM is set to scan the beam energy range from 2 to 40 AGeV where matter at the highest net-baryon densities are expected to be created in the laboratory, where no dilepton measurement has been done so far in heavy ion collisions, and which will open a new era in dilepton experiments. Plan at CBM experiment is to measure systematically both di-electrons, using RICH detector, and di-muons, using MUCH detector in place of RICH in the set-up, for p+p, p+A and A+A collisions as a function of incident beam energy and system size. High precision data of two leptonic channels of low mass vector mesons and charmonium will complement each other to provide a consistent picture on di-leptonic radiation from dense

baryonic matter. Therefore, one can say that the CBM experiment has a large discovery potential at SIS100 as well as SIS300.

In chapter 4 the approved design of MUCH (muon chamber) detector for CBM experiment has been discussed. As discussed in detail the design of a novel muon detection system based on segmented and instrumented absorbers. In this experiment, the muon system is located behind a silicon tracking system that provides particle tracks and momenta. The design goal is to identify muon candidates over a wide range of momenta. Different components like absorber material, absorber length, gaps between the absorber, type of tracking detector, type of beam-pipe and its shielding material has been optimised and the corresponding values have been quoted in this chapter. First absorber will be made of carbon and rest of absorbers from iron. First two tracking stations will of GEM technology while the rest of stations can be made from straw-tube detectors. TRD stations can be used alternatively at the last MUCH station position. TOF can be used optionally with MUCH for the further reduction of unwanted background. Modified version of MUCH beam-pipe made of Aluminium has been presented with lead shielding beneath the first carbon absorber whose whole has also been optimised.

In chapter 5 the feasibility studies of MUCH has been given especially with respect to cocktail sources and charmonium. The layout of the muon detector system has been studied with simulations of central Au + Au collisions at $E_{lab}$ 25 AGeV with respect to acceptance, efficiency, and signal-to-background (S/B) ratio. Both for low mass vector mesons and $J/\psi$ mesons, the phase-space acceptances cover the midrapidity. For $\omega$ mesons emitted in central Au + Au collisions the S/B ratio is about 0.5 and the overall reconstruction efficiency is of the order of 1% at 25 AGeV beam energy. For $J/\psi$ mesons from central Au+Au collisions at 25 AGeV the overall reconstruction efficiency is 8.2% and the S/B ratio is close to unity. It should be mentioned that, even though in the present case, the performance of the system has been shown for the CBM experiment, the concept of this detector setup could be applied to any such experiment on high energy heavy ion collisions at similar energy range.

In chapter 6 two important probes have been discussed, namely fluctuation and strangeness production, of de-confined nuclear medium created in heavy ion collisions at FAIR energies. These collisions produce matter under very high net-baryon density. It is seen from the transport models that the net baryon density reaches maximum for a short time during the overlap of two nuclei. During this time, the particle multiplicity also reaches a peak and then slowly through the evolution reaches a near-saturated values at freeze-out. During this evolution, fluctuations at the beginning show structures which then smoothen out during the evolution. It therefore suggests that there is a considerable modification of the early fluctuation signals. We have studied the effect of hydrodynamical evolution of the signals by comparing the results from transport only, hydro with hadronic EOS and chiral EOS. It is seen that at freeze-out, $\nu_{dyn}$, the measures of fluctuations of K/$\pi$ for hydro with both hadronic and chiral EOS show higher values at lower beam energies as compared to the default version of UrQMD, with the chiral EOS being highest. However, the fluctuations with the chiral EOS shows more enhancement at lower beam energy. There is almost no effect seen on the charge ratio fluctuation in all the cases. This therefore suggests that even at freeze-out, at lower beam energy, fluctuations in K/$\pi$ might be considered to be important signals for identifying the EOS. For net-proton, fluctuation observables like S$\sigma$ and K$\sigma^2$ shows initial fluctuation, at the time of nuclear overlap, which washes out at freeze-out.

Moreover, chapter 6 also discusses the strange quark yield as well as multi strange hyperon yield via exchange mechanism which has been proposed to increase in a de-confined baryon rich medium created in heavy ion collisions. AMPT Model predicts the enhanced production of multi-strange hyperons in the partonic medium in comparison to the hadronic scenario and the partonic version of the model shows higher sensitivity to multi-strange hyperons. We have extrapolated the results towards the higher strange quark number particles and/or of higher mass. It should be noted that production of particles beyond three quarks require special treatment and as per this simplistic model the yields of strange objects with six (anti-)strange quarks could be of the order of $(10^{-4})10^{-6}$. To provide the experimental verification

of these predictions, detector system with high interaction rates are required-for which the Compressed Baryonic Matter (CBM) detector system is being designed at FAIR in Darmstadt, Germany.

# Bibliography


[1] C. Amsler et al., Phys. Rev. Lett. **B 667**, 1 (2008).

[2] http://pdg.lbl.gov/2008/listings/q009.pdf

[3] D. Decamp et al., Phys. Lett. **B 231**, 519 (1989).

[4] A. Fisher, *Searching for the Beginning of Time: Cosmic Connection*, Popular Science, 238 (1991)

[5] J. D. Barrow, *The Origin of the Universe,* Science Masters Series (1997).

[6] D .H. Perkins, *Particle Astrophysics*, Oxford University Press (2003).

[7] J. Schukraft and H.R Schmidt, J. Phys. **G 19**, 1705 (1993).

[8] M. Schmelling, *Proceeding of XXVII International Conference on High Energy Physics*, Warsaw (1996).

[9] Rohlf and J. William, *Modern Physics from $\alpha$ to $Z^o$* (1st ed.), Wiley (1994).

[10] Morii et al, *The physics of the standard model and beyond*, World Scientific (2004).

[11] F. Halzen and A. D. Martin, *Quarks and Leptons*, John Wiley & Sons (1984).

[12] H. Satz, Nucl. Phys. **A 418**, 447 (1984).

[13] C. Y. Wong, *Introduction to High-Energy Heavy-Ion Collisions*, World Scientific Publishing Company (1994).

[14] M. Anselmino, *Strangeness and spin in fundamental physics*, IOP Press US (2008)

[15] G. Baym, Nucl. Phys. **A 590**, 233 (1995).

[16] M. Alford, K. RajaGopal, and F. Wilczeck, Nucl. Phys. **B 537**, 443 (1998).

[17] T. Blum et al., Phys. Rev. **D 51**, 5153 (1995).

[18] J. Kapusta, P. Lichard, and D. Seibert, Phys. Rev. **D 44**, 2774 (1991).

[19] WA98 Collaboration, *Direct Photon Production in 158A GeV 208Pb+208Pb Collisions*, Phys. Rev. Lett. **85 (17)**, 3595 (2011).

[20] S. Drell and T.M.Yan, Phys. Rev. Lett. **25**, 316 (1970).

[21] E. V. Shuryak, Phys. Lett. **B 78**, 150 (1978).

[22] P. V. Ruuskanen, Nucl. Phys. **A 544**, 169 (1992).

[23] J. Kapusta, Nucl. Phys. **A 566**, 45 (1994).

[24] K. Kajantie, J. Kapusta, L. McLerran and A. Mekijan, Phys. Rev. **D 34**, 2746 (1986) .

[25] C. Gale and P. Lichard, Phys. Rev **D 49**, 3338 (1994).

[26] C. Song, C. M. Ko and C. Gale, Phys. Rev. **D 50**, 1827 (1994) .

[27] T. Matsui and H. Satz, Phys. Lett. **B 178**, 416 (1986).

[28] C. Baglin et al., Phys. Lett. **B 220**, 471 (1989).

[29] J. Rafelski and B. Muller, Phys. Rev.Lett. **48**, 1066 (1982).

[30] J. Rafelski, Nucl. Phys. **A 418**, 215 - 235 (1984).

[31] J. Rafelski and B. Muller, Phys. Rev.Lett. **56**, 2334 (1986).

[32] B. Muller and J. Rafelski, Phys. Rep. **142**, 167 (1986).

[33] J. Rafelski, Phys. Lett. **B 262**, 333 (1986).

[34] P. Koch, B. Muller, and J. Rafelski, Phys, Rep., **142(4)**, 167-262 (1986).

[35] M. Gyulassy , Nucl. Phys. **B 571**, 197 (2000).

[36] M. Gyulassy , Nucl. Phys. **A 661**, 637 (1999).

[37] C. Adler et al, Phys. Rev. Lett. **89**, 202301 (2002).

[38] http://cms.web.cern.ch/news/jet-quenching-observed-cms-heavy-ion-collisions

[39] K. Yagi, T. Hatsuda, and Y. Miake, *Quark-Gluon Plasma*, Cambridge University Press (2005).

[40] H. Heiselberg, Phys. Rep. **351**, 161 (2001).

[41] M. A. Stephanov, K. Rajagopal and E. Shuryak, Phys. Rev. Lett. **81**, 4816 (1998).

[42] M. M. Aggarwal et al. (WA98 Collaboration), Phys. Rev. **C 65**, 054912 (2002).

[43] S. Jeon and V. Koch, Phys. Rev. Lett. **85**, 2076 (2000).

[44] E. Shuryak and M.A. Stephanov, Phys. Rev. **C 63**, 064903 (2001).

[45] B. Mohanty, J. Alam, and T.K. Nayak, Phys. Rev. **C 67**, 024904 (2003).

[46] T. Satogata et al., *RHIC Low-Energy Challenges and Plans*, PoS(CPOD07)**051**, 837, 864 (2007).

[47] A. Laszlo (NA60 collaboration), *NA61/SHINE at the CERN SPS*, Pos(CPOD07)**054**, 837, 864 (2007).

[48] V. Toneev, *The NICA/MPD Project at JINR (Dubna)*, Pos(CPOD07)**057**, 837, 864, 921 (2007).

[49] FAIR Baseline Technical Report, http://www.gsi.de/fair/reports/btr.html 865, 868, 877 (2006).

[50] B. Friman, C. Hohne et al, *The CBM Physics Book*, Springer (2010).

[51] V. Friese et al., *The CBM Experiment at FAIR*, CBM Progress Report 2007 and 2008.

[52] D. Gonzålez-Diaz et al., *Progress in the CBM-TOF Wall: R&D and Simulation*, GSI Report 2007 and 2008.

[53] A. Akindinov et al., Nucl. Instrum. Meth. **A 572**, 676 (2007).

[54] A. Ivashkin, *Projectile Spectator Detector in CBM setup at SIS300, Talk given on the 1st CBM-Russia-JINR Collaboration Meeting in Dubna*(2009).

[55] http://cbm-wiki.gsi.de/cgi-bin/view/Public/PublicMuon

[56] A. Dubey et al., *R&D with GEMs and THGEMs Towards Developing a Muon Tracker for CBM*, CBM Progress Report 2007 and 2008.

[57] A. Delbert et. al., Nucl. Instrum. and Meth. **A 461**, 84 (2001).

[58] A. S. Brogna et al, NIM **A 568**, 301 (2006).

[59] CBM-Progress Report 2006 p. 49.

[60] C. J. Schmidt1 et al, CBM Progress Report 2007 p. 48.

[61] N. Abel1 et al, CBM Progress Report 2007 p. 53.

[62] R. L. Thews, M. Schroedter, J. Rafelski, Physical Review C 63, 054905 (2001)

[63] M. Gazdzicki and M. I. Gorenstein, Phys. Rev. Lett. 83 (1999) 4009

[64] S. Hamieh et al., Phys. Lett. B486, 61 (2000).

[65] R. Rapp, AIP Conf. Proc. 1322, 55 (2010).

[66] A. Kupsc, AIP Conf. Proc. 950, 165 (2007).

[67] K. Kajantie et al. , Phys. Rev. D34 (1986) 811; 2746

[68] G. Agakichiev et al. (CERES), Eur. Phys. J. C41 (2005) 475.

[69] R. Rapp and J. Wambach, Adv. Nucl. Phys. 25 (2000) 1

[70] R. Arnaldi et al. [NA60 Coll.], Phys. Rev. Lett. 96, (2006) 162302

[71] R. Arnaldi et al. [NA60 Coll.], Eur. Phys. J. C 61, (2009) 711

[72] R. Rapp, J. Wambach and H. van Hees, in Relativistic Heavy-Ion Physics (Springer), New Series I/23A (2010), arXiv:0901.3289 hep-ph

[73] R. Arnaldi et al., (NA60), PRL 100 (2008) 022302

[74] N. Xu, Int. J. Mod. Phys. E16 (2007) 715

[75] R. Arnaldi [NA60 Coll.], Nucl.Phys.A830 ( 2009) 345c

[76] A. Frawley, T. Ulrich, R. Vogt, Phys.Rept.462 (2008) 125

[77] T. Matsui, H. Satz, Physical Review Letters 79 (1997) 1229; G. Agakichiev, et al., Hades Coll., Physical Review C 84 (2011) 014902; R. Rapp, J. Wambach, H. van Hees, in: R. Stock (Ed.), Relativistic Heavy-Ion Physics, Landolt Boernstein (Springer), New Series I/23A (2010).;

[78] H. Akikawa, et al., Nuclear Instruments and Methods in Physics Research Section A 499 (2003) 537.

[79] K. Aamod, et al., ALICE collaboration, Journal of Instrumentation 3 (2008) S08002.

[80] S. Chatrchyan, CMS Collaboration, Journal of Instrumentation 3 (2008) S08004. 147

[81] P. Senger, Journal of Physics: Conference Series, 50 357; http://dx.doi.org/10.1088/1742-6596/50/1/048.

[82] S. Chattopadhyay, et al., Current Science 100 (2011) 682.

[83] CBM Collaboration, ¡http://repository.gsi.de/record/54798

[84] S. A. Bass, et al., Progress in Particle and Nuclear Physics 41 (1998) 225.

[85] I. Froehlichet, et al., Journal of Physics: Conference Series 219 (2010) 032039 arxiv:0905.2568v1.

[86] R. Brun, et al., GEANT3, CERN/DD/EE/84-1, 1986, long writeup W5013, 1993.

[87] F. Sauli, et al., Nuclear Instruments and Methods in Physics Research Section A 386 (1997) 531; A. K. Dubey, et al., Nuclear Instruments and Methods in Physics Research Section A (2012); A. K. Dubey, et al., Nuclear Instruments and Methods in Physics Research Section A 718 (2013) 418; A. K. Dubey, et al., Nuclear Instruments and Methods in Physics Research Section A 755 (2014) 62; A. K. Dubey, et al., Journal of Instrumentation 9 (2014) C06004.

[88] Y. Giomataris, et al., Nuclear Instruments and Methods in Physics Research Section A 419 (1998) 452.

[89] G. Battistoni, S. Muraro, P.R. Sala, F. Cerutti, A. Ferrari, S. Roesler, A. Fasso, J. Ranft, The FLUKA code: description and benchmarking, in: M. Albrow, R. Raja (Eds.), Proceedings of the Hadronic Shower Simulation Workshop 2006, Fermilab 6-8 September 2006, , AIP Conference Proceeding 896, 31-49, (2007), A.Ferrari, P.R. Sala, A. Fasso, J. Ranft, FLUKA: a multi-particle transport code CERN-2005-10 (2005), INFN/$TC_{05}$/11, SLAC-R-773.

[90] I. Kisel, Nuclear Instruments and Methods in Physics Research Section A 566 (2006) 85.

[91] R. Kalman, Journal of Basic Engineering Series D 82 (1960) 35.

[92] R. Fruhwirth, Nuclear Instruments and Methods in Physics Research Section A 262 (1987) 444.

[93] A. Lebedev, Journal of Physics Conference Series 219 032048, A. Lebedev Pos (ACAT08) 068.

[94] W. Cassing, E. L. Bratkovskaya, Physics Reports 308 (1999) 65; W. Ehehalt, W. Cassing, Nuclear Physics A 602 (1996) 449; J. Geiss, W. Cassing, C. Greiner, Nuclear Physics A 644 (1998) 107.

[95] I. Arsene et al. BRAHMS collaboration, Nucl. Phys. A 757, 1-27 (2005)

[96] A. Dainese for the ALICE Collaboration, Xiv:1212.0995 [nucl-ex]

[97] P. Romatschke and U. Romatschke, Phys. Rev. Lett. 99, 172301 (2007)

[98] V. Koch, *Hadronic Fluctuations and Correlations*, arXiv:0810.2520.

[99] H. Heiselberg, *Event-by-event physics in relativistic heavy ion collisions*, Phys. Rept. 351, 161-194 (2001)

[100] H. Heiselberg and A. D. Jackson, Phys. Rev. C63, 064904 (2001)

[101] C. Alt et al. (NA49 Collaboration), Phys. Rev. C 70 (2004) 064903.

[102] J. Adams et al. (STAR Collaboration), Phys. Rev. C68 (2003) 044905.

[103] K. Adcox et al. (PHENIX Collaboration), Phys. Rev. Lett. 89 (2002) 082301.

[104] C. Pruneau, S. Gavin, S. Voloshin, Phys. Rev. C66 (2002) 044904.

[105] J. T. Mitchell, J. Phys G30 (2004) S819.

[106] C. Alt et. al, for NA49 Collaborations, Phys. Rev. C77, 024903 (2008).

[107] M. M. Pawlowska, for the NA49 Collaboration, Central Eur.J.Phys. 10, 1285-1288 (2012)

[108] A. Schmah for the STAR Collaboration, arXiv:1202.2389v1 [Nucl-ex] (2012)

[109] M. A. Stephanov, Phys. Rev. Lett. 102, 032301 (2009).

[110] K. Rajagopal and M. A. Stephanov, private comm. 2009.

[111] STAR Collaboration ( M. M. Aggarwal et al. ), Phy. Rev. Lett. 105, 022302 (2010)

[112] P. Staig and E. Shuryak, Phys. Rev. C 84, 044912 (2011)

[113] B. Nilesson-Almqvist and E. Stenlund, Comput. Phys. Commun. 43, 387 (1987)

[114] B. Andersson et al., Nucl. Phys. B 281, 289 (1987)

[115] T. Sjostrand, Comput. Phys. Commun. 82, 74 (1994)

[116] S. A. Bass et al., Prog. Part. Nucl. Phys. 41, 255 (1198)

[117] M. Bleichner et al, J. Phys. G 25, 1859 (1999)

[118] J. Steinheimer et al., Phys. Rev. C 77, 034901 (2008)

[119] D. H. Rischke, S. Bernard and J. A. Maruhn, Nucl. Phys. A 595, 346 (1995)

[120] D. H. Rischke, Y. Pursun and J.A. Maruhun, Nucl. Phys. A 595, 383 (1995)

[121] H. Petersen, J. Steinheimer, G. Burau, M. Bleicher and H. Stocker, Phys. Rev. C 78, 044901 (2008)

[122] C. Pruneau, S. Gavin, and S. Voloshin, Phys. Rev. C 66, 044904 (2002).

[123] P. Christiansen, E. Haslum, and E. Stenlund, arXive:0902.4788v1 [hep-ex]

[124] S. Sarkar, H. Satz and B. Sinha (eds), *The Physics of the Quark Gluon Plasma, Springer Lecture Notes in Physics*, (2010), vol. 785.

[125] J. Rafelski and B. Müller, *Phys. Rev. Lett.* **48** (1982) 1066; P. Koch, B. Müller and J. Rafelski, *Phys. Rep.* **142** (1986) 167.

[126] P. Senger and V. Friese, *CBM Report 2012-01 Nuclear matter physics at SIS-100 The CBM Collaboration* (2012).

[127] C. Blume and C. Markert, *Prog. Part. Nucl. Phys.* **66** (2011) 834.

[128] S. Chattopadhyay, *Nucl. Phys.* **A931** (2012) 267c.

[129] Z. W. Lin, C.M. Ko, B.A. Li, B. Zhang and S. Pal, *Phys. Rev.* **C72** (2005) 064901.

[130] S. V. Afanasiev et al (NA49 Collaboration), *Phys. Rev.* **C66** (2002) 054902; C. Alt et al (NA49 Collaboration), *Phys. Rev.* **C78**, (2008) 034918 [nucl-ex/0804.3770]; F. Antinori, et al (NA57 Collaboration), *J. Phys. G* **32**, (2006) 427; F. Antinori et al (NA57 Collaboration), *Phys. Lett.* **B595** (2004) 68.

[131] A. Pevsner, et al., Phys. Rev. Lett. **7**, 421-423 (1961)

[132] G. R. Kalbfleisch et al, Phys. Rev. Lett. **12**, 527-530 (1964).

[133] M. Goldberg et al, Phys. Rev. Lett. **12**, 546-550 (1964).

[134] R. Rapp, E. Shuryak, Phys.Lett. **B473**, 13-19(2000)

[135] J. D. Bjorken and L. McLerran, Phys. Rev. **D31**, 63 (1985)

[136] C. M. Ko and C. Y. Wong, Phys. Rev. **C33**, 153 (1986)

[137] L. Xiong and C. M. Ko, Phys. Rev. **C37**, 880 (1988)

[138] Abbon P. et al., Nucl. Instr. Meth. A. **577**, 455-518 (2007)

[139] E. Abat ert al., JINST 3: P10003, 2008.